This electronic thesis or dissertation has been downloaded from the King's Research Portal at https://kclpure.kcl.ac.uk/portal/

Nanoparticle-assisted microwave sensing and hyperthermia for the detection and treatment of breast cancer

Wilson, Jasmin

Awarding institution:
King's College London

The copyright of this thesis rests with the author and no quotation from it or information derived from it may be published without proper acknowledgement.

END USER LICENCE AGREEMENT

Unless another licence is stated on the immediately following page this work is licensed under a Creative Commons Attribution-NonCommercial-NoDerivatives 4.0 International licence. https://creativecommons.org/licenses/by-nc-nd/4.0/

You are free to copy, distribute and transmit the work

Under the following conditions:

- Attribution: You must attribute the work in the manner specified by the author (but not in any way that suggests that they endorse you or your use of the work).
- Non Commercial: You may not use this work for commercial purposes.
- No Derivative Works - You may not alter, transform, or build upon this work.

Any of these conditions can be waived if you receive permission from the author. Your fair dealings and other rights are in no way affected by the above.

Take down policy

If you believe that this document breaches copyright please contact librarypure@kcl.ac.uk providing details, and we will remove access to the work immediately and investigate your claim.

Download date: 13. Jan. 2025

NANOPARTICLE-ASSISTED MICROWAVE SENSING AND HYPERTHERMIA FOR THE DETECTION AND TREATMENT OF BREAST CANCER

Annah Jasmin Wilson *BSc (Hons), MSc*

King's College London

Faculty of Life Sciences & Medicine
School of Cancer & Pharmaceutical Sciences

A thesis submitted in partial fulfilment for the degree of Doctor of Philosophy

2023

Acknowledgements

I would like to thank my colleagues and supervisors at King’s College London, the BBSRC LIDo Program, and the industrial sponsor for my project, MediWise.

I would like to dedicate this thesis to my family and friends. Without their love and support, none of this would have been possible.

Abstract

In recent years, microwave imaging/sensing and hyperthermia technologies have emerged in the field of diagnostics and therapy. Early-stage breast cancer diagnosis is one of the key application areas for the technology, where intervention at an early stage is essential for successful treatment and preventing progression to incurable secondary breast cancer. Breast cancer is the most common cancers in the UK, and advances in the imaging and treatment seek to address this unmet medical need. Current imaging modalities have limitations associated with cost and accessibility.

For diagnosis, this technology involves the application of low power microwaves, utilising contrast between the relative permittivity of tissues to identify pathologies. Antennas placed around the target region transmit and receive signals; the signal scatter is impacted by the dielectric properties of the individual tissue. The use of non-ionising radiation and low relative cost allows the technology to be available to a wider patient base, attempting to address the limitations of MRI and mammograms. However, challenges in the field associated with the heterogeneity of breast tissue and variance between individuals, can have an impact on the scale of the contrast in dielectric properties observed, making tumours more difficult to identify. The contrast in tissue permittivity can therefore be further enhanced through the implementation of nanomaterials. This project focuses initially on the development of nanomaterials suitable for use as contrast agents for microwave imaging/sensing. To achieve this, polymer-coated zinc ferrite nanoparticles were synthesised and assessed for their dielectric properties in model systems including *ex vivo* and *in vivo*. In particular, *in vivo* experiments demonstrated injected polymer-coated zinc ferrite nanoparticles increased the observed dielectric constant in triple-negative breast cancer tumours in a mouse model system.

For therapy, microwave technologies can be applied in tissues either through hyperthermia, which can help anti-cancer drug tumour penetration, or as ablation to destroy malignant tissues. Advances in this area have centred on the development of hyperthermia and ablation antennas, designed to selectively heat targeted tissues. However, concerns remain regarding the heating of deep-seated tumours and unintentional heating of peripheral tissues, causing damage. Nanomaterials can absorb electromagnetic radiation and can enhance the microwave hyperthermic effect. This could allow heating to be applied at lower powers, limiting damage to surrounding tissues. This technology has the potential to be combined with thermosensitive drug release, allowing therapeutic targeting to tumours. This project explored the development of a lab microwave hyperthermia (MWHT) setup suitable for use *in vivo*. This was achieved using suitable breast tumour mimicking phantoms before progression to *in vivo* experiments. Microwave responsive PSMA-coated zinc ferrite nanoparticles developed for microwave imaging/sensing were also tested in conjunction with the MWHT antenna, to assess the impact on observed heating profiles. Finally, image-guided thermosensitive liposomes (iTSLs) were tested in conjunction with microwave hyperthermia *in vivo*, to establish if MWHT is suitable for the targeted release of therapeutics.

Table of Contents

List of Figures

Abbreviations

CNT	Carbon nanotubes
CT	Computerised tomography
EM	Electromagnetic
ER	Estrogen receptor
HIFU	High intensity focused ultrasound
HER2	Human epidermal growth factor 2
iTSLs	Image-guided thermosensitive liposomes
MMG	Mammogram
MNPs	Magnetic nanoparticles
MRI	Magnetic resonance imaging
MW	Microwave
MWI	Microwave imaging
MWHT	Microwave hyperthermia
MWNT	Multi-walled carbon nanotubes
NPs	Nanoparticles
PEG	Polyethylene glycol
PET	Positron emission tomography
PMAO	Poly(maleic anhydride-alt-1-octadecene)
PR	Progesterone receptor
PSMA	Poly(styrene-co-maleic anhydride)
TNBC	Triple-negative breast cancer
TSLs	Thermosensitive liposomes
US	Ultrasound

Publications

A. J. Wilson, M. Rahman, P. Kosmas and M. Thanou, “Nanomaterials responding to microwaves: an emerging field for imaging and therapy.” Nanoscale Adv. 2021 Apr 1;3(12):3417-3429. doi: 10.1039/d0na00840k. PMID: 34527861; PMCID: PMC8388194.

A. J. Wilson, P. Kosmas and M. Thanou, "Ex-vivo Dielectric Properties of Tissues in Athymic Nude Mice," 2022 3rd URSI Atlantic and Asia Pacific Radio Science Meeting (AT-AP-RASC), 2022, pp. 1-4, doi: 10.23919/AT-AP-RASC54737.2022.9814269.

1: Introduction

It should be noted that a large portion of this introduction is adapted from our publication:

Wilson AJ, Rahman M, Kosmas P, Thanou M. Nanomaterials responding to microwaves: an emerging field for imaging and therapy. Nanoscale Adv. 2021 Apr 1;3(12):3417-3429. doi: 10.1039/d0na00840k. PMID: 34527861; PMCID: PMC8388194.

1.1 Overview

Nanomaterials that respond to electromagnetic (EM) radiation have been suggested for either imaging and/or hyperthermia. These nanomaterials would need to be suitably biocompatible as well as able to interact with EM energy to induce a signal response or increase the temperature locally. To this end, various nanomaterials have been suggested as contrast agents in microwave (MW) imaging and sensing, with the aim to increase contrast between target and background tissue Figure 1.

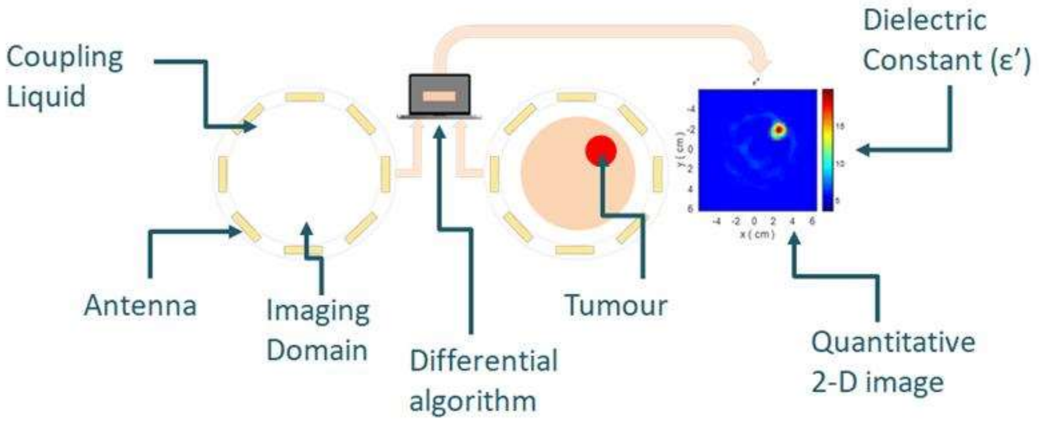

Figure 1 - Typical microwave imaging scheme for biomedical applications. Antennas are placed around the exterior of the imaging domain which contains the object of interest,with downsteam algorithm processing allowing the identification of the target.

This principle is based on the hypothesis that nanoparticles (NPs) are accumulated in tumours. If NPs with high dielectric constant could accumulate in tumours, they could alter the permittivity of the tumour, providing a required tissue dielectric contrast. In recent years, however, the potential of preferential NP accumulation has been debated amongst experts. For example, a review of 232 data sets conducted by Chen *et al.* in 2016 suggested a median of 0.7% of the systemically injected dose reaches the tumours[1] , while the same group showed in 2020 that the injected NP dose is critical. In particular, an intravenous administration in mice of over 1 trillion NPs resulted in an increased accumulation in tumours of up to 12% of the injected dose.[2]

Targeting NPs to cancer has long been considered a challenge.[3] While an extensive review of the topic is beyond the scope of this review, it is important to consider the main factors that are important to improve NP concentration in tumours. This is of particular significance owing to the likelihood that both imaging/sensing and hyperthermia will be dependent on the concentration of the MW responsive NPs in tumours. Adaptation of NP size to compliment tumour pathophysiology has been demonstrated to improve permeation. [4]

Another classic method to improve the concentration of the nanoparticles in tumours is by modifying the nanoparticle surface to represent ligands that facilitate binding on receptors related to the lesion. A number of molecules have been shown to improve nanoparticle binding in tumours such as antibodies, peptides, sugars aptamers and small molecules. [5]

Finally, physical non-invasive methods such as localised sound and heat can increase the tumours blood vessels permeability and enhance extravasation in tumours. Developing nanomaterials for MW applications should consider both the chemical and physical methods of increasing the nanoparticle concentration in tumours. [6]

The concept of increasing the relative permittivity of tissue using nanomaterials for sensing and imaging has been introduced recently with current studies mainly using phantoms[7–10], and only few published studies seen to present *in vivo* data. In hyperthermia, however, combining NPs with MW applicators has been tested *in vivo,* producing strong evidence that there is synergy. This review will present the principles of MW imaging/sensing and hyperthermia and the nanomaterials that have been explored up to now. The outlook of combining nanomaterials and MW modalities will be discussed.

1.2 Breast cancer

The focus of this research is MW imaging/sensing and hyperthermia in conjunction with nanoparticles, specifically for the detection and treatment of breast cancer. It is important therefore, to outline the relevant area of unmet medical need we are seeking to target.

Breast cancer is one of the most prevalent cancers in the UK and worldwide, with millions of people diagnosed each year. Breast cancer is most common in women, but can also rarely affect men, with male breast cancer accounting for approximately 1% of diagnosed cases in the UK.[11] Incidence rates of female breast cancer are rising globally, showing an increase of approximately 0.5% every year. [12] In 2020 alone, 2.3 million new cases of breast cancer were diagnosed across the world, with nearly 700,000 deaths from the disease reported that same year.[13] With rates rising and the global burden increasing, it's evident that continued research will be required to support this medical need.

Breast cancer is classified using the TNM (tumour; nodes; metastasis) staging criteria.[14] These criteria give an indication of the size of the primary tumour, migration to lymph nodes and any detectable metastasis to other tissues. Breast cancer can also be characterised by the presence of receptors; the estrogen receptor (ER), progesterone receptor (PR) and overexpression of human epidermal growth factor 2 receptor (HER2) protein.[15] Identification of receptor expression is central to some treatment strategies, with hormonal therapies such as Tamoxifen forming a part of treatment regimes.[16] Triple negative breast cancer (TNBC) is an aggressive breast cancer subtype, that lacks presentation of these hormone receptors. TNBC has been associated with poor treatment outcomes, with increased rates of recurrence and death seen in women diagnosed with this subtype.[15,17]

Early diagnosis is key to successful treatment outcomes[18], and therefore interventions have focused on this, with screening using x-ray mammography showing statistically significant reductions in breast cancer mortality in participating groups.[19] X-ray mammography is one of the most common imaging technologies associated with breast cancer. The current UK mammogram screening program invites women between the ages of 50 and 70 for a screening every 3 years. This age range reflects the most at-risk age group for breast cancer, with studies demonstrating increased risk onset with age.[20] Limitations with mammography are largely associated with breast density, with research showing reduced sensitivity in the screening of dense breast tissue.[21] Mammograms also have high incidence rates of false positives, causing stress and anxiety to affected patients. [22,23]

Ultrasound is another modality sometimes used in the breast cancer diagnostic pathway, often as an adjunct to mammography, offering a comparatively low cost to other available modalities and a portable transducer system. Clinical ultrasound uses high frequency sound waves between 1 and 20 MHz to create a real-time image. A global review of diagnostic studies using ultrasound in breast cancer found overall sensitivity of 80.1% and specificity of 88.4%, showing the benefit of this modality particularly in circumstances where mammography or MRI may not be available.[24] However, there are limitation of breast ultrasound including low resolution and time-consuming scans.

The most sensitive imaging modality for breast cancer is magnetic resonance imaging (MRI) with a higher sensitivity than mammography.[25] MRI is often applied in conjunction with gadolinium-based contrast agents. While sensitive, MRI comes at a significant cost and often limited availability and is therefore often reserved for the most at-risk cases.[26]

Given the significant role of imaging modalities in early diagnostics, effective and accessible imaging approaches are required. MW imaging/sensing shows potential as a portable and cost-effective modality which does not use ionising radiation. Recent research has demonstrated breast cancer to be a candidate for application of this technology.[7,27–29]

1.3 Microwave imaging/ sensing and its principles

MW imaging or sensing can be described as the use of non-ionizing EM radiation for the profiling of tissues. Principally, antennas are used to transmit EM signals within the MW frequency (300MHz-300GHz), and the subsequent scattering and refection is processed through algorithms and is used to create a dielectric tissue profile.[28]

The dielectric constant of a material can be described as the ratio of the relative permittivity of a material to that of a vacuum. However, this can be described in more depth as a function of frequency as below:

$$\varepsilon_r^*(\omega) = \varepsilon'_r(\omega) - j\varepsilon''_r(\omega) = \varepsilon'_r(\omega) - j\frac{\sigma}{\omega\varepsilon_0} \qquad (1)$$

In (1), the real part $\varepsilon'_r(\omega)$ represents how much electric energy is stored by the material, and the imaginary part $\varepsilon''_r(\omega)$ represents the energy loss (in form of heat) due to the material properties. Another relevant quantity is the loss tangent ($tan\delta$), which is also known as the loss angle, and is defined as:

$$tan\delta = \frac{\varepsilon''}{\varepsilon'} = \frac{1}{\varrho} \qquad (2)$$

MW imaging broadly includes two approaches, termed tomography and radar. MW tomography is a quantitative imaging technique that estimates the relative permittivity of an object through cross-sectional imaging by producing a dielectric map of the target tissue.[30] Radar-based MW imaging is a qualitative technique and focuses signals on set points to identify regions with unusual scatter.[31] Applications of MW technologies are far reaching, with research in agricultural[32,33], military [34,35] and clinical areas. This review will present the potential clinical pathways for MW imaging, which have taken both tomography and radar-based approaches and explore how nanomaterials can be used as contrast enhancers.

1.4 Applications of microwave imaging and sensing

Microwave imaging and sensing is a complex process that is dependent on the relative permittivity of the tissue to be measured, its depth in the body and the MW frequencies used to detect the difference between lesion and healthy tissue. MW imaging faces the challenge of requirement of a high dynamic range system to successfully measure weak scattering fields.[36] Initial studies on assessing tissues in 50 to 900 MHz frequency range indicated differences in electrical properties from normal to malignant for kidney about 6% and 4% and for mammary gland about 233% and 577% average differences in permittivity and conductivity, respectively. [37] Other types of tumours such as colon and liver showed small differences in both parameters indicating that contrast enhancers would benefit the MW detection of these tumours.

Challenges still remain open at experimental level where there is a need to efficiently connect the microwave parameters to the target biological tissues as well as identifying the suitable frequency for good resolution and penetration depth, and development of suitable contrast agents.

In MW tomography the frequency that is applicable for imaging larger objects, for example bone in whole-body imaging is 0.9 GHz whereas higher frequencies (up to 3–4 GHz) are applicable in terms of tissue penetration producing high resolution images. [38]

Breast cancer is one of the key areas in which MW technology is seeking to provide clinical impact through the offering of a low-cost non-ionising imaging modality.[39] Early work in the area identified the contrast observed in relative permittivity of healthy and cancerous tissues of the breast [40], providing a promising foundation for progression. Early measurements at 3.2 GHz indicated that the most common relative permittivity values for breast fat were 4 to 4.5 for normal breast glandular tissue 10 to 25, compared with 45 to 60 for breast malignant tissues.[41] Since then, several studies have further confirmed differences between healthy and malignant tissue. [42]

This has been strengthened by more recent clinical advances such as the MARIA® system (Micrima Ltd)[27], which utilises radar approach to create a 3-D image of the breast lesion. The system demonstrated a detection rate of 74% across the full sample group, rising to 86% in dense breast tissue patients. For this type of breast imaging the frequencies between 3-8GHz are used. While there has been notable progress in this area, there are still challenges to overcome such as sensitivity and image resolution.[43]

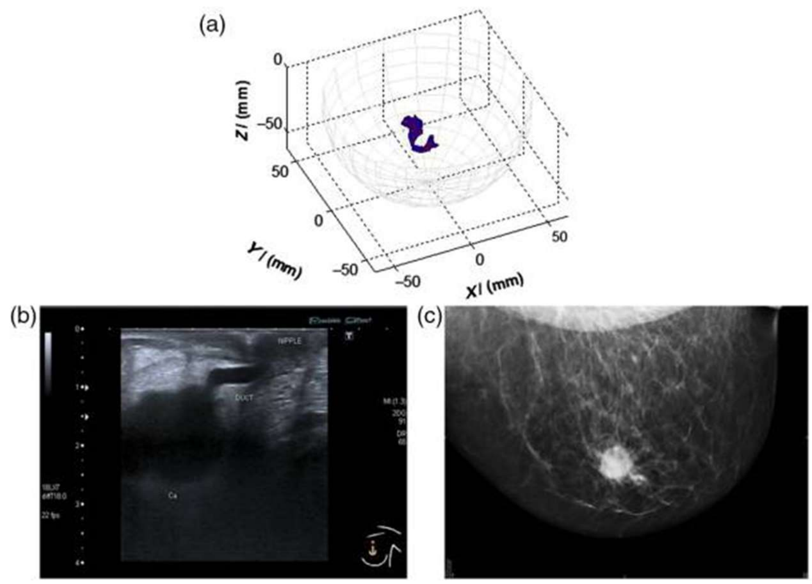

Figure 2 - An example of a MARIA scan compared with a mammogram (MMG) and US. (a) MARIA M4 scan [max focused strength at (X=3, Y=21, Z=−42mm)], (b) US scan, and (c) MMG. Clinical diagnoses: carcinoma 17 mm and liquid-filled milk duct. Reproduced with permission from ref. [27]

Reprinted (adapted) with permission from ref [27]. (Alan W. Preece, Ian Craddock, Mike Shere, Lyn Jones, and Helen L. Winton "MARIA M4: clinical evaluation of a prototype ultrawideband radar scanner for breast cancer detection," Journal of Medical Imaging 3(3), 033502 (20 July 2016). https://doi.org/10.1117/1.JMI.3.3.033502). Used in accordance with the Creative Commons Attribution license.

Feasibility studies have also assessed and found promise in the ability of MW imaging to be used on the brain[44], with possible applications in areas such as stroke imaging and monitoring[45,46] as well as brain injuries. The frequency range for MW brain imaging has been reported as 0.75–2.55 GHz30 and 0.5–4.0 GHz.31 As with MW breast imaging, characterisation could take either a tomographic or radar approach and aims to again provide cheap and potentially portable sensing that can ensure very quick turn-around time, which is a critical requirement in diagnostics of acute stroke or brain injury. Clinical evaluation has been undertaken in this area, with examples including the MW helmet and accompanying diagnostic algorithm evaluated by researchers at Chalmers University in the detection of intercranial hematomas, which showed 75% specificity at 100% sensitivity.[49] Critically, MW technology has also demonstrated the ability to differentiate between haemorrhagic and ischemic stroke, which is essential to patient treatment and outcomes.[50] Ongoing research in this area includes prototype brain imaging scanners which are under investigation by a number of companies that develop MW imaging systems.

MW imaging has also begun to generate interest on a cellular level, with emerging studies describing the contrast between the dielectric signatures of healthy and cancerous cell lines.[51,52] Ahmad *et al.* noted that "normal cells were observed to exhibit higher dielectric constants when compared to cancer cells from the same tissue". In addition to this, cancer cells of different origins could be identified by their electronic properties. It has also been suggested that MW technologies may have the potential to characterise the morphological properties of cells.[53]

1.5 Nanoparticles and nanomaterials as potential contrast agents for microwave imaging/sensing

In recent years, NPs have demonstrated their potential to be applied extensively across biomedicine and bioimaging. In the case of MW imaging and sensing the investigation of microwave-sensitive materials looks to alter the dielectric properties of a targeted area, thereby providing an enhancement on the established contrast between background and the desired area of focus. This would enhance detection through an improved reconstruction image.

A need for such contrast agents has been identified in MW imaging areas such as breast cancer. As discussed, early studies have shown the contrast observed in dielectric profile between healthy and cancerous tissues of the breast. In 1988, Surowiec *et al.* profiled excised breast tumour samples from different areas with large water content variation.[40] The results demonstrated differences in dielectric constant related to the sample origin and morphology measured at frequencies from 20kHz to 100MHz. While this is a promising foundation for MW imaging, due to the heterogenous nature of breast tissue, in some areas of the breast, such as fibroconnective and glandular tissues, this contrast can be as low as 10 [54] %, highlighting the potential for contrast agents to grow in this area. This large-scale study by the University of Wisconsin and the University of Calgary 37,38 showed that: (i) "there is a large variation in the dielectric properties of normal breast tissue due to substantial tissue heterogeneity"[54] and (ii) the contrast in dielectric properties "between malignant and normal adipose-dominant tissues in the breast is considerable, as large as 10 : 1", while the contrast "between malignant and normal glandular/fibroconnective tissues in the breast is no more than approximately 10 per cent".[54] This highlighted the need for both improving contrast and developing of sophisticated microwave imaging approaches. With this in mind, MW imaging/sensing systems have begun to explore the inclusion of contrast enhancement, such as through iron oxides.[56]

A range of materials have been investigated for their dielectric capabilities.[57] Iron oxides are well established in biomedicine through their use as MRI contrast agents and identification as vehicles for drug delivery.[58] Studies have gone on to evaluate their potential use in the altering of dielectric properties, with outcomes indicating low but detectable contrast which was hypothesised to be due to polarity either from the carboxydextran coating of the iron oxides or else the surfactant used in the preparation.[59] Enhanced MW absorption properties have been observed in ferrite nanocomposites, such as those formed with carbon black.[60] In our group, investigations focus on ferrite NPs, with zinc ferrite particles tested in phantoms demonstrating the ability to further improve the dielectric contrast between healthy and target tissues when compared with commercial iron oxides.[61] In this study, ferrites of differing zinc concentration were synthesised and compared with iron oxides, with all particles functionalised with the polymer PMAO (Poly(maleic anhydride-alt-1-octadecene)). This links with further work by our group conducted with ZnO particles which had been functionalized with PEG (Polyethylene glycol) were demonstrated to produce a difference in dielectric constant in a frequency range of 1 and 4 GHz when suspended in water.[62]

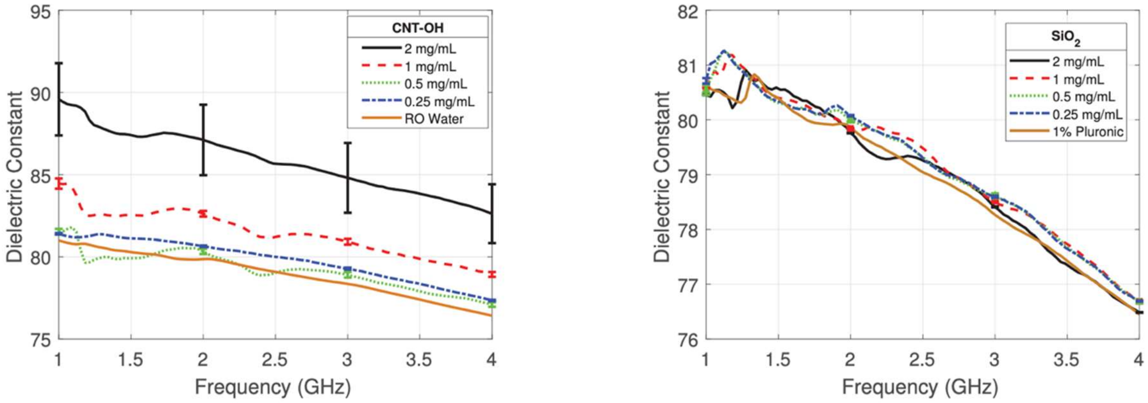

(a) CNT-OH (RO Water) (b) SiO_2 (1% Pluronic)

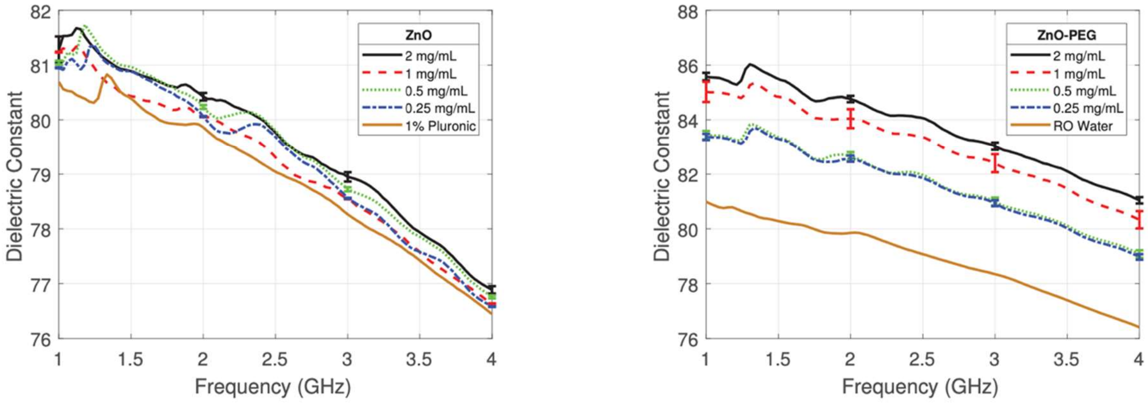

(c) ZnO (1% Pluronic) (d) ZnO-PEG (RO Water)

Figure 3 - Average dielectric constant of colloidal dispersions of (a) CNT-OH in RO water, (b) SiO2 with 1 % Pluronic, (c) ZnO with 1 % Pluronic, and (d) ZnO-PEG in RO water characterised between 1–4 GHz. Reproduced with permission from ref. [62]

Research in these microwave-sensitive materials has provided the foundation for contrast agent exploration, with studies moving into model systems and in some cases *in vivo* work. This has also been explored in stroke detection, where the administration of superparamagnetic iron oxide NPs was used to enhance image reconstruction through increased signal attenuation.[63] In this pioneering study, ferumoxytol was investigated for the potential to enhance contrast in MW imaging in phantoms in ischaemic stroke rabbit model and in humans. The study indicated that at frequencies 1-2 GHz it was possible to observe contrast in phantoms and rabbits using a purpose made MW imaging device, with increased attenuation of the MW signal in phantoms containing the iron oxides. Intravenous administration of the iron oxides into rabbits also produced increased MW signal attenuation above 1.3GHz. In a healthy male human ferumoxytol provided some signal difference however the data were not clear and indicated that the signal difference was not consistent over time probably due to ferumoxytol blood kinetics. The authors concluded that considering all studies, their data suggested that superparamagnetic iron oxide NPs attenuate the transmitted MW signal and operate as MW contrast enhancers. Further benefits of this approach include the ability to functionalize the NPs, allowing tissue specificity through the addition of peptides or antibodies. In 2020, Qin *et al.* explored Fe_3O_4 nanoparticles modified with galectin-1 antibody in the targeted microwave-induced thermoacoustic imaging of pancreatic cancer, demonstrating an enhanced contrast ratio.[64]

Carbon nanotubes (CNT) are another nanomaterial that has attracted the interest of MW researchers. An early analysis of the nanomaterial in 2009 indicated that "When carbon nanotubes are exposed to microwaves, strong absorptions are observed, producing intense heating, outgassing, and light emission".[65] Carbon nanotubes have unique electronic properties, which can be attributed to their distinctive structure. [66] They have been assessed as potential MW contrast agents and have been modified in several ways to increase these properties.[67] Composites with carbon nanotubes have also been characterised such as with the polymer polypropylene for both dielectric properties and MW heating. [68] Although carbon nanotubes are consistent in enhancing the dielectric constant of media and phantoms, their mechanism of interacting with MW radiation at these frequencies is unclear. They do however have a notable ability to produce signal attenuation as well as consistently increasing the temperature of phantom models and have therefore been suggested as agents of theranostic potential.[69]

Dielectric influencers can also be identified through their use in electronics, such as silicon dioxide (SiO_2) nanoparticles. Often used in hybrid materials, they have several different electronic applications, such as fillers in capacitors. It comes as no surprise therefore, that SiO_2 composites formed with a diverse range of materials including polymers and carbonyl iron, have been reported to produce an enhanced MW absorption.[70–74] More recently, it has been indicated that SiO_2 nanoparticles can be doped to introduce dipoles, thereby increasing their MW absorption properties.[75]

Following a similar trend, barium titanate ($BaTiO_3$) nanoparticles are also common dielectric agents in multi-layered ceramic capacitors, due to their ability to alter the dielectric properties of the matrix fillers. The ability of $BaTiO_3$ to increase the dielectric constant has been characterised in solution[76] , where concentrations of $BaTiO_3$ between 0-12% with an average size of 70nm have shown to increase the dielectric properties of 1-propanol when in suspension at a frequency of 20.0MHz. The dielectric constant of barium titanates has been shown to alter with temperature[77]; at 10.0MHz large temperature increases between 700-1050°C significantly increased the dielectric constant. It has also been reported that these properties can be altered, such as through the polymer modification, with interesting findings including the formation of a $BaTiO_3$ composite with polyaniline powder caused a significant reduction in the dielectric constant.[78] With formation of nanocomposites an established way to change MW properties, combination with high dielectric permittivity polymers has been explored with examples including polyvinylidene fluoride (PVDF).[79] This study demonstrated an ability to increase the dielectric constant of these $BaTiO_3$ nanowire composites through the tuning of the aspect ratio, which was achieved though the alteration of the hydrothermal reaction temperature. A further study in the area indicated $BaTiO_{3-}$ PVDF composites could produce a higher dielectric constant when the $BaTiO_3$ nanoparticles were modified with PEG, the basis for which was proposed to be due to enhanced polarisation.[80]

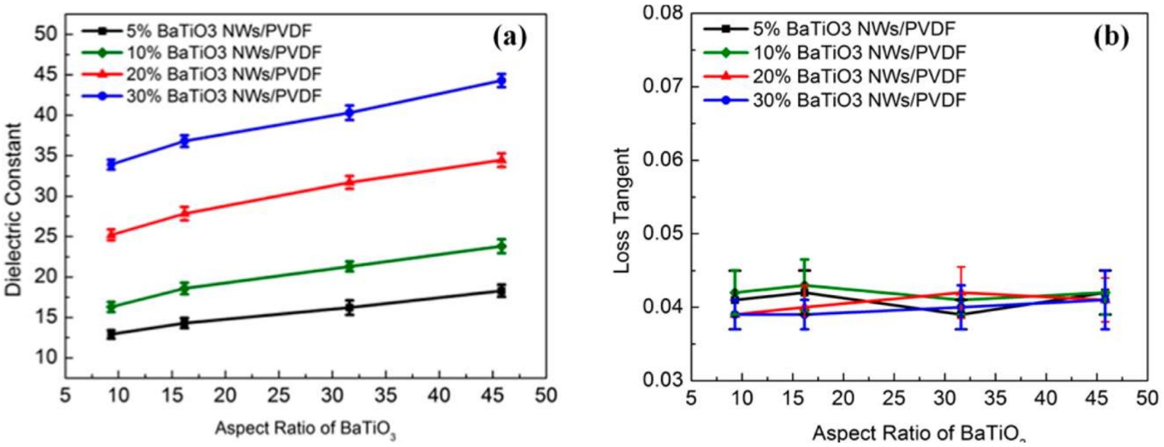

Figure 4 - (a) Dielectric constant and (b) loss tangent of the nanocomposites measured at 1 kHz as a function of aspect ratio and volume fraction of BaTiO3 NWs. Reproduced with permission from ref. [80]

Reprinted (adapted) with permission from ref. 60 (H. Tang, Z. Zhou, H.A. Sodano. Relationship between $BaTiO_3$ nanowire aspect ratio and the dielectric permittivity of nanocomposites. ACS Appl Mater Interfaces. 2014 Apr 23;6(8):5450-5. doi: 10.1021/am405038r. Epub 2014 Apr 14. PMID: 24670582.). Copyright (2014) American Chemical Society.

Hydrogenation of $BaTiO_3$ nanoparticles has also been studied as a mechanism to increase their MW absorption[81], with characterisation conducted in a paraffin wax dispersant over a 1–18 GHz frequency range. Overall, the hydrogenated particles showed increased MW absorption when compared with their pristine counterparts which the authors postulate is due to increased interfacial polarisation.

Titanium oxide (TiO_2) nanoparticle studies have shown its high dielectric capabilities with studies involving polymer matrices and ceramic systems.[82–84] As with other MW absorbing materials, it has been demonstrated that synthesis parameters such temperature have an influence on downstream dielectric properties. [85] Further modification of the synthesis such as partial crystallization and hydrogenation can also have a positive impact on these properties.[86,87] Titanium oxide has also shown early promise in cancer therapy as a method to induce necrosis of cancer cells when illuminated with a specific electromagnetic radiation as well as additional radiation therapy.[88]

Studies have also been conducted using microbubbles, with the overall indication that the presence of the microbubbles decreased the dielectric properties thereby providing contrast.[89] Although interesting, there were some limitations of this, as the dielectric behaviour was heavily influenced by the dispersion of the microbubbles.

Solution	**Initial microbubble concentration (% by weight) at 0 mins**	**Estimated actual concentration (% by weight) at 2.5 mins**	**Average ε r (3GHz)**	**Average σ (3GHz) (S/m)**
1	0	0	14.03	2.32
2	5	20	9.66	1.33
3	10	30	8.34	1.11
4	20	35	7.38	0.95
5	30	40	6.86	0.84
6	100	100	NA[a]	NA[a]

Figure 5 - Summary of data for microbubbles assessed at 3GHz. Adapted with permission from ref. [89]

Figure 6 shown below shows a selection of nanomaterials identified for MW imaging and that have not been identified as contrast agents in other imaging modalities. These nanomaterials represent a variable chemical composition with a minimum change of surface characteristics. The surface of nanomaterials should be altered to allow biocompatibility and tumour receptor potential.

Nanomaterial type	**Composition**	**Size**	**Shape**	**Surface**	**References**
Ferrites	Nanocomposite with nickel and zinc ($Ni_{0.6}Zn_{0.4}Fe_2O_4$)	Average of 53nm	Not specified	Not specified	[60]
	ZnO-PEG	60-100nm	Spherical	PEG	[62]
Carbon Nanotubes	Single-walled carbon nanotubes	Diameter 1-2nm	Rod	Not modified	[69]
Barium Titanates	Pristine and hydrogenated $BaTiO_3$	Diameter 20-30 nm (pristine) and 100-200nm (hydrogenated)	Not specified	Not modified	[81]

Figure 6 - Examples of nanomaterials tested for MW imaging and sensing that represent a variable chemical composition.

1.6 Microwave hyperthermia (MHWT) as a cancer treatment method

In this context, hyperthermia refers to the heating of a targeted area using with an end goal in the improvement of therapy, which can be induced through a range of methodologies including microwave. The use of hyperthermia in cancer treatment is an established clinical technique, where the application of heat to around 42°C has been demonstrated to increase tumour cell death and improve the efficacy of treatment options such as chemotherapy and radiotherapy by increasing cytotoxic effects on the desired cells.[90,91] The treatment may be applied locally, regionally or through the whole body, with aims in producing as little damage as possible to any surrounding healthy tissues. Heat is applied to induce either reversible tissue changes including increase of cell metabolism, blood perfusion and oxygen supply via hyperthermia (40–45°C), or to irreversibly change tissue during ablation (50–110°C). The tissue change (damage) depends on both duration and temperature, and can change blood perfusion, or cause changes in the mechanical, electrical and thermal tissue properties.[92] Hyperthermia has also been considered as a means to enhance immunotherapy approaches to cancer treatment.[93]

As with many cancer therapeutics, specificity remains a hurdle for hyperthermia and while minimally invasive, there may be the undesired effect of heating on surrounding tissues. As applications of microwaves have been established as a means of inducing hyperthermia, one possible solution to this is through the utilisation of microwave-sensitive materials to allowed targeted enhancement of the heating effect. NPs have been demonstrated to prefer highly vascularised tumours and they could offer such specificity when combined with non-invasive MW hyperthermia techniques.

Microwave hyperthermia is usually applied for superficial or intraluminal/intracavitary tumours using antennas at 433 MHz, 915 MHz and 2450 MHz. microwave ablation is induced using a needle applicator at frequencies 915 MHz or 2.45 GHz. Microwave ablation causes dielectric heating in a volume around the applicator.[94] Higher frequency MW heat systems use antennas with small dimensions, showing flexibility in probe design and can make the procedure non-invasive. Several studies on ablation have been conducted at higher frequencies, ranging from 9.2 to 24.1 GHz.[95]

Although the systems of non-invasive ablation are in development, endoscopic MW devices prove to be valuable tools in inducing localised ablation when used under imaging. These endoscopic devices would largely benefit from the use of nanomaterials that could enhance the local MW absorption.[96] Devices for endoscopic ablation are in development (Endowave.ie) and could find biomedical applications of treating oesophagus lung and bowel lesions. The use of MW absorbing nanoparticles with such endoscopic devices could offer a specific and controlled ablation method.

Thermometry is required in all thermal treatments. Non-invasive thermometry should be used during the treatment to provide temperature feedback in order to safely control treatment and avoid exceeding the temperature limits. From all imaging techniques used such as X-ray computed tomography, microwave tomography, echo sonography, and magnetic resonance (MR) imaging, the proton resonance frequency method of MRI is the only method currently in clinical practice due to its temperature sensitivity that appears consistent in most aqueous tissues and because it can be easily observed using common clinical MRI scanners.[97] The proton resonance frequency shift (PRFS) is used in MRI guided interventions. The proton resonance frequency (PRF) of hydrogen in water molecules, the most abundant molecules in the human body, depends linearly on temperature. RPFS can be affected by the body motion, however this can be corrected. There is however indication that some paramagnetic agents can affect the RPFS and the temperature measurements. Gadolinium based contrast agents (linear) have been found to affect the focal heating point read out by 2°C. Such effect can be corrected by the dose and or the type of contrast agents.[98] If, however paramagnetic contrast agents affect the temperature feedback, emphasis should be given that the nanomaterials used to increase the temperature locally after MW application do not have a large effect on RPF.

1.7 Nanoparticle enhanced microwave hyperthermia (MWHT)

MW sensitive nanomaterials have the potential to be applied in the growing area of hyperthermia with magnetic NPs already identified as capable of hyperthermia enhancement.[99] In this approach, the focus shifts from detection and diagnostics to harnessing the capabilities for therapeutics, both as a stand-alone technique and in combination with drug administration. The theory behind this approach involves the selective uptake of MW sensitive NPs by a target area such as a tumour. Due to the presence of these NPs, the application of MW radiation will provide enhanced hyperthermia in the target region. This has the potential to be combined with drug-loaded NPs to deliver a dual-approach therapeutic, in keeping with the current trend towards research in theranostics.[100]

As in MW sensing, breast cancer forms a key area of interest within MWHT, with studies conducted *in vitro, ex vivo* and using breast imaging model systems.[101] This novel study utilised transmission ultrasound combined with NPs to monitor subsequent application of MW hyperthermia. The results demonstrated the favourable impact of 10nm Fe_3O_4 iron oxide nanoparticles on the induction of heat alongside improvement of target detection and non-invasive thermo-monitoring. Copper oxide particles were also evaluated for the same purpose but were not observed to improve the heating rate. Studies are not limited to breast cancer, with maghemite γ-Fe_2O_3 evaluated for hyperthermia potential in liver cancer. Here it was noted that the presence of the magnetic NPs allowed a lower power input of MW radiation to achieve the desired level of hyperthermia.[102] Iron oxide composite NPs have also been identified as candidates for microwave-controlled drug release,[103] further demonstrating the potential in both contrast and therapeutics.

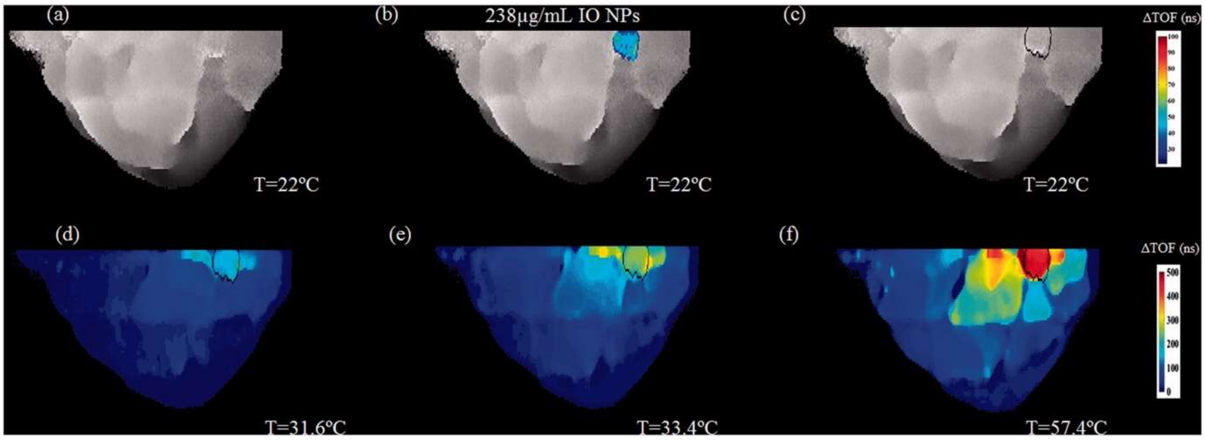

Figure 7 – An example of two-step image guided therapeutic procedure in a heterogeneous breast phantom, using Iron Oxide-based NETUS (nanoparticle-enhanced transmission ultrasound). Reproduced with permission from ref. [101] with permission from the publisher-Taylor & Francis Ltd, http://www.tandfonline.com.

In 2017, McWilliams *et al.*[104] also explored iron oxide NPs in relation to MWHT, testing a range of compositions and spherical, cubic and hexagonal shapes. Experiments were conducted at frequencies of 2.0, 2.45 and 2.6 GHz in tissue-mimicking phantoms. Overall, the authors concluded that the spherical Fe/Fe$_3$O$_4$ nanoparticles showed the greatest potential for thermal enhancement. The Prakash group has also conducted *in vivo* research demonstrating MW hyperthermia systems combined with magnetic resonance thermometry, again establishing feasibility of such approaches.[105] However there with noted limitations in the MW applicators, with further work looking to model the design of more focussed applicators. [106]

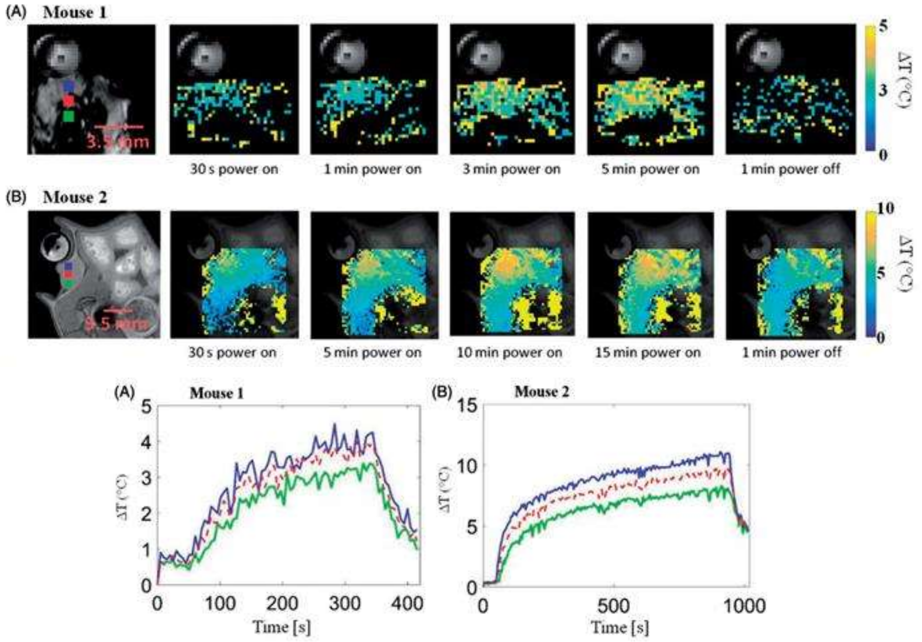

Figure 8 – (Upper Panel) Transient evolution of spatial temperature profiles during and microwave exposure *in vivo* with 20W input power.

(Lower panel) *In vivo* transient temperature profiles within subcutaneous tumours during microwave exposure. Adapted with permission from ref.[105] from the publisher-Taylor & Francis Ltd, http://www.tandfonline.com.

Multiwalled carbon nanotubes (MWNTs) have been extensively characterised for their MW absorption properties.[107–110] With this in mind, recent work[111] has sought to combine these desirable properties with composite nanomaterials (comprising lithium, zinc, cobalt and iron oxide) through integration into the matrix. Further work from this group has explored the microwave properties of Ni-Zn-Co-ferrite nanoparticles that had been similarly encapsulated in MWNTs. [112]

Gold has also been investigated as a material with potential in microwave absorption and hyperthermia. Polymer nanocomposites demonstrated a higher microwave absorption when doped with gold NPs.[113] SU-8 polymer material was mixed with different concentrations of gold NPs and assessed over a frequency range of 0.5 GHz to 20 GHz. Of the two concentrations tested, 2.2 wt.% of gold was demonstrated to be superior in the increasing of microwave absorption, with a small particle size of approximately 4nm. Furthermore, increasing the NP concentration resulted in a more pronounced effect. This has also been observed *in vitro,* where incubation with gold NPs was observed decrease survival rate in cells exposed to a combination of microwave hyperthermia and chemotherapy[114], further inferring their microwave absorption properties. Other recent work includes gold nanoclusters, incubation with which reduced cell viability in combination with microwave radiation applied at 1 GHz.[115] In an interesting recent paper, gold nanostructures were also synthesised with solutions of honey, and subsequently evaluated for their microwave-thermal properties. [116]

Further research has also demonstrated the strength of a combination effect between microwave hyperthermia and targeted drug release, with examples including a cell model study using fullerene. In this study, cell viability was measured an outcome of the application of fullerene which had been encapsulated by specifically designed pluronic F127-chitosan nanoparticles. The cells were demonstrated to uptake the NPs when microwave heating was applied. The overall outcomes demonstrated a more powerful effect on cell viability when the microwave heating and NPs were combined[117]. This may be attributed to the accelerated heating time observed in the presence of fullerene and the potential for a higher intracellular temperature, which is an established effect of this agent.[118] *In vivo* studies have also been conducted with a similar theme, for example the evaluation of self-assembled micelles capable of encapsulating both chemotherapy drugs and magnetic NPs.[119] Here, the micelles were allowed to selectively accumulate in the tumour before the microwave application, with the resultant effect being the triggered drug release alongside tumour temperature increase. This appeared to have a positive impact on tumour volume in the ensuing 19-day observation period. Such *in vivo* studies are not limited to cancer therapy, with work undertaken to evaluate targeted drug delivery for rheumatoid arthritis.[120] This study explored the delivery of novel thermosensitive liposomes loaded with sinomenine hydrochloride paired with MW hyperthermia and demonstrated reduced arthritic scores and pathological features in the combined approach group.

Another novel approach recently described is microwave dynamic therapy. This harnesses the principles of photodynamic therapy, whereby the production of reactive oxygen species is used to destroy cells; an effect that has been noted to be more pronounced in tumour cells.[121] Limitations include poor light penetration depth, which Wu *et al.* [122] have sought to overcome through a combination of microwave irradiation and NPs tested both *in vivo* and *in vitro*. The NPs are zirconium dioxide composite with ionic liquid and liquid metal components and are functionalised with PEG for biocompatibility. The application of these particles demonstrated increased microwave sensitivity postulated to be due to the ionic liquid component, and this in turn meant that an increased thermal effect was seen upon microwave irradiation. Their presence also triggered free radical production which was observed to decrease cell viability. Studies such as these provide an interesting foundation for further research and highlight the capability of microwave sensitive materials in therapeutics. The potential combination with CT imaging for real-time monitoring gives an idea of how therapeutics and imaging in this area can be unified to deliver a targeted solution.

Interestingly, zirconium dioxides have also been suggested as drug delivery vehicles. [123] In this study, ZrO_2 nanospheres were loaded with the cancer therapeutic arsenic trioxide (which functions through the damage of mitochondria), as well as the mitochondrial targeting ligand TPP (triphenylphosphine. The composites were also modified with tetradecanol for temperature sensitive release upon the application of microwave hyperthermia.

There are a small number of studies that suggested metal organic framework NPs for MW hyperthermia. For instance, the Zr metal organic framework or the equivalent nanocube using Mn doped Zr metal organic framework.[124,125] These studies clearly indicate that MW absorption by NPs can be tuned. NP chemists can design materials of high dielectric constant and conductivity that are biocompatible with tuned MW absorption properties.

As mentioned earlier, MW hyperthermia has been identified as an immunotherapy candidate. This has recently been investigated in combination with microwave-sensitive composite NPs and bovine lactoferricin; a cationic anti-cancer peptide[126], which has been evidenced to cause tumour cell death as well as inducing an enhanced immune response. Due to degradation, application of cationic anti-cancer peptides has proved challenging. This study explores PEG-coated thermal and pH sensitive NPs to act as carriers, negating this effect. Again, the MW absorption of these materials produces an enhanced thermal effect, and we see the combined effect of the therapeutic delivery and heating in the causation of tumour cell death. Figure 9 depicts a selection of nanomaterials that have been tested with MW hyperthermia. Similar to MW imaging these materials represent variable chemical composition.

Nanomaterial type	Composition	Size	Shape	Surface	References
Iron Oxides	Magnetite Fe_3O_4	10nm (in water)	Spherical	Not specified	[101]
	Core/shell Fe/Fe_3O_4	10nm; 20nm	Spherical	Dopamine-coated	[104]
Multiwalled carbon nanotubes (MWNTs)	$Li_{0.3}Zn_{0.3}Co_{0.1}Fe_{2.3}O_4$ doped MWNT	Average matrix diameter 30-50nm (range of NP crystallite sizes)	Rod	Not specified	[111]
	Ni-Zn-Co-ferrite doped MWNT	Average matrix diameter 30-50nm (NP crystallite size of ~34.7 nm)	Rod	Not specified	[112]
Gold	SU-8 Polymer nanocomposites doped with Gold NPs	Approximately 4nm	Spherical	Not specified	[113]
	Gold NPs	20nm; 40nm	Spherical	Not specified	[114]
Zirconium	Zirconium dioxide composite with ionic liquid and liquid metal components	210 +/- 60nm	Spherical	PEG	[122]
	Zirconium Metal Organic Framework doped with Mn	Average size of 60nm	Nanocubes	PEG-$(NH_2)_2$	[124]

Figure 9 - Examples of nanomaterials tested for MW hyperthermia that represent variable chemical composition.

1.8 Summary and outlook

The development of medical devices for imaging and sensing is a significant multidisciplinary mission that suggests a holistic approach. Achieving this will require a combination of theoretical physical and biological knowledge, along with an understanding of the regulatory and market adoption avenues. In the event that these modalities adopt companion nanomaterials for contrast enhancement, it is imperative to also consider the material chemical composition, projected human dose, interactions with biological tissue, clearance and most important the safety of these agents.[127] These factors must also be aligned carefully with the imaging system, to fully appreciate detection limits.[128]

Lessons from the development of magnetic resonance imaging strongly indicate that equipment should evolve simultaneously with the chemical and biological development of the nanomaterial. Currently the only safe nanomaterial for contrast enhancement in clinical development is ferumoxytol (a 30nm carbohydrate-coated superparamagnetic iron oxide NP) that has been approved by FDA in 2009 for iron replacement.[129,130] Given this regulatory approval and the potential that ferumoxytol has demonstrated in MRI, it seems likely that iron oxide NPs will be tested in clinical trials of MW imaging/sensing and hyperthermia.

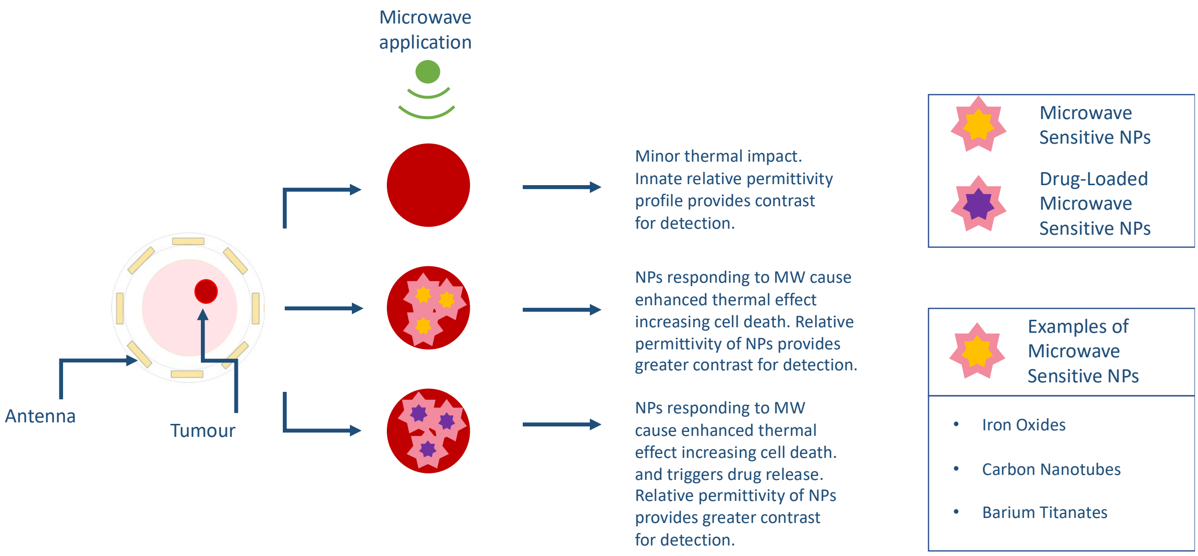

Minor thermal impact. Innate relative permittivity profile provides contrast for detection.

NPs responding to MW cause enhanced thermal effect increasing cell death. Relative permittivity of NPs provides greater contrast for detection.

NPs responding to MW cause enhanced thermal effect increasing cell death. and triggers drug release. Relative permittivity of NPs provides greater contrast for detection.

- Iron Oxides
- Carbon Nanotubes
- Barium Titanates

Figure 10 - Overview of the use of nanoparticles in microwave imaging/sensing and hyperthermia.

While well-characterised for the MW absorption properties, questions remain over the biocompatibility of carbon nanotubes and therefore their ability to be successfully used as contrast agents. Despite this, it is difficult to envisage that carbon nanotubes will be tested in a clinical setting as their toxicological profile indicates the risks outweigh the benefit.[131] Should suitable modification for biocompatibility and clearance achievable however, it is clear from their unique properties that this nanomaterial should be investigated for MW contrast enhancement and hyperthermia. As a further challenge to development, the various biocompatible versions of CNT would have to be continuously monitored throughout to ensure that the chemical functionalisation does not affect their properties of absorbing MW energy.

Devices based on MW technologies can provide treatment through modification of tissue temperature. In oncology, hyperthermia is used to sensitize tumour cells, making the cancerous tissue more susceptible to chemotherapy and radiotherapy. The key challenge with MW hyperthermia devices is the inability to focus as they apply hyperthermia regionally within tissues, and this continues to be a disadvantage for devices currently in development. Nanomaterials that absorb MW radiation could be used to overcome this hurdle through their selective accumulation in the target area, which would provide a temperature increase in this region. The result being a focused and targeted response to applied MW radiation.

For MW to achieve hyperthermic or ablative temperature, iron oxide NPs could be used as they have previously shown promise.[132] Interestingly, the temperature increase of the tumour can be controlled even further using certain types and sizes of iron oxides. The application of iron oxide NPs with MW hyperthermia is one that has attracted significant attention, mainly due to the known safety of iron oxide NPs. Various methods are suggested for the design of NP assisted MW hyperthermia including computational methods.[133]

In a similar way, gold nanoparticle-enhanced MW hyperthermia could offer better clinical translation due to the biocompatibility of the gold and its potential to induce more local effects such as the production of free radicals.[114,134]

Overall, there are a number of materials that have shown promise in the development of nanoparticle-enhanced MW imaging and hyperthermia. There are, however, challenges that need to be overcome, primarily a firm knowledge base in the dielectric constant of both healthy and malignant tissues. Current data are limited and based on excised tissues from surgeries. The accuracy of these measurements has been called into question due to the fact that the tissue hydration plays an important role on dielectric constant.[135] The second challenge that scientists need to address is the direct correlation between tumour NP concentration, NP and tissue dielectric properties and MW frequencies.

Recent improvements in MW devices have allowed progression to clinical trial in applications such as breast cancer. Sensitivity of the MW imaging devices could be increased with companion NPs, with candidates such as iron oxides and ferrites, to alter the dielectric properties. Similar NPs could be used for MW hyperthermia controlling this way the increase of the temperature only in the targeted lesion.

As with any emerging technology, more research is required to support success and address unmet medical need. Running parallel with this is the ongoing development in MW hyperthermia, with associated microwave-sensitive materials that seeks to improve therapeutics, particularly in combination with controlled drug release. As the field moves in this direction, the potential for combined imaging and targeted therapy through the use of NPs has become the goal, offering a new clinical outlook for MW research.

2: Exploring zinc ferrite nanoparticles as contrast agents for microwave imaging/sensing

2.1 Introduction

MW imaging/sensing is an emerging modality that focuses on the dielectric profiles of tissues. Potential applications include breast cancer, where research has progressed to clinical systems, based on the heterogenous properties of different types of breast tissues.[27,136,137] Early research in the field identified significant contrast between healthy and malignant tissues.[40,138] However, variance in breast tissue composition between individuals presents a significant challenge in the field, with *ex vivo* studies suggesting contrast between fibroglandular and malignant tissues can be as low as 10% in some individuals relative to the proportion of fat in the tissue sample. [139,140] Research, therefore, has begun to explore the potential of NPs as contrast enhancers for MW imaging/sensing. These NPs could be used to enhance the innate contrast between tissues allowing for a more sensitive imagine modality. A range of NPs have therefore been characterised for their dielectric properties with a view to their application as dielectric contrast enhancers. These include barium titanates[76,78], titanium dioxides[141] and carbon nanotubes.[65,69,111]

Relevant to this research, magnetic nanoparticles (MNPs) have been investigated for their dielectric properties.[142,143] MNPs have also been identified as heat attenuators in thermal therapies,[144] with downstream potential to combine with MWHT. Iron oxide nanoparticles are MNPs widely studied in biomedical settings and have extensive applications through diagnostics, theranostics and therapy; notably MRI.[145,146]

Research in our group has focused primarily on iron oxide and zinc ferrite NPs, with formulations tested in water, 60% glycerol phantoms and solid tumour phantoms.[61] In one study, ferrites functionalised with polymer PMAO (Poly(maleic anhydride-alt-1-octadecene)) were synthesised using varying zinc concentration and compared with commercially available iron oxides. While observed contrast in commercial iron oxides was negligible compared to water, synthesised zinc ferrite nanoparticles showed changes of up to 5.4% in the dielectric constant. This behaviour is hypothesised to be due to polarisation, with increases in conductivity attributed to electron hopping mechanisms and conductivity of the surface polymer.[147,148] This work highlights the need for further exploration of zinc ferrite nanoparticles as dielectric contrast enhancers.

Previous work has also investigated the potential of zinc oxide nanoparticles as MW contrast-enhancing agents. [62] In this study, aqueous suspensions of silicon dioxide, carbon nanotubes and zinc oxides were assessed for their dielectric properties using the open-ended coaxial probe method. From these data, it was shown that ZnO-PEG dispersions in RO water at a concentration of 2 mg/mL increased the dielectric constant relative to water by 6.80%. The addition of the surface PEG to the ZnO nanoparticles increased stability of the dispersions, but also had the interesting impact of increasing the dielectric constant. This study highlights the importance of surface coating on potential dielectric contrast enhancers.

2.1.1 Outline

In this chapter, we explore polymer-coated zinc ferrite nanoparticles as contrast agents for MW imaging/sensing. Zinc ferrite nanoparticles were initially synthesised by thermal decomposition. The method used was adapted from previous work in the research group.[61] Following synthesis, each ferrite composition was initially coated with PMAO to allow solubility in water, and subsequently assessed size and Fe and Zn content. Dielectric characterization for each composition was undertaken; that which was giving the greatest contrast relative to control was identified, to provide a foundation for further experiments.

When evaluating dielectric contrast enhancers, significant contrast should be noticeable as a change in the dielectric constant of the material under test. The imaginary part or loss index is associated with the dissipation of energy (as heat) when an EM field is applied. Changes in the imaginary component are less desirable for MW sensing/imaging, as it could lead to signal loss. Finding an effective balance between these properties is essential for nanomaterials applied as dual imaging and hyperthermia agents. Results presented throughout this chapter will include the dielectric constant (ε), imaginary (ε”) and effective conductivity S/m (σ) of tested materials. For the purposes of MW imaging/sensing the change in dielectric constant is most relevant, conversely, potential agents for MWHT could show increases in imaginary or effective conductivity, which is linked to the later chapters of this thesis.

Coating the nanoparticles is an essential step for bioavailability, with PMAO (Poly(maleic anhydride-alt-1-octadecene)) coating forming the basis for the previous work undertaken in my research group.[61] To better understand the relationship between the polymer chosen for phase transfer and downstream dielectric characterization, three different polymers were used to coat the synthesized zinc ferrites: PSMA (Poly(styrene-co-maleic anhydride)), PEDOT:PSS (Poly(3,4-ethylenedioxythiophene)-poly(styrenesulfonate)). and PMAO (Poly(maleic anhydride-alt-1-octadecene)). Following dielectric characterisation in water and 60% glycerol phantoms, a candidate composition for progression to *ex vivo* and *in vivo* experimentation was identified and assessed by TEM and DLS (size and stability).

2.2 Aim & Objectives

2.2.1 Aim

To evaluate polymer-coated zinc ferrite nanoparticles for their dielectric properties with a view to their application as dielectric contrast enhancers.

2.2.2 Objectives

1) To synthesize PMAO-coated zinc ferrite nanoparticles with varying concentrations of zinc (Zn).
2) To functionalize the surface of synthesised zinc ferrite nanoparticles with different polymers: PMAO (Poly(maleic anhydride-alt-1-octadecene)); PSMA (Poly(styrene-co-maleic anhydride)); PEDOT:PSS (Poly(3,4-ethylenedioxythiophene)-poly(styrenesulfonate)).
3) To evaluate the dielectric properties and conductivity of functionalized zinc ferrite nanoparticles in water and 60% glycerol phantoms, identifying a candidate for future *ex vivo* and *in vivo* characterisation.
4) To assess the colloidal stability of functionalized zinc ferrite nanoparticles in water using DLS over 30 days.
5) To characterize final selected composition using TEM.

2.3 Results & Discussion

2.3.1 Synthesis of zinc ferrite nanoparticles

Zinc ferrite nanoparticles were synthesised by thermal decomposition. Full details of the preparation and subsequent phase transfer can be found in Materials and Methods. Briefly, zinc ferrite nanoparticles were synthesised by thermal decomposition. The amount of iron precursor was kept consistent in all batches. The amount of zinc was varied to achieve different compositions. All three compositions were coated with PMAO (Poly(maleic anhydride-alt-1-octadecene)) using an established maleic anhydride coupling mechanism[149] to allow water solubility. Particles were suspended to a final concentration of 0.06 mg/mL in diH_2O. ICP-OES was used to determine Zn and Fe ratios in each composition. Size and PDI of coated particles were determined by DLS measurements. Results are shown in Figure 11.

Formulation	**Z-average size /nm**	**PDI**
[PMAO]-$Zn_{0.03}Fe_2O_4$	109.9 (+/- 2.6)	0.29 (+/- 0.03)
[PMAO]-$Zn_{0.06}Fe_2O_4$	92.15 (+/- 1.8)	0.28 (+/-0.02)
[PMAO]-$Zn_{0.09}Fe_2O_4$	104.8 (+/- 3.9)	0.43 (+/-0.04)

Figure 11 - Characteristics of synthesised PMAO-coated zinc ferrite nanoparticles. The table shows the formulation and measured z-average and PDI by DLS of PMAO-coated particles. Values shown are the calculated average of 3 individual DLS measurements +/- SD.

PMAO-coated zinc ferrite nanoparticles show a z-average size of between approximately 90-110 nm. PDI values ranged from 0.28 to 0.43, with the composition containing the highest zinc content showing the highest polydispersity index.

2.3.3 Dielectric properties in water

Measurements were taken using a Keysight potable two-port VNA over a frequency range of 0.5-4 GHz. All measurement used a Keysight slim-form co-axial probe. Full details can be found in Materials and Methods. It is important to note that the visible ‘jumps’ seen in the profiles are caused by systematic errors in frequency dispersion which are common in the coaxial probe technique due to susceptibility to systematic errors especially at low frequencies.[62] Every effort was made to minimise this through frequent calibration of the system using a standard air, short, water protocol. Briefly, PMAO-coated zinc ferrite nanoparticles were analysed for their dielectric properties using the open-ended co-axial probe technique using a slim-form probe. All compositions were suspended to a final concentration of 0.06 mg/mL in diH_2O at a minimum volume of 5 mL to ensure appropriate immersion of the slim form probe. Results are displayed in Figure 12.

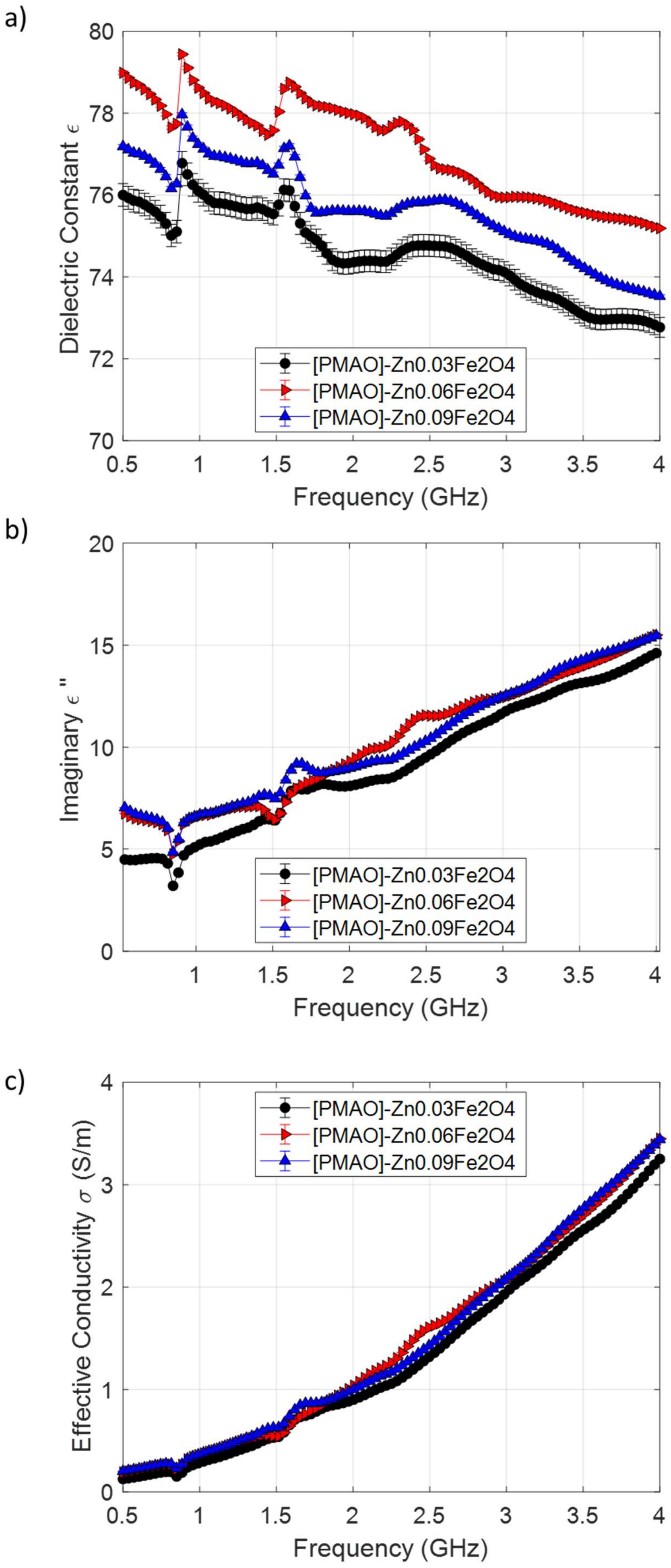
a)
Dielectric Constant ε
80
78
76
74
72
70
0.5
1
1.5
2
2.5
3
3.5
4
Frequency (GHz)
[PMAO]-Zn0.03Fe2O4
[PMAO]-Zn0.06Fe2O4
[PMAO]-Zn0.09Fe2O4
b)
Imaginary ε ''
20
15
10
5
0
1
1.5
2
2.5
3
3.5
4
Frequency (GHz)
[PMAO]-Zn0.03Fe2O4
[PMAO]-Zn0.06Fe2O4
[PMAO]-Zn0.09Fe2O4
c)
Effective Conductivity σ (S/m)
4
3
2
1
0
0.5
1
1.5
2
2.5
3
3.5
4
Frequency (GHz)
[PMAO]-Zn0.03Fe2O4
[PMAO]-Zn0.06Fe2O4
[PMAO]-Zn0.09Fe2O4

Figure 12 - Graphs showing measured a) dielectric constant (ε), b) imaginary (ε”) and c) effective conductivity S/m (σ) of [PMAO]-$Zn_{0.03}Fe_2O_4$, [PMAO]-$Zn_{0.06}Fe_2O_4$ [PMAO]-$Zn_{0.09}Fe_2O_4$ nanoparticles in diH_2O at a concentration of 0.06 mg/mL. For each sample, 10 consecutive measurements were taken using a slim-form co-axial probe in the same position. Plots show an average calculated from measurements.

From the graph we can see three distinct profiles relating to dielectric constant. At 2.45 GHz the measured dielectric constant values were 74.7, 77.1 and 75.8 respective to the $Zn_{0.03}$, $Zn_{0.06}$ and $Zn_{0.09}$ compositions. Interestingly, the imaginary profiles for each composition vary slightly with $Zn_{0.06}$ and $Zn_{0.09}$ compositions showing elevation at frequencies <1 GHz when compared to the $Zn_{0.03}$. Imaginary profiles tend to increase with frequency, as dielectric constant profiles decrease. All measured samples show similar conductivity profiles, with no significant difference observed between formulations.

While there is no directly comparable published data for this nanoparticle composition, previous work in the group examined higher zinc ratios; [($Zn_{0.18}$ $Fe_{0.82}$) Fe_2O_4]-PMAO and [($Zn_{0.39}Fe_{0.61}$)Fe_2O4]-PMAO.[61] Measured dielectric constant for these compositions was slightly higher than we have observed, with a dielectric constant value of approximately 81 at 2.45 GHz in the [($Zn_{0.18}$ $Fe_{0.82}$) Fe_2O_4]-PMAO formulation . It is important to note however that a significantly higher concentration of 2 mg/mL was used. Conductivity and imaginary profiles are not shared in this publication and so cannot be cross compared.

As the nanoparticles as are suspended in water, it is important to compare dielectric properties relative to this. However, it should be considered the measured dielectric constant and effective conductivity values of breast tumour tissue at 2.45 GHz have been reported as in the region of 60 and 2.5 S/m respectively.[150] Therefore $Zn_{0.06}$ composition would show the greatest increase in dielectric constant relative to this value. With interest in combining with MWHT in downstream experiments, this composition also shows the desired alteration in imaginary profile, as well as a smaller size and PDI. Therefore, the $Zn_{0.06}$ composition was selected for further experiments.

2.3.4 Polymer variation

Previous studies have hypothesised that the dielectric profile of zinc ferrites is influenced by the surface polymer. [61,62,147,148] In order to understand the impact of the chosen coating on the dielectric profile of the formulation, alternative polymer coatings were explored. As a reproducible method for phase transfer had been established via maleic anhydride coupling, a further amphiphilic polymer was selected to allow coupling with the same mechanism; PSMA (Poly(styrene-co-maleic anhydride)).

Formulation	**z-average size /nm**	**PDI**
[PMAO]-$Zn_{0.06}Fe_2O_4$	92.2 (+/- 1.8)	0.28 (+/-0.02)
[PSMA]-$Zn_{0.06}Fe_2O_4$	68.1 (+/- 1.2)	0.18 (+/- 0.01)

Figure 13 - Characteristics of synthesised PMAO- and PSMA-coated zinc ferrite nanoparticles. The table shows the formulation and measured z-average and PDI by DLS of coated particles. Values shown are the calculated average of 3 individual DLS measurements +/- SD.

Following size measurements, [PMAO]-$Zn_{0.06}Fe_2O_4$ and [PSMA]-$Zn_{0.06}Fe_2O_4$ nanoparticles were assessed for their dielectric properties in diH_2O. Measurements were taken using a Keysight potable two-port VNA over a frequency range of 0.5-4 GHz. All measurement used a Keysight slim-form co-axial probe. Full details can be found in Materials and Methods. Briefly, coated zinc ferrite nanoparticles were analysed for their dielectric properties using the open-ended co-axial probe technique using a slim-form probe. All samples were a minimum volume of 5 mL to ensure appropriate immersion of the slim form probe. Both compositions were suspended to a final concentration of 0.06 mg/mL.

a)

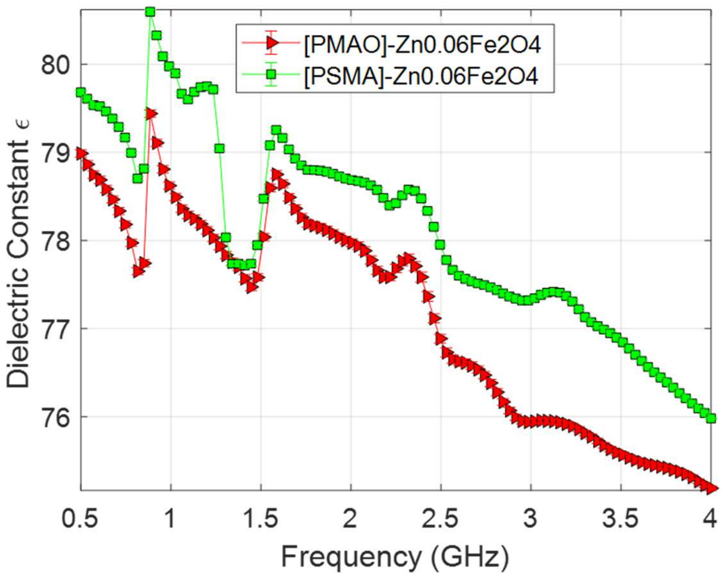
[PMAO]-Zn0.06Fe2O4
[PSMA]-Zn0.06Fe2O4
Dielectric Constant ϵ
76
77
78
79
80
0.5
1
1.5
2
2.5
3
3.5
4
Frequency (GHz)

b)

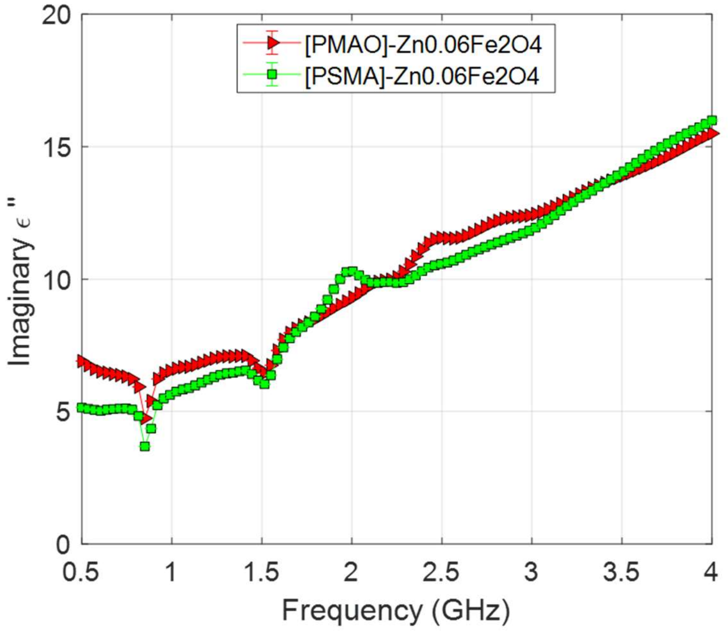
[PMAO]-Zn0.06Fe2O4
[PSMA]-Zn0.06Fe2O4
Imaginary ϵ "
0
5
10
15
20
0.5
1
1.5
2
2.5
3
3.5
4
Frequency (GHz)

c)

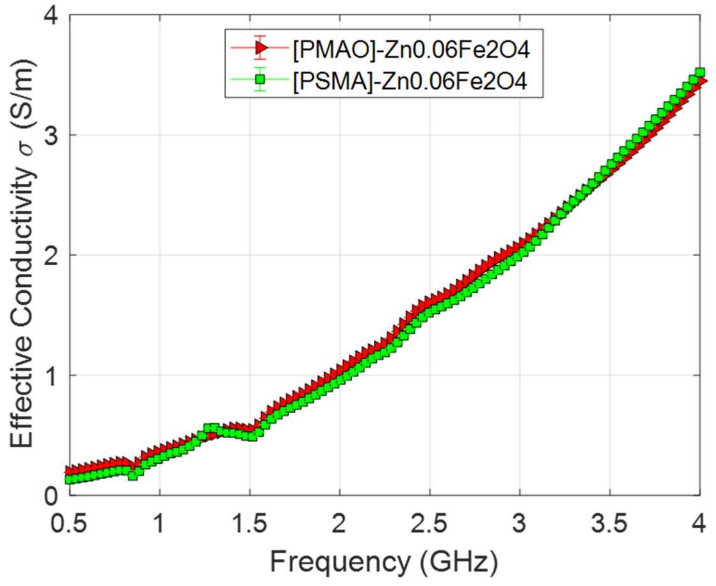
[PMAO]-Zn0.06Fe2O4
[PSMA]-Zn0.06Fe2O4
Effective Conductivity σ (S/m)
0
1
2
3
4
0.5
1
1.5
2
2.5
3
3.5
4
Frequency (GHz)

Figure 14 - Graphs showing measured a) dielectric constant (ε), b) imaginary (ε”) and c) effective conductivity S/m (σ) of [PMAO]-$Zn_{0.06}Fe_2O_4$ and [PSMA]-$Zn_{0.06}Fe_2O_4$ nanoparticles in diH_2O at a concentration of 0.06 mg/mL. For each sample, 10 consecutive measurements were taken using a slim-form co-axial probe in the same position. Plots show an average calculated from measurements.

From the graph we can see two distinct profiles relating to dielectric constant. At 2.45 GHz the measured dielectric constant were 76.8 and 78.1 respective to the PMAO and PSMA compositions. This shows an interesting variation with an increase of 1.3 observed when coated with PSMA. Differences are also seen in the imaginary profile, where at frequencies less than 1 GHz, the PMAO composition shows an imaginary value of 6.1 vs 5.1 for PSMA compositions at 0.5 GHz. At frequencies above 1 GHz the imaginary profile for both polymer coatings are observed to be similar interestingly measured effective conductivity for both compositions is relatively low, measured at 1.6 S/m and 1.5 S/m for PMAO and PSMA respectively at 2.45 GHz. It should be noted that these measurements were taken at a low concentration of 0.06 mg/mL with downstream translation in mind; further experiments with more concentrated particles may give a clearer indication of the dielectric properties.

Previous publications have examined higher concentrations of 2 mg/mL of nanoparticles when evaluating contrast agents.[61] Finding the balance between effective contrast and injectable concentration can be a challenge, with high concentrations difficult to translate to *in vivo* or clinical settings. While the low concentration of 0.06 mg/mL zinc ferrites showed some changes to the dielectric properties relative to water, concentrating the nanoparticles may give further indications of their behaviour. The [PMAO]-$Zn_{0.06}Fe_2O_4$ and [PSMA]-$Zn_{0.06}Fe_2O_4$ nanoparticles were therefore concentrated using centrifugal filter units (Amicon® Ultra-15) to achieve a final concentration of 0.6 mg/mL in diH_2O. This concentration was chosen as a ten-fold increase on the previous experiments, while still maintaining a reduction relative to previous experiments. Dielectric properties of the concentrated nanoparticles were then assessed. Measurements were taken using a Keysight potable two-port VNA over a frequency range of 0.5-4 GHz. All measurement used a Keysight slim-form co-axial probe. Full details can be found in Materials and Methods. Briefly, coated zinc ferrite nanoparticles were analysed for their dielectric properties using the open-ended co-axial probe technique using a slim-form probe. All samples were a minimum volume of 5 mL to ensure appropriate immersion of the slim form probe. Results are shown in Figure 15.

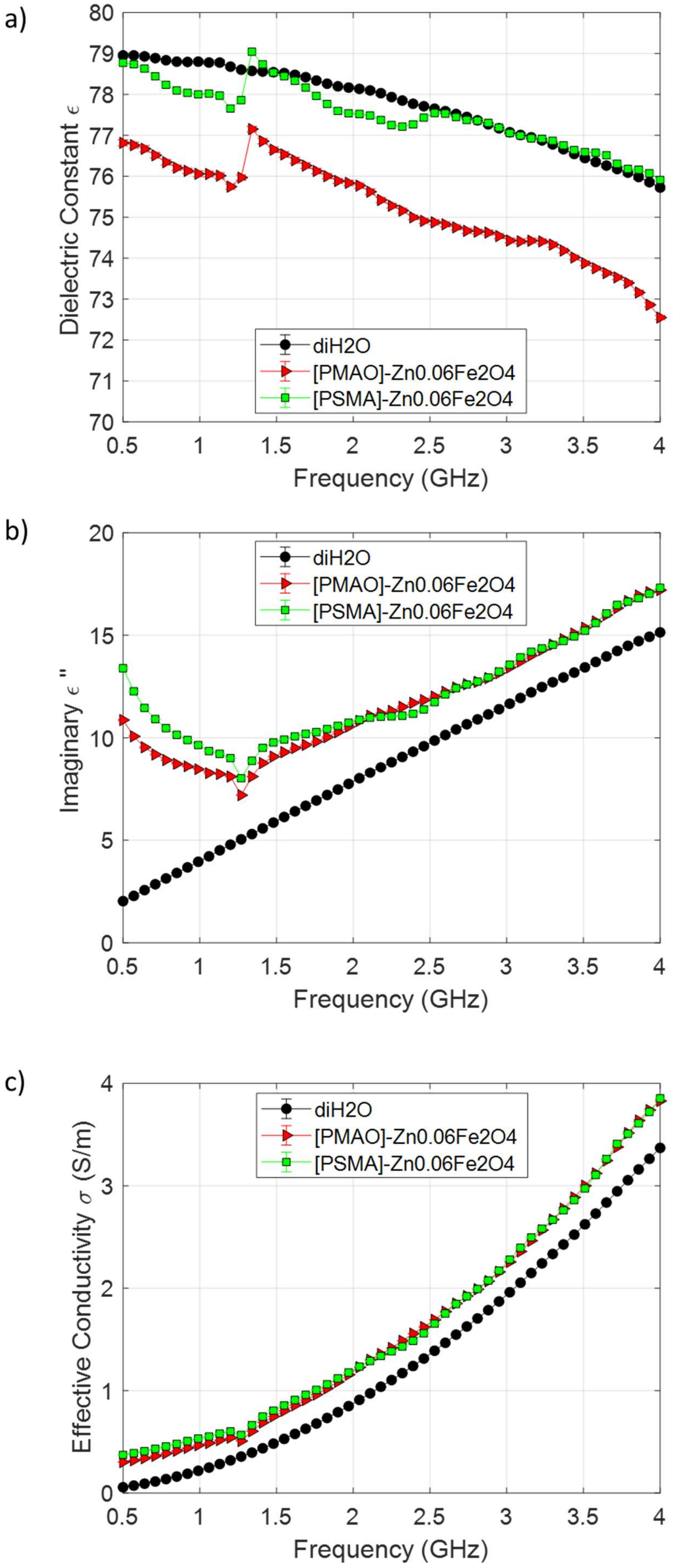
a)
Dielectric Constant ϵ
80
79
78
77
76
75
74
73
72
71
70
0.5
1
1.5
2
2.5
3
3.5
4
Frequency (GHz)
diH2O
[PMAO]-Zn0.06Fe2O4
[PSMA]-Zn0.06Fe2O4
b)
Imaginary ϵ"
20
15
10
5
0
0.5
1
1.5
2
2.5
3
3.5
4
Frequency (GHz)
diH2O
[PMAO]-Zn0.06Fe2O4
[PSMA]-Zn0.06Fe2O4
c)
Effective Conductivity σ (S/m)
4
3
2
1
0
0.5
1
1.5
2
2.5
3
3.5
4
Frequency (GHz)
diH2O
[PMAO]-Zn0.06Fe2O4
[PSMA]-Zn0.06Fe2O4

Figure 15 - Graphs showing measured a) dielectric constant (ε), b) imaginary (ε”) and c) effective conductivity S/m (σ) of [PMAO]-$Zn_{0.06}Fe_2O_4$ and [PSMA]-$Zn_{0.06}Fe_2O_4$ nanoparticles in diH_2O at a concentration of 0.6 mg/mL. For each sample, 10 consecutive measurements were taken using a slim-form co-axial probe in the same position. Plots show an average calculated from measurements.

From the graphs, we can see that PSMA-coated zinc ferrites and PMAO-coated ferrites show distinct profiles. A comparison to water is shown in the graph which highlights this change. At 2.45 GHz the measured dielectric constant were 74.9 and 77.4 respective to the PMAO and PSMA compositions. This shows an interesting variation, with an increase of 2.5 relative to the value observed when coated with PMAO. Furthermore, this is greater than the difference observed at lower concentrations of the same formulation. Interestingly, both formulations showed a noted decrease in overall measured dielectric constant when more concentrated. These findings indicate that certain properties could have a direct relationship with concentration. As the goal for these particles is *in vivo* translation higher concentrations were not explored. A similar observation is made in imaginary profiles. Both compositions show notably higher imaginary values at frequencies less than 1 GHz, than their less concentrated counterparts. Most interestingly, the conductivity values did not follow this trend. Despite a tenfold increase in concentration measured conductivity values were measured to be 1.6 S/m and 1.5 S/m for PMAO and PSMA respectively at 2.45 GHz. This is the same as was measured for the 0.06mg/ml solutions.

2.3.6 Polymer variation: PEDOT:PSS

PEDOT:PSS is a conductive polymer commonly used in electronics, that has been explored as a nanocomposite material with iron oxide nanoparticles. [151–153] Given the role of polymer coating in the dielectric behaviour of zinc ferrite nanoparticles. In these experiments $Zn_{0.06}Fe_2O_4$ was combined with 3.0-4.0% PEDOT:PSS in H_2O. Full details can be found in Materials and Methods. The reaction showed a low yield, with a final concentration of 0.01 mg/mL of zinc ferrites. Efforts to concentrate this showed aggregation. Given the lower concentration and separate mechanism, this formulation was assessed separately to PMAO and PSMA. Size characterisation by DLS showed a single peak with a z-average size (d.nm) of 115.4 with a PDI of 0.087. Dielectric properties were then assessed. Measurements were taken using a Keysight potable two-port VNA over a frequency range of 0.5-4 GHz. All measurement used a Keysight slim-form co-axial probe. All samples were at a concentration of 0.01 mg/mL at a minimum volume of 5 mL to ensure appropriate immersion of the slim form probe. Results are shown in Figure 16.

a)

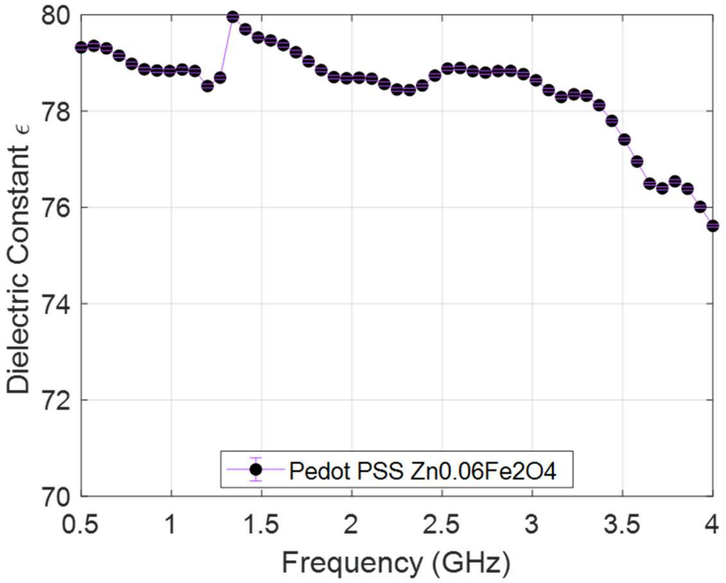
Dielectric Constant ϵ
80
78
76
74
72
70
Pedot PSS Zn0.06Fe2O4
0.5
1
1.5
2
2.5
3
3.5
4
Frequency (GHz)

b)

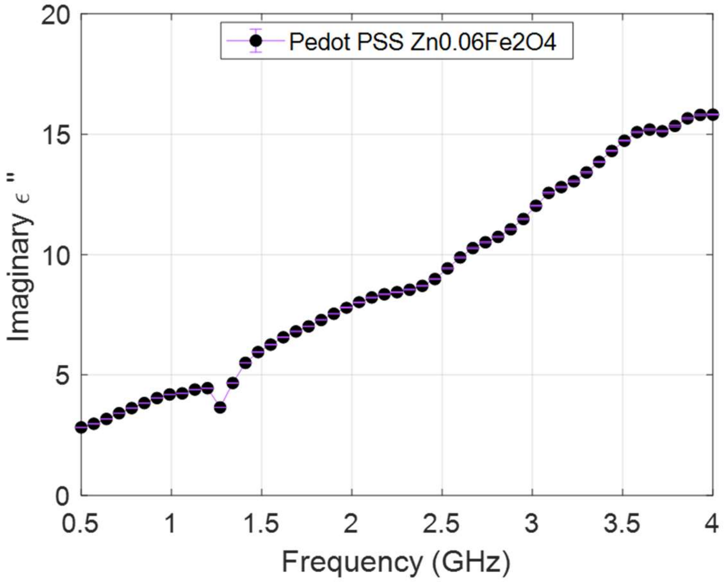
Imaginary ϵ "
20
15
10
5
0
Pedot PSS Zn0.06Fe2O4
0.5
1
1.5
2
2.5
3
3.5
4
Frequency (GHz)

c)

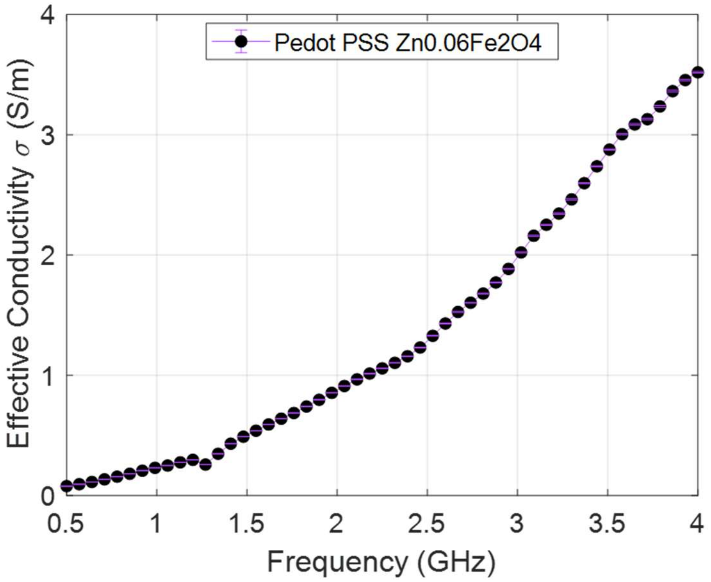
Effective Conductivity σ (S/m)
4
3
2
1
0
Pedot PSS Zn0.06Fe2O4
0.5
1
1.5
2
2.5
3
3.5
4
Frequency (GHz)

Figure 16 - Graphs showing measured a) dielectric constant (ε), b) imaginary (ε") and c) effective conductivity S/m (σ) of PEDOT:PSS $Zn_{0.06}Fe_2O_4$ in diH_2O at a concentration of 0.01 mg/mL. For the sample, 10 consecutive measurements were taken using a slim-form co-axial probe in the same position. Plots show an average calculated from measurements.

At 2.45 GHz the measured dielectric constant 78.7. Effective conductivity at the same frequency was recorded as 1.2 S/m. Imaginary value at 2.45 GHz was recorded to be 8.9. Interestingly this formulation shows similar dielectric constant and imaginary profiles to [PSMA]-$Zn_{0.06}Fe_2O_4$ which was measured at a higher concentration of 0.06 mg/mL. Some small increase in the imaginary profile can be seen relative to water, but this is lower when compared with 0.6 mg/ml suspensions of [PSMA]-$Zn_{0.06}Fe_2O_4$ and [PMAO]-$Zn_{0.06}Fe_2O_4$. Effective conductivity shows little increase relative to previously measured water samples and is less than the measured values for [PSMA]-$Zn_{0.06}Fe_2O_4$ and [PMAO]-$Zn_{0.06}Fe_2O_4$ at either concentration. It was concluded that given the relationship between concentration and dielectric profiles that this formulation was of insufficient concentration for further investigation.

2.3.6 Dielectric properties in 60% glycerol

While the dielectric properties in measured water can give some indication as to the dielectric properties of a formulation, water has a dielectric constant of approximately 80 at 1 GHz, which is not reflective of the dielectric characteristics of the tumour environment. To better understand the dielectric properties of the nanoparticles relative to a tumour environment, phantom model systems are often used, with common phantoms incorporating mixtures of oils and salts to achieve the dielectric properties of relevant tissues. [10,29,154] While solid phantoms can present challenges with the dispersion of nanoparticles, liquid phantoms can provide a more colloidally stable environment for the material under test while still being reflective of the tumour environment. The dielectric properties of a 60% glycerol-water mixture have been demonstrated to be similar to those of breast tumour tissue, with a value of approximately 56.6 measured at 1.0 GHz.[155] 60% glycerol phantoms were therefore selected to further understand the dielectric properties of the synthesised polymer-coated zinc ferrite nanoparticles. Measurements were taken using a Keysight potable two-port VNA over a frequency range of 0.5-4 GHz. All measurement used a Keysight slim-form co-axial probe. Full details can be found in Materials and Methods. Briefly, 0.06 mg/mL PSMA- and PMAO-coated zinc ferrite nanoparticles were analysed for their dielectric properties in 60% glycerol phantoms using the open-ended co-axial probe technique using a slim-form probe. Nanoparticle formulations were incorporated into 60% glycerol phantoms a concentration of and 10% (v/v). Phantoms had a total volume of 5 mL to ensure appropriate immersion of the slim form probe.

a)

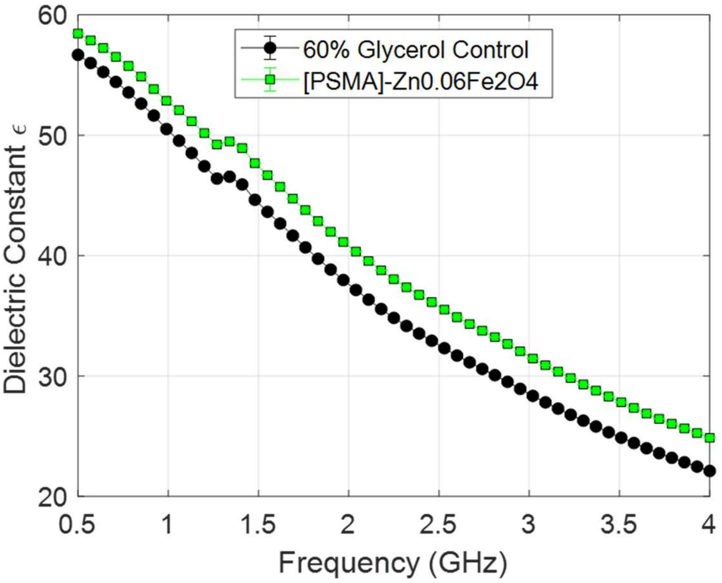
60% Glycerol Control
[PSMA]-Zn0.06Fe2O4
Dielectric Constant ϵ
60
50
40
30
20
0.5
1
1.5
2
2.5
3
3.5
4
Frequency (GHz)

b)

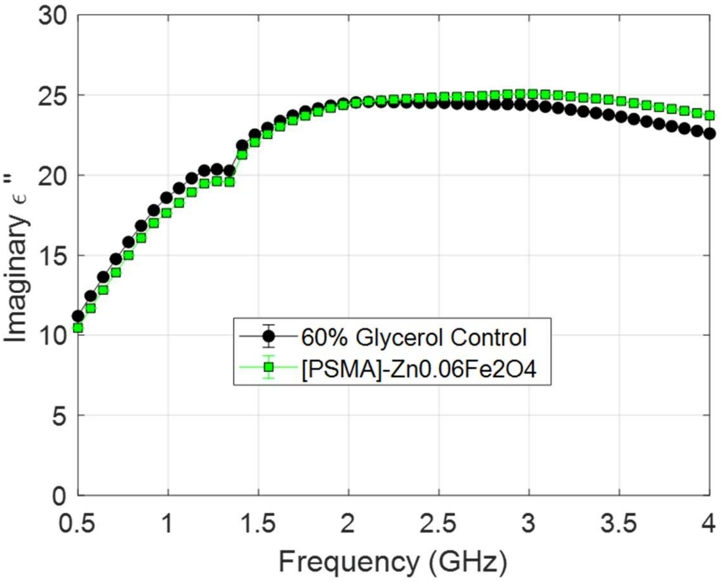
60% Glycerol Control
[PSMA]-Zn0.06Fe2O4
Imaginary ϵ''
30
25
20
15
10
5
0
0.5
1
1.5
2
2.5
3
3.5
4
Frequency (GHz)

c)

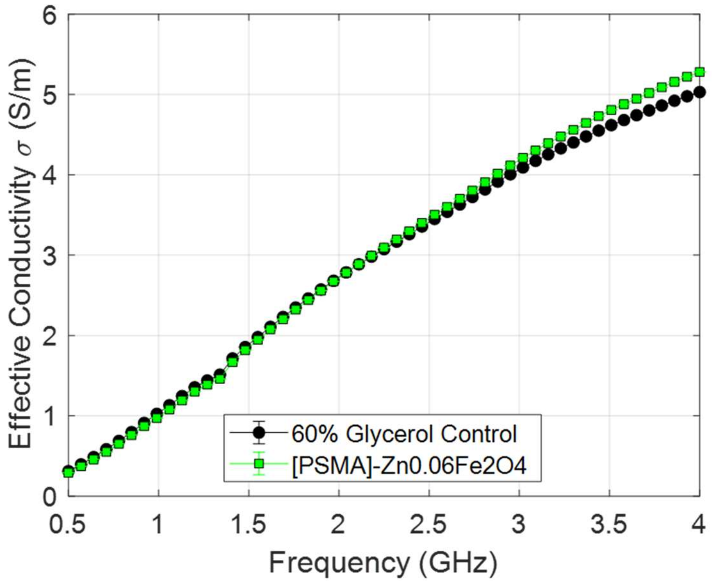
60% Glycerol Control
[PSMA]-Zn0.06Fe2O4
Effective Conductivity σ (S/m)
6
5
4
3
2
1
0
0.5
1
1.5
2
2.5
3
3.5
4
Frequency (GHz)

Figure 17 - Graphs showing measured a) dielectric constant (ε), b) imaginary (ε”) and c) effective conductivity S/m (σ) of [PSMA]-$Zn_{0.06}Fe_2O_4$ in 60% glycerol.

a)

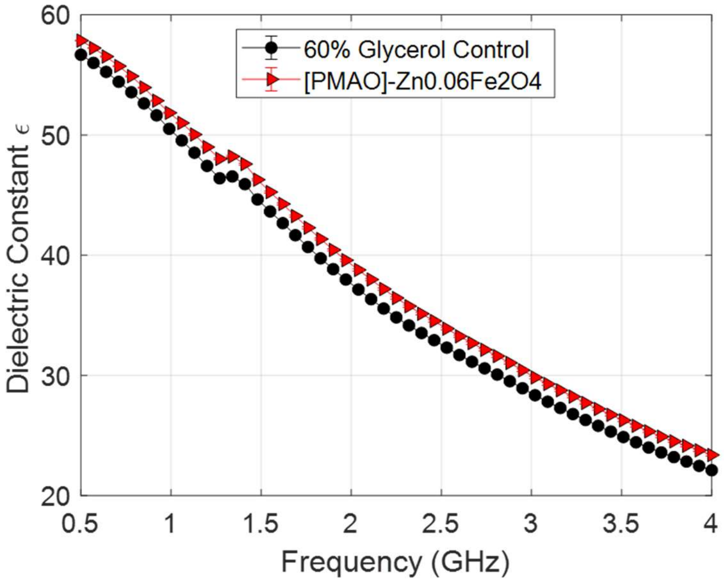
60% Glycerol Control
[PMAO]-Zn0.06Fe2O4
Dielectric Constant ϵ
Frequency (GHz)
60
50
40
30
20
0.5
1
1.5
2
2.5
3
3.5
4

b)

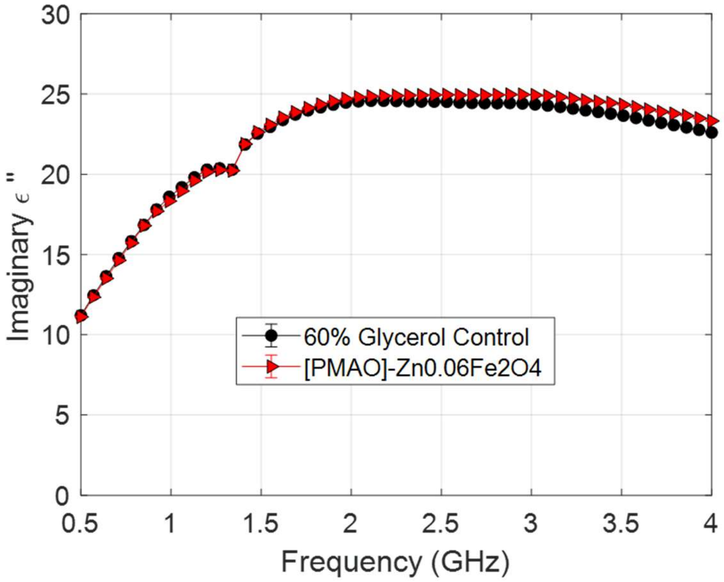
60% Glycerol Control
[PMAO]-Zn0.06Fe2O4
Imaginary ϵ"
Frequency (GHz)
30
25
20
15
10
5
0
0.5
1
1.5
2
2.5
3
3.5
4

c)

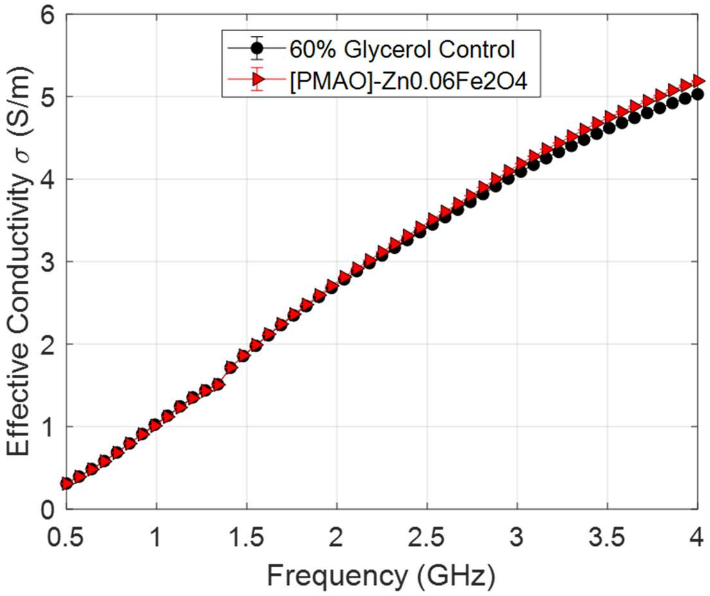
60% Glycerol Control
[PMAO]-Zn0.06Fe2O4
Effective Conductivity σ (S/m)
Frequency (GHz)
6
5
4
3
2
1
0
0.5
1
1.5
2
2.5
3
3.5
4

Figure 18 - Graphs showing measured a) dielectric constant (ε), b) imaginary (ε”) and c) effective conductivity S/m (σ) of [PMAO]-$Zn_{0.06}Fe_2O_4$ in 60% glycerol.

From the graphs in Figure 17 and Figure 18, we can see the measured dielectric properties of [PMAO]-$Zn_{0.06}Fe_2O_4$ and [PSMA]-$Zn_{0.06}Fe_2O_4$ in 60% glycerol in phantoms. At 2.45 GHz, the measured dielectric constant of the glycerol control phantom was 32.9. For phantoms incorporating [PMAO]-$Zn_{0.06}Fe_2O_4$, the measured dielectric constant at this same frequency was 34.5. Interestingly, for [PSMA]-$Zn_{0.06}Fe_2O_4$ this value was 36.1, an increase of 3.1 relative top the control. This is reflective of measurements taken in water which showed [PSMA]-$Zn_{0.06}Fe_2O_4$ to have a higher dielectric constant than [PSMA]-$Zn_{0.06}Fe_2O_4$. From a contrast perspective the increase seen in the presence of zinc ferrite nanoparticles reenforces their potential as dielectric contrast enhancers.

While suspended at a 10% (v/v) concentration in the phantom, concentrations of the nanoparticle solutions prior to addition were 0.06 mg/mL. Therefore, the final concentration of the particles in the phantom would be extremely low, which is reflected in the minimal changes we observe. Nonetheless, the higher dielectric constant observations seen for the [PSMA]-$Zn_{0.06}Fe_2O_4$ relative to the [PMAO]-$Zn_{0.06}Fe_2O_4$ formulations are reflective of the measurements taken in water. Comparing this to previous studies[61], we are seeing less but nevertheless observable contrast, but at almost 4-fold less concentration. While the contrast is lower, the potential of translation is higher, with 0.06 mg/mL reflecting a more achievable injectable dose vs 2 mg/mL.

Based on this combination of experiments, [PSMA]-$Zn_{0.06}Fe_2O_4$ was selected as the candidate formulation for further experiments in living model systems, as it showed a higher measured dielectric constant profile, which is complimentary to application in MW sensing. Before taking this step, the formulation was assessed for stability and imaged using TEM.

2.3.7 Stability of [PSMA]-$Zn_{0.06}Fe_2O_4$

The stability of [PSMA]-$Zn_{0.06}Fe_2O_4$ nanoparticles was assessed in water over time using DLS. This technique includes an output of Z-average (d.nm) and PDI measurements. Z-average gives an indication of the hydrodynamic size while PDI or polydispersity index indicates the dispersion of the particles. A higher PDI indicates that there is a wider range of particle sizes within a given solution, while a desirable lower PDI indicates good dispersion and less variation in size. Initially, a baseline measurement on the day of coating was taken. Subsequent samples were taken every 10 days over a total period of 30 days. Particles remained in suspension during this period, with no sedimentation observed. A minimum of three separate measurements were taken at each timepoint; results are shown in

Figure 19.

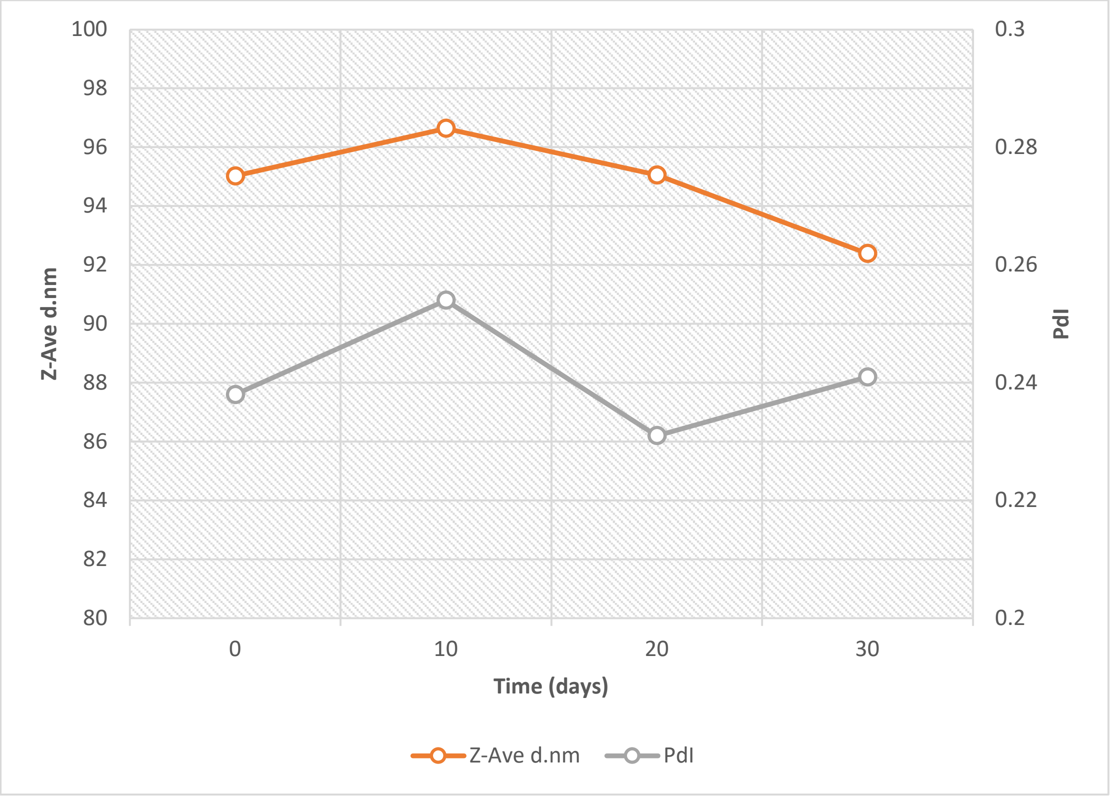

Figure 19 - Z-average size and PDI of [PSMA]-$Zn_{0.06}Fe_2O_4$ nanoparticles measured by DLS in water over a period of 30 days. Each time point is representative of three separate measurements taken on the specified day.

As is demonstrated from the plotted data, minimal variation is seen over the 30-day period in either Z-average (d.nm) or PDI; small variations are to be expected with this measurement technique. Overall, the indication is of a stable formulation in water, suitable for further experiments in living model systems.

2.3.8 TEM of [PSMA]-$Zn_{0.06}Fe_2O_4$

In order to confirm the size and structure of $Zn_{0.06}Fe_2O_4$ uncoated particles dissolved in hexane were assessed by TEM.

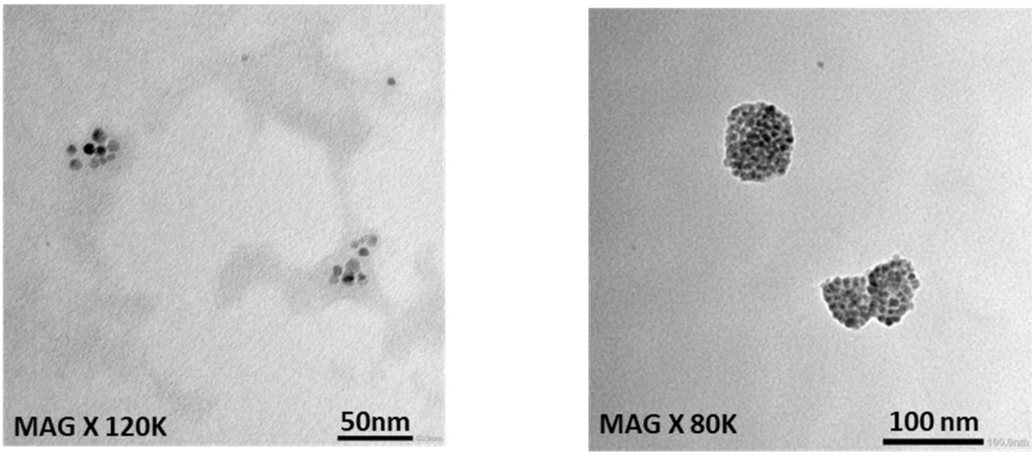

Figure 20 - Characteristics of synthesised $Zn_{0.06}Fe_2O_4$ nanoparticles. Panels show TEM images of the uncoated particles taken at X120K and X80K.

From the TEM images in Figure 20, we can see predominantly spherical nanoparticles approximately 10 nm in size.

2.4 Conclusion

In conclusion, coated zinc ferrite nanoparticles were assessed for their dielectric properties. Measurements determined $Zn_{0.06}Fe_2O_4$ showed increased dielectric constant relative to other zinc concentrations. This is in line with published literature indicating the impact of zinc concentration on dielectric constant.[61] Further investigations exploring alternative polymer coatings identified PSMA-coated zinc ferrite nanoparticles as giving a higher measured dielectric constant relative to their PMAO counterparts. This was explored at two different concentrations and in both water and 60% glycerol phantoms, with similar observations. A study conducted in water confirmed the stability of [PSMA]-$Zn_{0.06}Fe_2O_4$ in water over a period of 30 days, with minimal observed fluctuations in Z-average (d.nm) and PDI. Finally, TEM images of the uncoated particles confirm a spherical shape approximately 10 nm in size. Overall, these data further confirm zinc ferrite nanoparticles as candidate contrast agents for MW imaging/sensing and the impact of polymer coating choice on the downstream dielectric properties. From these experiments we also identified a specific formulation ([PSMA]-$Zn_{0.06}Fe_2O_4$) for further experiments in living model systems.

3: *In vitro, ex vivo* and *in vivo* model systems for contrast agents in microwave (MW) imaging/sensing

It should be noted that a portion of this chapter is adapted from our publication:

A.J. Wilson, P. Kosmas and M. Thanou, "Ex-vivo Dielectric Properties of Tissues in Athymic Nude Mice," 2022 3rd URSI Atlantic and Asia Pacific Radio Science Meeting (AT-AP-RASC), 2022, pp. 1-4, doi: 10.23919/AT-AP-RASC54737.2022.9814269.

3.1 Introduction

Microwave (MW) imaging/sensing systems show promise in providing a low-cost alternative for tumour detection without the use of ionising radiation. Central to the technology is the innate difference in dielectric properties observed between surrounding and target tissues. In some applications such as breast cancer, however, contrast between healthy and malignant tissues has been noted to be as low as 10%[139,140], varying individual to individual. Breast tissue is very heterogenous[156], and areas with higher water content such as the mammary glands will show a higher measured dielectric constant than for example adipose tissue. Breast density is also an important consideration; dense breasts contain large proportions of fibroglandular tissue and therefore show higher dielectric properties to breast with a higher proportion of fat content.[137] With this in mind, an accurate understanding of the dielectric properties of living tissues continues to be an essential element in this research area. In addition to the development of imaging/sensing platforms, these values of these dielectric properties form the basis of model systems that are key to the verification of developmental MW systems.

Early studies exploring dielectric characterisation of tissues formed the foundation for the wide knowledge base now available.[157–161] More recent work now encompasses an even wider range of measurement techniques and technologies across several model organisms.

Cells have also been explored as a model system, with studies aiming to identify if different populations of cells exhibit different dielectric signatures. This hypothesis would indicate that a contribution to the dielectric profile of a tissue is made by its component cells, potentially as a result of cell polarisation.[162] Specific to this project, breast cancer cells have been characterized using the co-axial probe technique.[51] Cells from different cancerous and healthy lines were seeded at a density of $4x10^5$ were seeded to form a monolayer on 12-well plates for 24 hours and then washed and resuspended in 1 mL culture media and subsequently analysed for their dielectric properties between 200 MHz and 13.6 GHz. Reported outcomes of the study state that normal and cancerous cells lines displayed distinct signatures including MDA-MB-231, a triple negative breast cancer cell line that has formed the basis of much of the modelling in this project. Cells in suspension have also been characterised, with one such study comparing the capacitance of cancer cell lines when compared to normal cells.[52] As with the previous study, it was noted that contrasting electrical properties observed between cancer cells and their normal counterparts as well as different signatures between one another, with an overall trend showing cancerous cell lines to have a general reduction in capacitance.

Detailed studies have covered the dielectric properties of a broad spectrum of tissues including the heart[163], brain[164,165] and liver[150,166,167], amongst many others. Specific to this project, the dielectric properties of tumours have been explored across small animal models.[168–170]

While model systems form such a key part of this research, inconsistency in reported values has been a challenge in the field, with several previous studies having explored the factors leading to variability in published dielectric tissue measurements. In addition to this, many studies use excised tissues, with some authors raising the question of whether these are comparable to the *in-situ* properties, due to factors such as dehydration and temperature.[171] Conversely, in 2016 Farrugia *et al.* correlated the *in* *vivo* and *ex vivo* measurements conducted on rat liver, concluding that hydration and temperature are key parameters in ensuring that *ex vivo* data provides a true reflection of *in vivo* values.[166] Furthermore, Shahzad *et al.* reported liver measurements from BALB/c nude mice over a time period of 3.5 hours post-excision, noting the decrease in dielectric constant over time.[167] This again was concluded to be the result of dehydration, emphasising the need for careful timing and measurement protocols.

3.1.1 Outline

Given the variation of equipment, measurement techniques and timing protocols used in published reports, we were keen to establish an ‘in house’ set of controls for evaluation of the PSMA-coated zinc ferrite nanoparticles as contrast agents. This would allow them to be assessed for contrast relative to a biological background that has been measured under the same conditions. Having established the nanoparticle behaviour in solution, we first sought to use triple negative breast cancer cells (MDA-MB-231) as a model with methods based on the literature.[51,52]

Experiments then progressed to *ex vivo* models. In this study, we present the results of *ex-vivo* measurements of excised tissues from athymic nude mice using the open-ended co-axial probe technique. Measurements were taken between 500MHz and 4GHz on samples of liver, skin, muscle, and fat. Results were evaluated to examine the distinct profiles observed from individual tissues as well as any differences seen between individual animals. In characterising these tissues, we sought to provide a foundation for further work, with dielectric values specific to this model and measurement style. We also highlighted the known variability in contrast between tumour and surrounding tissues, and how this can vary between individuals. Additionally, we used excised tumours to establish if *ex vivo* intra-tumoral injection of PSMA-coated zinc ferrites had an impact on the dielectric profile.

Finally, *in vivo* dielectric profiling took place, again using an athymic nude mouse model with bilateral triple negative breast cancer tumours. This setup allowed for one tumour to be directly injected with PSMA-coated zinc ferrite nanoparticles while the other remained a control, with the dielectric profiles of both assessed.

3.2 Aim & Objectives

3.2.1 Aim

To establish *in vitro*, *ex vivo* and *in vivo* model systems for breast cancer using the open-ended co-axial probe technique.

3.2.2 Objectives

1) To explore triple negative breast cancer cells as an *in vitro* microwave imaging/sensing model.

2) To evaluate the *ex vivo* dielectric properties of tumours and tissues using the open-ended co-axial probe method.

3) *Ex vivo* characterization using the open-ended co-axial probe method of tumour dielectric properties with PSMA-coated zinc ferrite nanoparticles as contrast agents.

4) *In vivo* characterization using the co-axial probe method of tumour dielectric properties with PSMA-coated zinc ferrite nanoparticles contrast agents.

3.3 Results & Discussion

3.3.1 Dielectric properties of cells

As earlier discussed, MW imaging/sensing research requires the establishment of suitable living tissue model systems. Given variation in MW measurement practices, it is important to explore and establish living tissue model systems and baseline measurements consistently using the same setup. Having characterised synthesised PSMA-coated zinc ferrite nanoparticles in tumour phantoms, the next step was to begin application in living models. Initially, cells were explored using the triple-negative breast cancer cell line MDA-MB-231, with a view to explore an alternative to the often-complex tissue models.

From a setup perspective, all measurements were taken using a Keysight potable two-port VNA over a frequency range of 0.5-4 GHz. All measurement used a Keysight slim-form co-axial probe. Full details can be found in Materials and Methods. Basing the approach on available literature [52], cells in suspension were analysed using the open-ended co-axial probe technique using a slim-form probe. MDA-MB-231 were grown to a confluent state and resuspended in 5 mL of fresh DMEM media (minus supplementation). Initially, 6 concentrations of cell suspensions were explored (10^1-10^6 cells per mL), to examine whether changes in cell concentration were detectable (please see Appendices). Finding that this was not the case, a final concentration of 10^6 per mL (the highest initially tested) was decided for further experiments. A total of 10 consecutive measurements were taken in each cell suspension, and an average calculated.

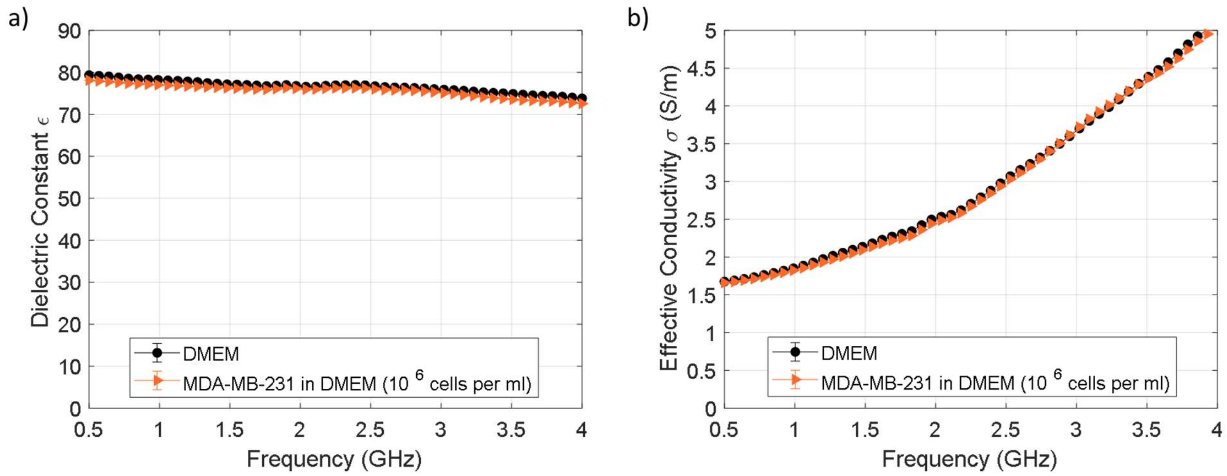

Figure 21 – Characterisation of MDA-MB-231 cells using the open-ended co-axial probe technique and a slim-form probe. Triple-negative breast cancer cell line MDA-MB-231 was suspended in 5 mL of DMEM at a concentration of 10^6 cells per mL. Graphs depict measured properties over a frequency range of 0.5-4 GHz and are shown in the panels as a) dielectric constant and b) effective conductivity. (n=3)

As can be seen from the above Figure 21, minimal difference is observed between concentrated cell suspension and the measurement of the background media control. This is the case for both measured dielectric constant and effective conductivity. This contrasts with a published paper by Ahmad et al. in 2019, which reported a difference between signatures of cancerous and healthy cell lines, as well as the ability to distinguish their signatures from background media.[52] However, an interesting publication using an osteosarcoma cell line reports similar findings to those we have observed.[172] The conclusions of this osteosarcoma study noted only small and inconsistent changes between cell suspensions and background media measured over a frequency range of 500 MHz to 18 GHz. The study also used a significantly higher number of cells in their suspension measurements when compared with our own, and yet still observed minimal change. This would indicate that even at higher concentrations, cells in suspension are difficult to profile using this technique and findings are therefore consistent with our measurement results. Overall, these varying observations in the literature could relate to measurement techniques used, or other factors such as cell line or cell preparation method.

Another parameter that was further investigated is the suspension medium of the cells. Mirroring the setup used for measurements in DMEM, alternative suspension mediums for the cells were explored. The impact of salts on the dielectric properties is well-established.[155,173] Therefore, it was important to assess alternatives with different salt concentrations to determine if the suspension medium was inhibiting our ability to correctly profile the cells. MDA-MB-231 were grown to a confluent state and resuspended in 5 mL of fresh Hank's Balanced Salt Solution (HBSS) and Phosphate Buffer Saline (PBS) to a final concentration of 10^6 per mL. A total of 10 consecutive measurements were taken in each cell suspension using the slim-form probe setup, and an average calculated.

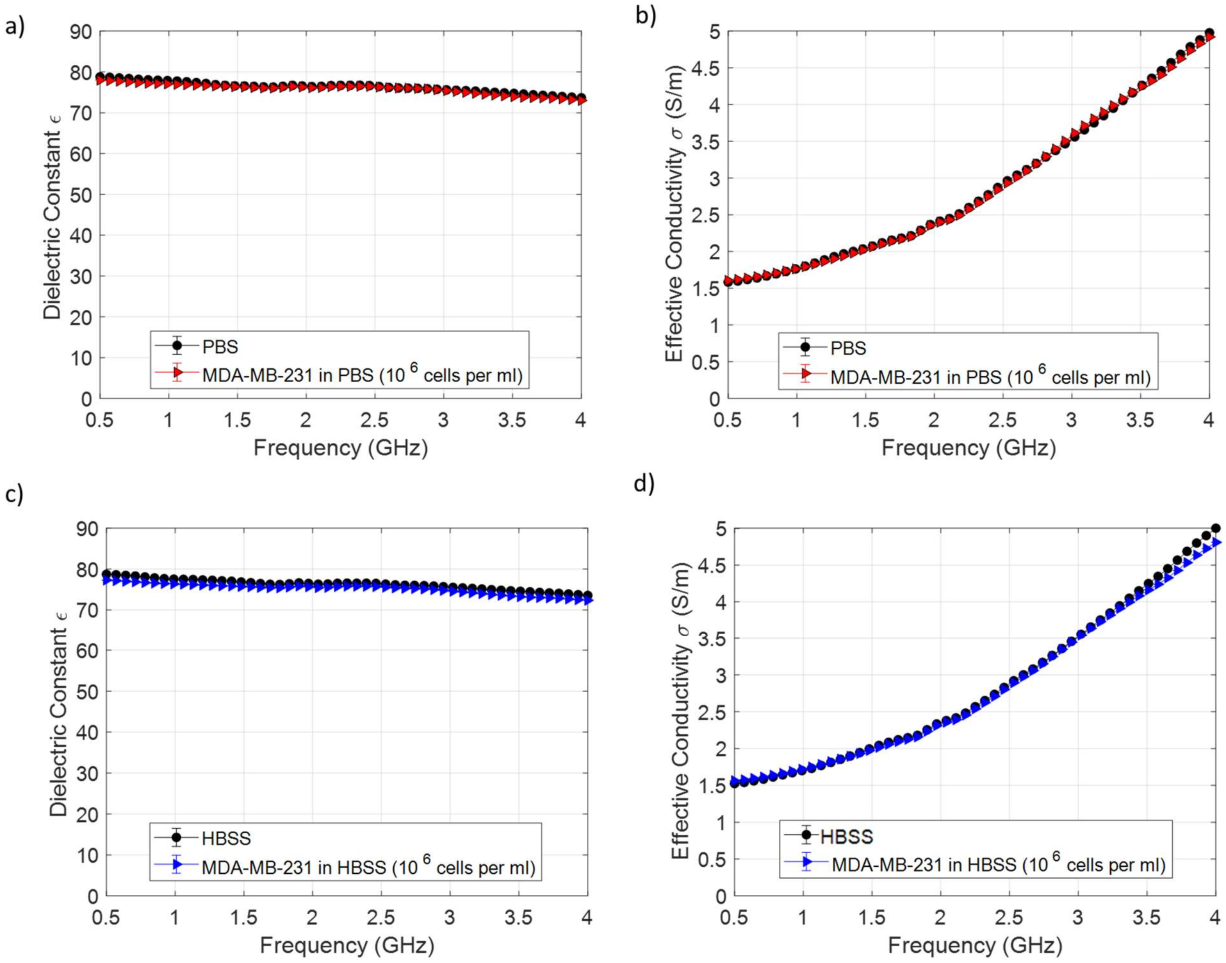

Figure 22 - Characterisation of cells using the open-ended co-axial probe technique and a slim-form probe. Triple-negative breast cancer cell line MDA-MB-231 was suspended in PBS or HBSS at a concentration of 10^6 cells per mL. Graphs depict measured properties over a frequency range of 0.5-4 GHz and are shown in the panels as: a) dielectric constant in PBS; b) effective conductivity in PBS; c) dielectric constant in HBSS; d) effective conductivity in HBSS. (n=3)

For both tested mediums (Figure 22), similar results were obtained, with again little observable difference between background and cells suspension. Additionally, it is noted that the profiles of all three mediums are remarkably similar. The results at 2.45 GHz have been collated for all suspension mediums in Figure 23. From this we can see further illustrated the minimal change observed between cell suspensions and the suspension mediums. The largest change seen is in the dielectric constant of cells in HBSS vs reference HBSS buffer, showing a shift from 75.7 to 76.5, an overall change of 0.8. However, given the small margins involved, this is within the expected error of the system and unlikely to represent a change bearing significance.

	Dielectric Constant ε at 2.45 GHz	**Effective Conductivity σ at 2.45 GHz (S/m)**
DMEM	76.7	2.9
MDA-MB-231 in DMEM (10^6 cells per mL)	76.8	2.9
PBS	76.6	2.9
MDA-MB-231 in PBS (10^6 cells per mL)	76.4	2.9
HBSS	76.5	2.8
MDA-MB-231 in HBSS (10^6 cells per mL)	75.7	2.8

Figure 23 – Table showing average measured dielectric constant ε and effective conductivity σ (S/m) values at 2.45 GHz for cell suspensions in varying mediums. (n=3)

Given that a similar signature is observed regardless of suspension medium, and the cells naturally begin to fall out of suspension and sediment to the bottom of any given container, it was decided to attempt measurement of the cells in a semi-solid format. This can be achieved by forming a cell pellet using centrifugation. The slim-form probe requires a minimum insertion into the desired sample of 5 mm with 5 mm around the tip area of the probe. Therefore, a cell pellet comprising approximately 60 million MDA-MB-231 cells was prepared using centrifugation. An appropriate diameter container was selected to accommodate the sample, to ensure sufficient depth for insertion of the probe. Care was taken to preserve the cell pellet, and residual media was removed, and the pellet washed with PBS. This method guaranteed the hydration of the pellet during the measurement and removed any residual media that may have an impact on the measurement.

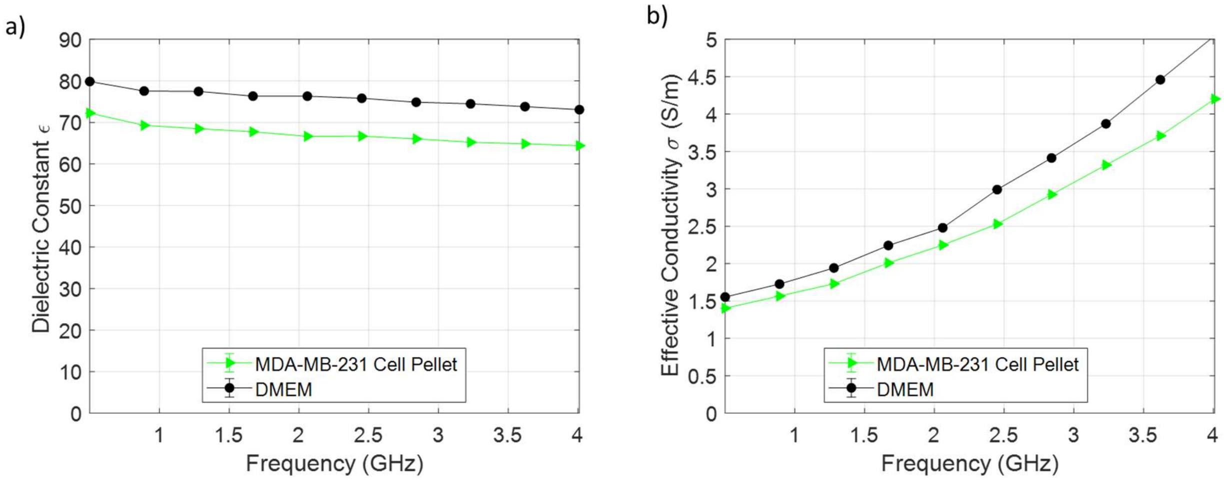

Figure 24 - Characterisation of a cell pellet using the open-ended co-axial probe technique and a slim-form probe. Triple-negative breast cancer cell line MDA-MB-231 was centrifuged to form a cell pellet. Graphs depict measured properties over a frequency range of 0.5-4 GHz and are shown in the panels as: a) dielectric constant and b) effective conductivity. Measured properties of DMEM are shown as a comparison. (n=3)

From Figure 24, it's clear an observed change is seen for both the dielectric constant and effective conductivity when comparing the measured cell pellet to background media samples. As triple-negative breast cancer cells have not been measured in this format previously, an appropriate literary comparison for cell pellet measurements was not able to be sourced for this. Interestingly, the values observed are not too distant from published tumour values and phantom model systems with a dielectric constant measured at 66.7 at 2.45 GHz and an effective conductivity of 2.5 S/m at this same frequency. To give an example from the literature, measured dielectric constant and effective conductivity values of breast tumour tissue at 2.45 GHz have been reported as in the region of 60 and 2.5 S/m respectively.[139] This is an unusual observation, given that pelleted cells lack the structure of tumour tissue and vasculature of any nature, but perhaps this structure is closer to tumour configuration than suspended cells, yet maintains its hydration.

Our final consideration is the cell-line behaviour. MDA-MB-231 are an adherent cell line, preferring to be in a monolayer configuration. While every care was taken to take prompt measurements of the cells following detachment, cells may exhibit stress in suspension and ultimately cell death could occur. To mitigate this, an alternative measurement adapted from the literature was explored.[51] This technique instead of a slim-form probe utilises a flat probe, with a wider, circular surface area. Therefore, rather than measuring as a suspension, this experiment sought to assess MDA-MB-231 cells grown in a monolayer while still adhered to a tissue culture plate, limiting stresses to the cells.

These experiments used a SPEAG DAK 1.2E open-ended co-axial probe suitable for use over a frequency range of 5 GHz - 67 GHz. This is similar to the probe described in the aforementioned literature but has a slightly different operational frequency range and a diameter of 18 mm. The probe was used in conjunction with a 2-port Keysight VNA, and the system was calibrated prior to measurements. Initial experiments a seeding density of 500,000 cells was used (please see Appendices), with no detectable difference observed relative to media-only control wells. For further experiments, 1 million MDA-MB-231 cells were seeded in 6-well and 12-well tissue culture plates and allowed to adhere for a period of 24 hours. Following incubation, cells were washed 3x with PBS and an appropriate amount of DMEM readded to each well. Experiments were performed in triplicate, and a total of 10 measurements were taken per well and an average calculated.

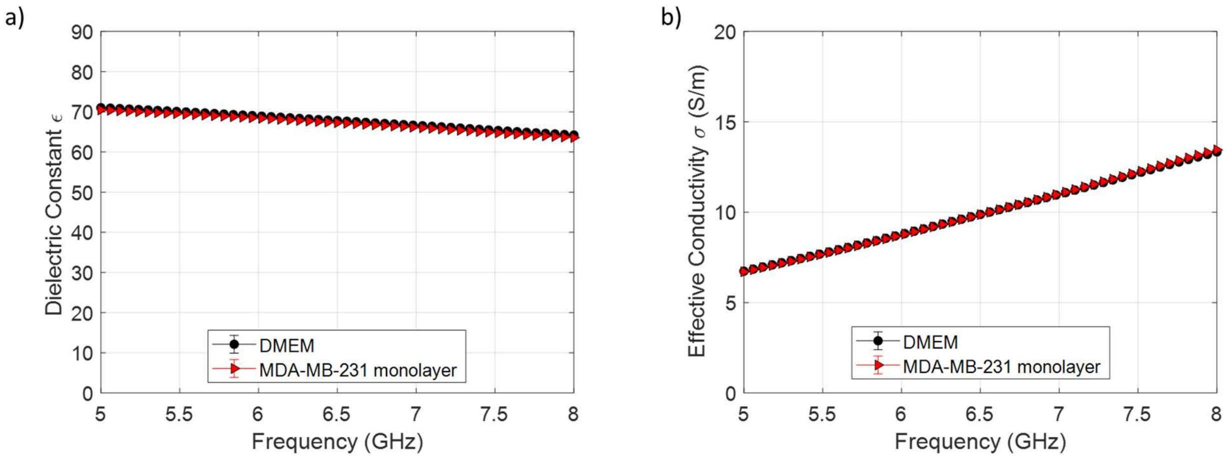

Figure 25 – Characterisation of cell monolayer using the DAK 1.2E probe. Triple-negative breast cancer cell line MDA-MB-231 allowed to form a monolayer on a 6-well plate. Graphs depict measured properties over a frequency range of 5-8 GHz and are shown in the panels as: a) dielectric constant and b) effective conductivity. Measured properties of DMEM are shown as a comparison. (n=3)

Figure 25 shows the measured properties of the MDA-MB-231 cell monolayer measured using the DAK 1.3E probe. As with suspension measurements minimal difference is observed between cell and background media measurements. As an illustration, dielectric constant values at 6 GHz were measured to be 68.9 for DMEM and 68.4 for the cell monolayer. Likewise, effective conductivity is measured to be 8.8 S/m for both at 6 GHz. It is of course important to highlight that these measurements were taken over a different frequency range than those in suspension due to the operational frequency of the probe, however it is interesting that the trend is the same.

Having considered that the surface area may be presenting an issue, measurements were taken under the same conditions, but using 12-well plates, again seeded with 1 million MDA-MB-231 cells. This is more similar to the setup of Hussein et al. as their design also uses a 12-well plate, however the number of cells seeded is more than double the amount reported in the paper.

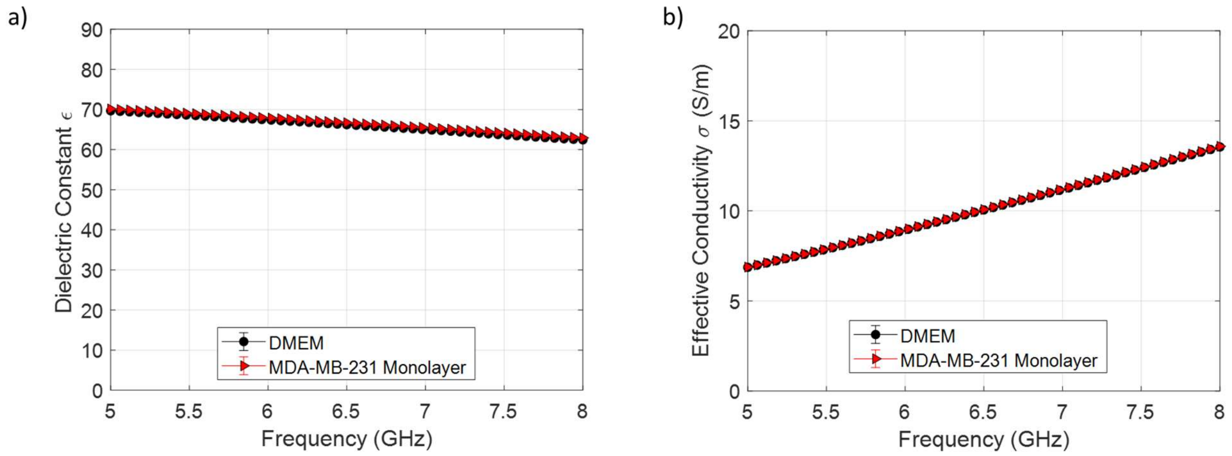

Figure 26 - Characterisation of cell monolayer using DAK 1.2E probe. Triple-negative breast cancer cell line MDA-MB-231 allowed to form a monolayer on a 12-well plate. Graphs depict measured properties over a frequency range of 5-8 GHz and are shown in the panels as: a) dielectric constant and b) effective conductivity. Measured properties of DMEM are shown as a comparison. (n=3)

Figure 26 shows the measured properties of the MDA-MB-231 cell monolayer measured using the DAK 1.3E probe in a 12-well plate. As with the 6-well plate measurements, little difference is observed between cell and background media measurements, though a similar trend between the two plate types was noted. Dielectric constant values at 6 GHz were measured to be 67.4 for DMEM and 67.9 for the cell monolayer. Similarly, effective conductivity is measured to be 9 S/m for both at 6 GHz.

When comparing these values to those published by Hussein et al., the measured dielectric constant of the MDA-MB-231 appears to be similar, with an approximate value of 64 at 6 GHz, slightly less than observed in our experiments. Measured conductivity values follow a similar trend, with the study reportingly approximately 7.5 S/m compared to our values of 8.8 S/m and 9 S/m. This small difference in conductivity may be accounted for by the slight difference in experimental setup, such as the probe, or lab to lab variation. In the published paper, the authors reportedly remove the media from the wells and obtain further measurements with lesser different values. This was not undertaken for our study, as a review of the operating parameters of the probe indicated this would not be suitable. A media control is not provided by the authors, and so it is not possible to compare this. Overall, measurements taken using this setup showed no indication of a difference between values obtained in the absence or presence of cells.

In conclusion, despite exploring different measurement approaches, a lack of consistent difference between measured cells and the background made this an unsuitable model for further investigation. While cell pellet measurements showed an observable difference, the need to pellet and wash cells would create challenges if used in conjunction with nanoparticles. Therefore, characterisation of the PSMA-coated zinc ferrites as MW contrast agents continued in *ex vivo* tissues.

3.3.2 Ex vivo *dielectric properties of tissues*

Before advancing to tumour measurements and exploring contrast agents, it was important to establish that our MW setup could produce replicable measurements in tissues. Tissues excised from an athymic nude mouse model were assessed for their dielectric properties, in keeping with the desired strain for later tumour model studies. Tumours were induced using MDA-MB-231 triple-negative breast cancer cells and allowed to grow an approximate size of 5-6 mm Ø. At this size, animals were humanely culled, and tissues excised for measurements. These measurements comprised the same setup as earlier described, using a slim-form open-ended co-axial probe in combination with a Keysight two-port VNA system. Measurements were conducted in under 5 minutes post-excision, to avoid dehydration. The number of samples for each tissue type is carefully noted with each graph. This varies in places as care was taken only to measure intact and undamaged samples. The measured dielectric properties of liver, leg muscle, skin, and abdominal fat are illustrated, with dielectric constant displayed on the *y*-axis over a scale of 0-90, and frequency (GHz) on the *x*-axis over a range of 0.5-4 GHz. Effective conductivity is presented over the same frequency range plotted between 0 and 5 S/m. Each coloured line represents a distinct sample from an individual mouse, with the plot representing the average of the 10 consecutive surface measurements using the co-axial probe technique. Each dielectric constant plot contains a zoomed portion over a frequency range of 1-1.5 GHz for comparison of the measured properties between samples.

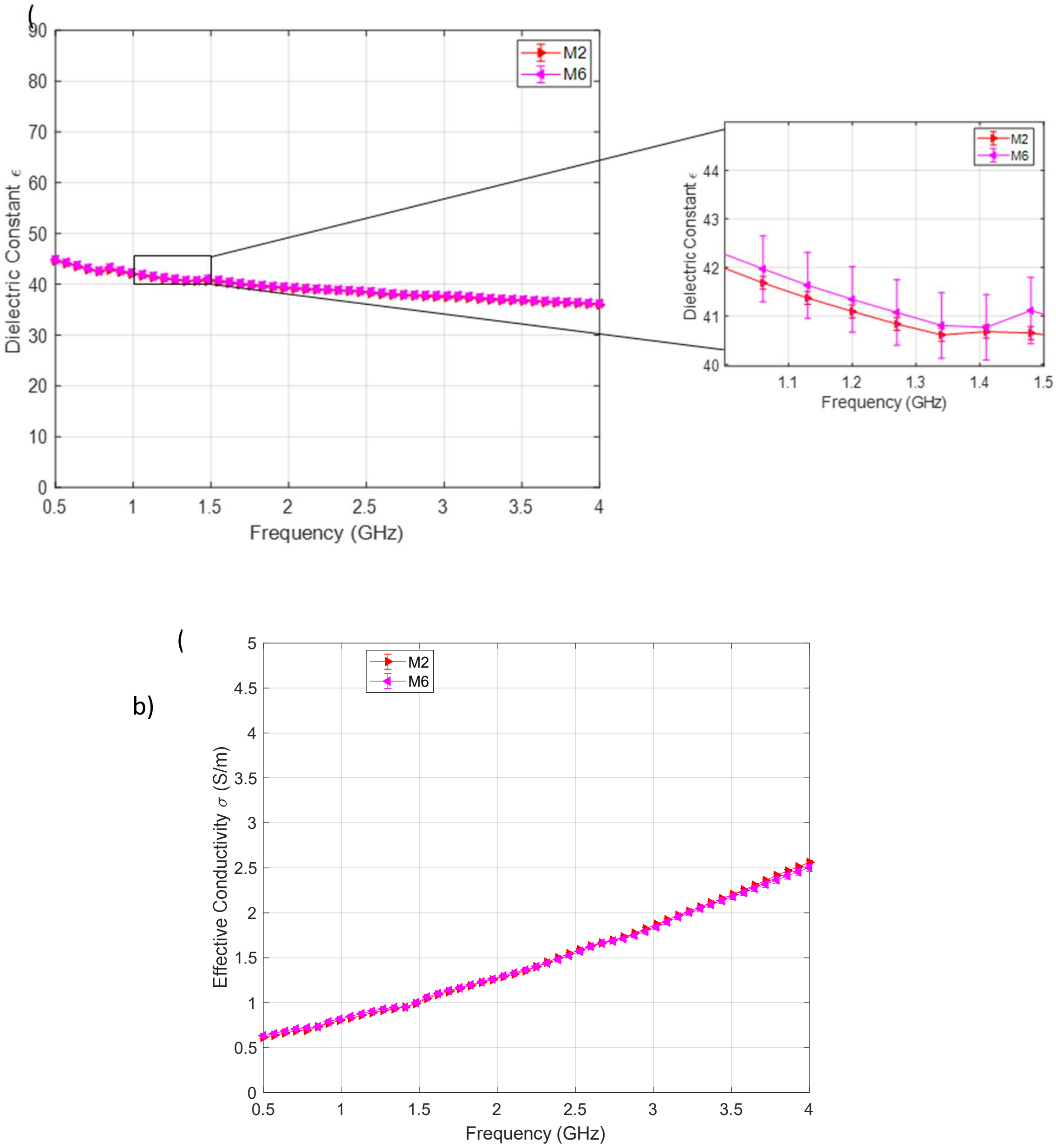

Figure 27 - Measured dielectric properties of two individual liver samples across a 0.5–4 GHz frequency range: (a) dielectric constant, (b) effective conductivity (S/m). (n=2)

The measured dielectric properties of the excised liver are shown in

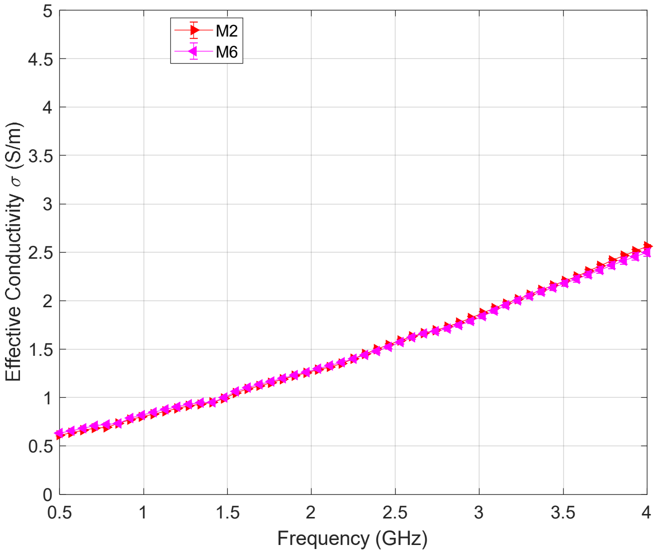

Figure 27. As can be seen, there is minimal variation between the two individual samples measured, with both samples showing an average dielectric constant of approximately 42 at 1 GHz. These values are higher than those measured for fat and skin which can be attributed to both the strong blood supply and fluid content of the liver. These values are similar to those reported in previous literature on the dielectric properties of the liver. [164,166,174]

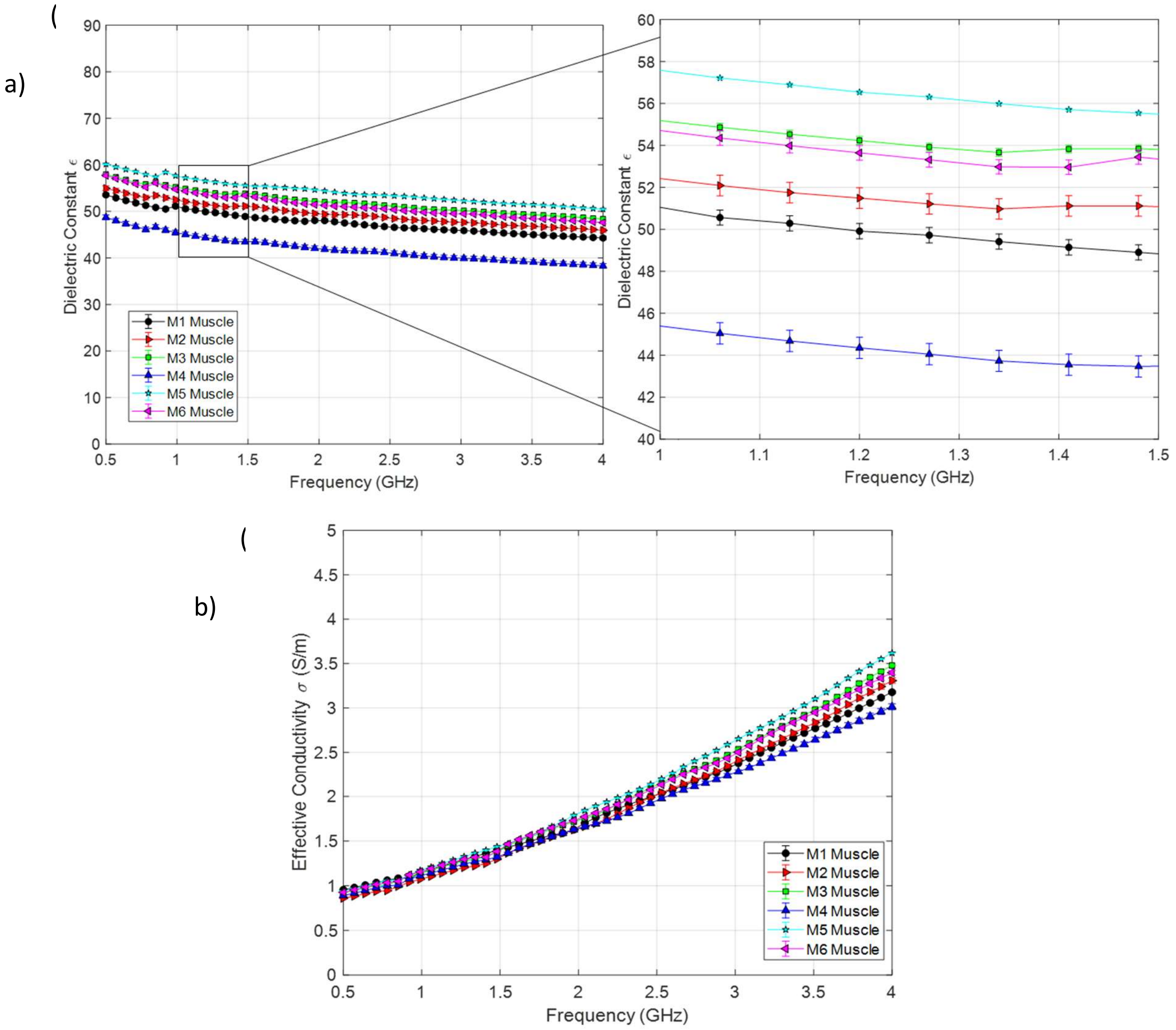

Figure 28 - Measured dielectric properties of six individual leg muscle samples across a 0.5–4 GHz frequency range: (a) dielectric constant, (b) effective conductivity (S/m). (n=6)

Muscle is a highly vasuclar tissue, as is demonstrated in Figure 28. Here we can see the 6 individual samples show dielectric constant over a range of 45-58 at 1 GHz, which is the largest variation we observed over any of the measured tissues. Muscle tissue is known to be highly heterogenous, which may account for this variability. This observed profile however, is in line with an *in vivo* study conducted by Cho *et al.* in 2006 [174] which the relative permitivity of skeletal muscle in athmyic nude mice was measured using a planar-tip probe, giving an average of 48.5. Both liver and musle measurements showed increasing conductivity over the frequency range. This is in contrast to skin and fat measurements, which while demonstrating an increase, was observed to be much smaller.

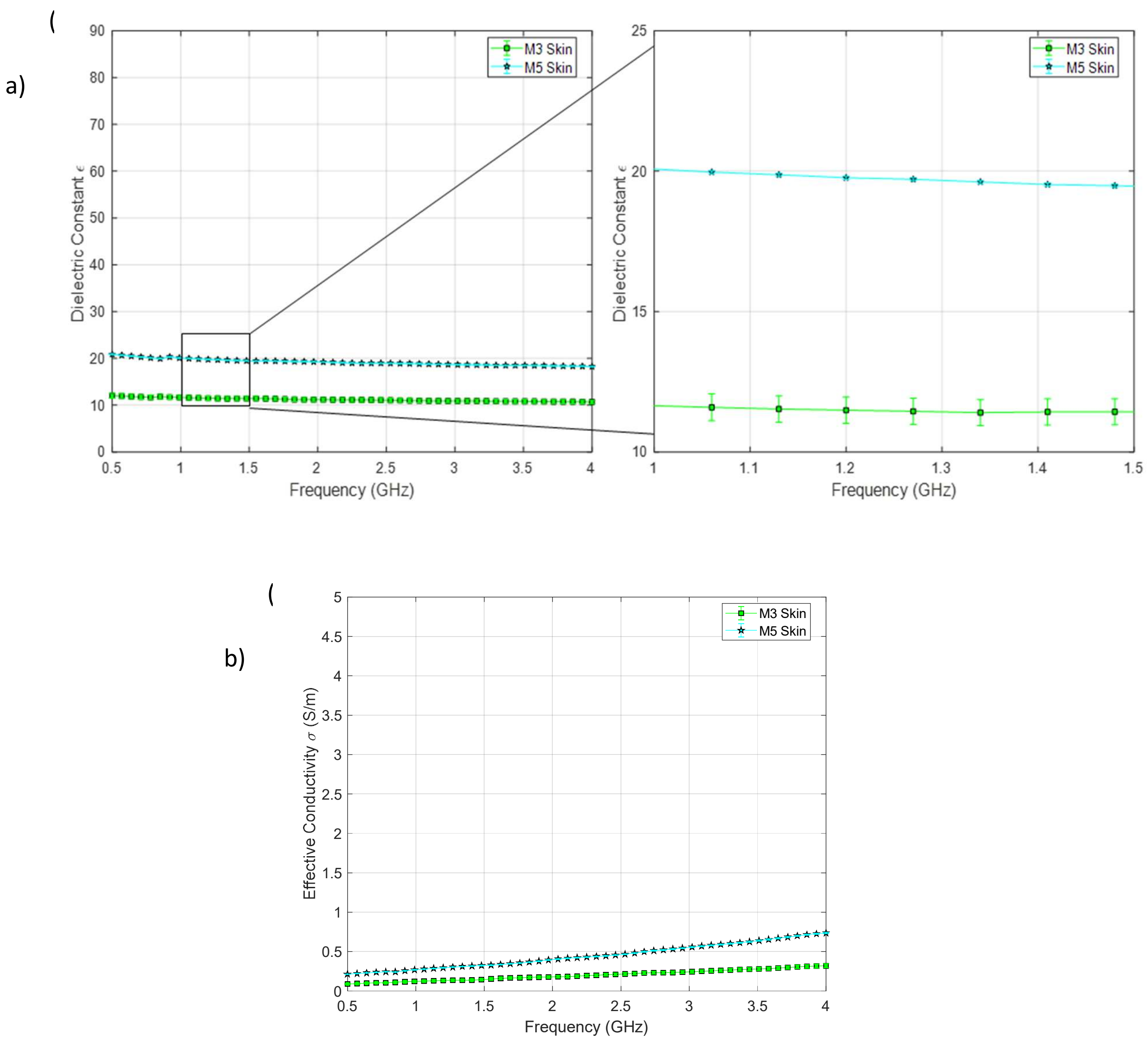

Figure 29 - Measured dielectric properties of two individual skin samples across a 0.5–4 GHz frequency range: (a) dielectric constant, (b) effective conductivity (S/m). (n=2)

Excised skin samples presented more of a challenge to excise and measure, particularly due to the thickness of the samples. This again may account for some of the variation observed in Figure 29, with a dielectric constant ranging from 11-20 at 1 GHz. Nevertheless, these values are low compared with muscle and liver samples, which is to be expected given the lesser blood supply and water content.

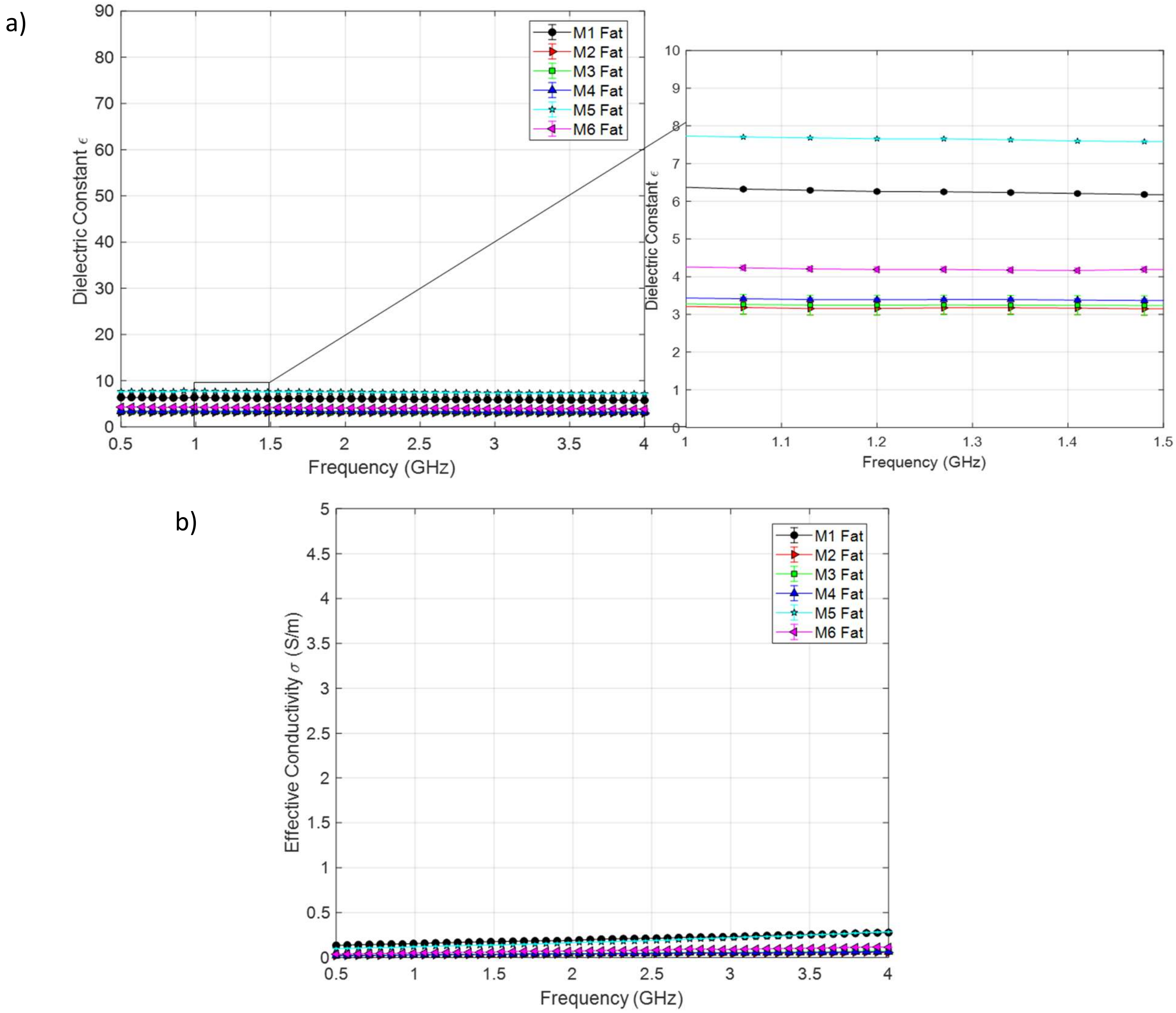

Figure 30 - Measured dielectric properties of six individual abdominal fat samples across a 0.5–4 GHz frequency range: (a) dielectric constant, (b) effective conductivity (S/m). (n=6)

Six fat samples from the abdomen were measured as illustrated in Figure 30. This data set showed lower variability than that of the more vascular tissues, with a measured dielectric constant of between 3 and 8 at 1GHz.

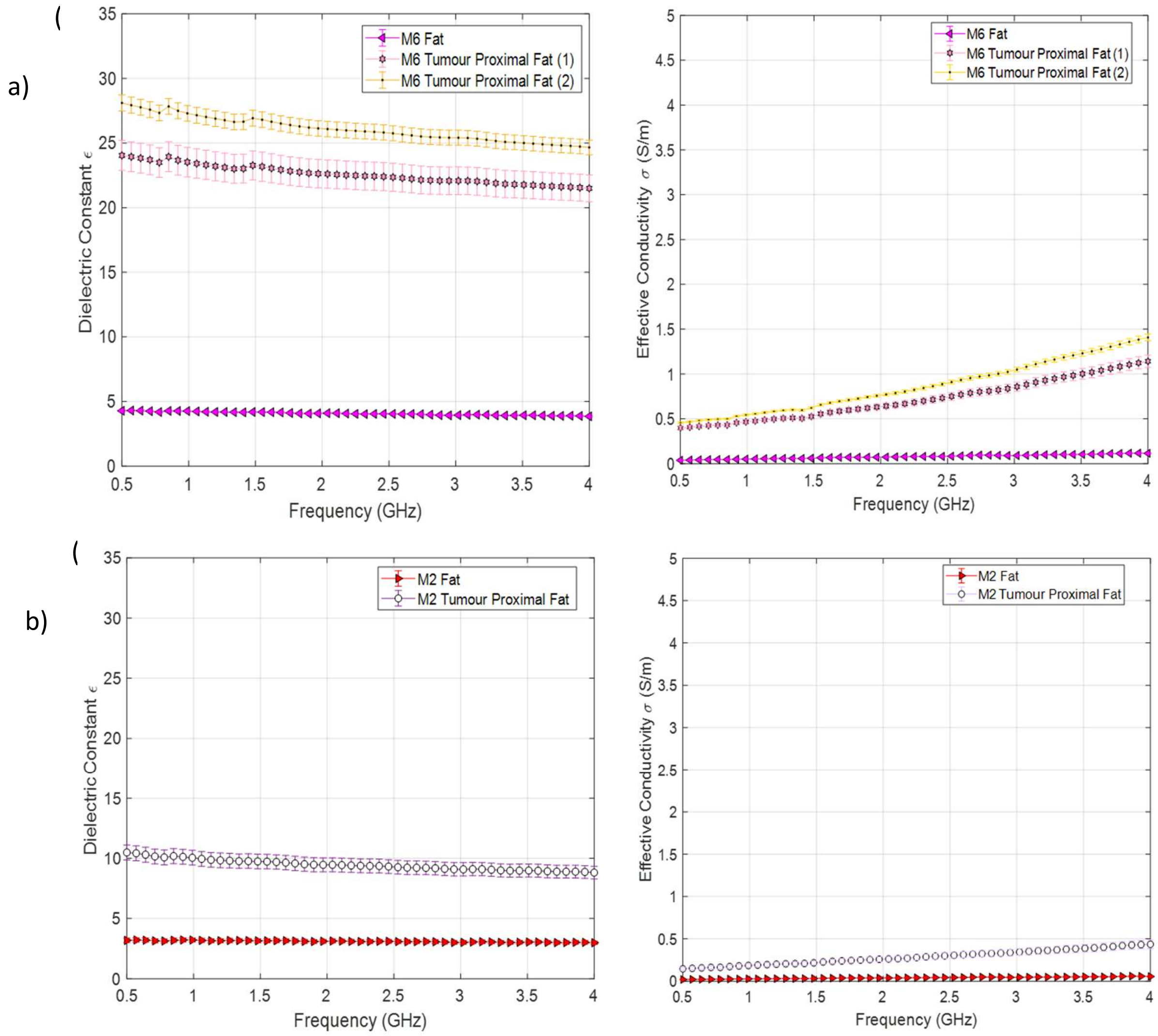

Figure 31 - Measured dielectric properties of fat and tumour proximal fat from two individual mice across a 0.5–4 GHz frequency range. Panels a) and b) represent the measurements taken from each individual. (n=2)

Figure 31 illustrates four plots comparing excised abominal fat with fat excised in close proximity to the tumour. Dielectric constant is displayed on the y-axis over a scale of 0-35, and frequency (GHz) is on the x-axis over a range of 0.5-4GHz. Graphs presenting the conductivity values have a y-axis scale of 0 to 5 S/m. It should be noted that the tumour proximal fat sample size is small, with a total of 3 samples from 2 individual animals and was collected based on the availability of suitable deposits near the tumour site. For both animals, we can see an increase in the measured dielectric constant for the tumour proximal fat, when compared with the abdominal fat. The observed effect is particularly prominent in plot (a), where both tumour proximal fat samples show a large dielectric constant increase. In plot (b), the effect is less pronounced, but nonetheless observed, rising from an average of 3.2 to 10 at 1 GHz. The increase could be due to increased tumour vasculature, which is typically abnormal, having an impact on the surrounding tissue. The difference is also observed in conductivity values, with increases in measurements taken from tumour proximal fat.

Comparing the dielectric constant values highlights the variance in normal tissue’s dielectric properties near cancerous tissue, even with tumours of the same origin and in a similar location. This has long been a key issue in microwave imaging/sensing, where tumour identification is based on the contrast between the cancerous and surrounding tissues and reinforces the potential of contrast enhancers or even reference tissues within an individual to circumvent this challenge.

3.3.3 Ex vivo dielectric properties of tumours

While significant data has been collected on the dielectric properties of tumours in the literature, differences in measurement approaches make it essential to verify control data for specific setups and models. In these experiments, an athymic nude mouse model bearing single flank triple-negative breast cancer tumours was used. Tumours were induced using MDA-MB-231 triple-negative breast cancer cells and allowed to grow an approximate size of 5-6 mm Ø. At this size, animals were humanely culled, and tumours excised for measurements. The measurements used the slim-form open-ended co-axial probe and a Keysight two-port VNA system. To avoid dehydration, measurements were conducted in under 5 minutes post-excision, with 10 consecutive measurements taken in the same position for each sample. Three different types of measurements for each tumour were taken: tumour in-situ (skin intact), tumour post-excision (skin removed) and tumour core. The expectation was to observe 3 distinct profiles, as the skin barrier is known to alter the dielectric measurement of tissues. The dielectric constant and effective conductivity (S/m) of each sample were measured over a range of 0.5-4 GHz. Presented is the averaged data from measurements taken across 5 athymic nude mice.

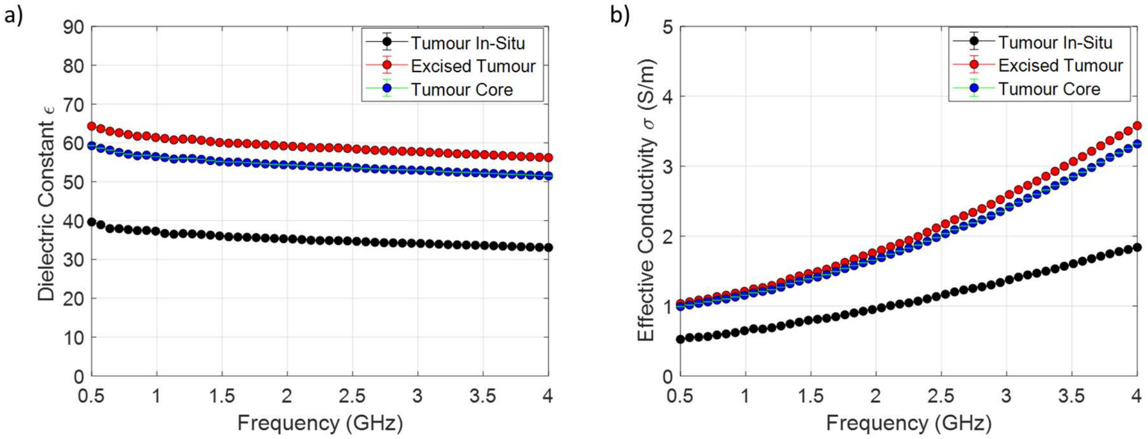

Figure 32 – Graph showing *ex* vivo measured a) dielectric constant (ε) and b) effective conductivity S/m (σ) of triple-negative breast cancer tumours in an athymic nude mouse model. For each individual mouse, 10 consecutive measurements were taken using a slim-form co-axial probe in the same position. Plots show measurements in three different conditions: tumour in-situ (n=5); excised tumour (n=5) and tumour core (n=4).

The graphs in Figure 32 show the distinct profiles observed for the different measured areas of tumour. Particularly notable, is the dielectric constant tumour in-situ profile, which shows a significantly lower dielectric constant and effective conductivity than the other two profiles. This is hypothesised to be due to the impact of skin on dielectric tissue measurements. This measurement was taken before excision and so the skin remained intact covering the surface of the tumour. In the previous section, we measured excised skin, noting the dielectric constant to be less than 20 at 2.45 GHz for both measured samples. Comparatively, we see here an average dielectric constant of 34.8 at 2.45 GHz (Figure 33), which may indicate the tumour beneath the skin surface is influencing the measured value. When we compare the in-situ with excised values, the contrast is stark, with an average dielectric constant of 58.5 at 2.45 GHz. This again highlights the impact of the skin layer on measured properties and is consistent with an area of high blood supply. Tumours undergo abnormal angiogenesis to supply the tumour during growth, creating leaking blood vessels of abnormal morphology. This process means the tumour is likely to have a high blood content, in keeping with the measured values. The core of the tumour also demonstrates a shift when compared to excised tumour surface, albeit less pronounced than that of the tumour in-situ. Taking into consideration the standard deviation, this puts the value close to the measured excised tumour range, though a performed t-test gave $p<0.05$ indicating the groups are significantly different. Many tumours when grown to a large size exhibit necrosis at the core, disrupting blood supply to the area, which could account for the slightly lesser values observed for core measurements. Naturally, similar trends are observed in conductivity values for the three conditions, with average values at 2.45 GHz of 2.2 S/m, 1.1 S/m and 2.0 S/m for excised tumour, tumour in-situ and tumour core respectively. A full breakdown of measured values at 2.45 GHz can be found in Figure 33.

	Dielectric Constant ε Excised Tumour	Effective Conductivity σ (S/m) Excised Tumour	Dielectric Constant ε Tumour In-Situ	Effective Conductivity σ (S/m) Tumour In-Situ	Dielectric Constant ε Tumour Core	Effective Conductivity σ (S/m) Tumour Core
Mouse 1	56.7	2.1	32.7	1.0	51.9	1.9
Mouse 2	59.2	2.2	30.8	0.9	58.9	2.2
Mouse 3	57.5	2.1	32.4	1.0	52.9	2.0
Mouse 4	58.0	2.1	37.9	1.3	*	
Mouse 5	61.1	2.3	40.2	1.4	50.7	1.9
Average	**58.5**	**2.2**	**34.8**	**1.1**	**53.6**	**2.0**
Standard Deviation	**1.7**	**0.1**	**4.0**	**0.2**	**3.6**	**0.1**

Figure 33 - Table showing *ex* vivo measured dielectric constant (ε) and effective conductivity (σ) (S/m) of triple-negative breast cancer tumours in an athymic nude mouse model at 2.45 GHz. For each individual mouse, 10 consecutive measurements were taken using a slim-form co-axial probe in the same position. Table show measurements in three different conditions: tumour in-situ (n=5); excised tumour (n=5) and tumour core (n=4).

**Tumour was small, and a reliable core measurement was not possible.*

Comparing these values to available literature such as Cho et al.[164,166,174], we can see measurement profiles taken closely resemble those of the excised tumour. This study has a slightly different measurement technique, using an invasive planar probe to measure the tumours, which negates the impact of the skin barrier. This is therefore most closely matched with the excised tumour measurements we have taken and given that the study uses the same mouse strain and cell line it is reassuring to see resemblance in the profiles. Translating these data out of the model system, measured dielectric constant and conductivity values from cancer surgery excisions have shown values at 2.45 GHz of approximately 60 and 2.5 respectively.[140] That our model system measurements show values in this range is further confirmation of the viability of the model.

Overall, this study demonstrates the capability of the slim-form open-ended co-axial probe method to produce consistent measurements between individuals and of the athymic nude mouse breast model to give values comparable to those in published studies for both other model types and patient samples. It also highlights the significance of tumour region in the values obtained, notably the tumour core and reinforces known challenges associated with the skin barrier. Finally, these data provide a baseline for further *ex vivo* testing with incorporation of candidate MW imaging/sensing contrast agents.

3.3.4 Ex vivo *dielectric properties of tumours with PSMA-coated zinc ferrite contrast nanoparticles*

The measured *ex vivo* data of tumours and tissues provided a solid foundation for further experiments with the nude mouse model. The Keysight two-port system in combination with the slim-form open-ended co-axial probe had demonstrated replicable results, forming a clear picture of the background properties of the tissues in this model. The next step, therefore, was to use synthesised PSMA-coated zinc ferrite nanoparticles in excised tissues to determine if an observable contrast was present.

PSMA-coated zinc ferrite nanoparticles were synthesised using the thermal decomposition method. To ensure dispersion in water and bioavailability, particles were coated using a polymer PSMA (Poly (styrene- co -maleic anhydride). For full synthesis details please see Materials and Methods. The base particle and coating were selected based on experiments conducted in Chapter 2. Particle size was determined by DLS, and metal content by ICP-OES; uncoated particles were also characterised by TEM imaging. Results are displayed in Figure 34.

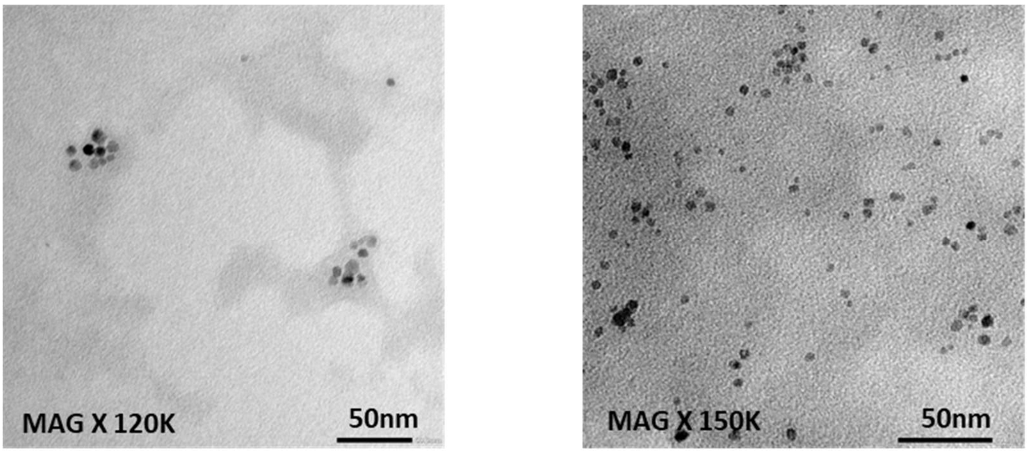

Formulation	z-average size /nm	PDI
[PSMA]-$Zn_{0.06}Fe_2O_4$	117.8 (+/- 1.2)	0.20 (+/- 0.02)

Figure 34 - Characteristics of synthesised $Zn_{0.06}Fe_2O_4$ nanoparticles used for *in vivo* experiments. Panels show TEM images of the uncoated particles taken at X100K and X200K. The table shows the measured z-average and PDI by DLS of PSMA-coated particles. Values shown are the calculated average of 3 individual DLS measurements +/- SD.

Bilateral triple-negative breast cancer tumours were induced in athymic nude mice using MDA-MB-231 cells and allowed to grow to a size of 5-6 mm Ø over a period of approximately 2 weeks. At this time, initial measurements of the tumours were taken *in vivo* before the humane culling of the animals. Graphs demonstrate the average of 10 tumours measured on 5 individual mice. 10 consecutive measurements were taken of each tumour, maintaining the same position with the co-axial probe. As these measurements are *in vivo* the skin is intact.

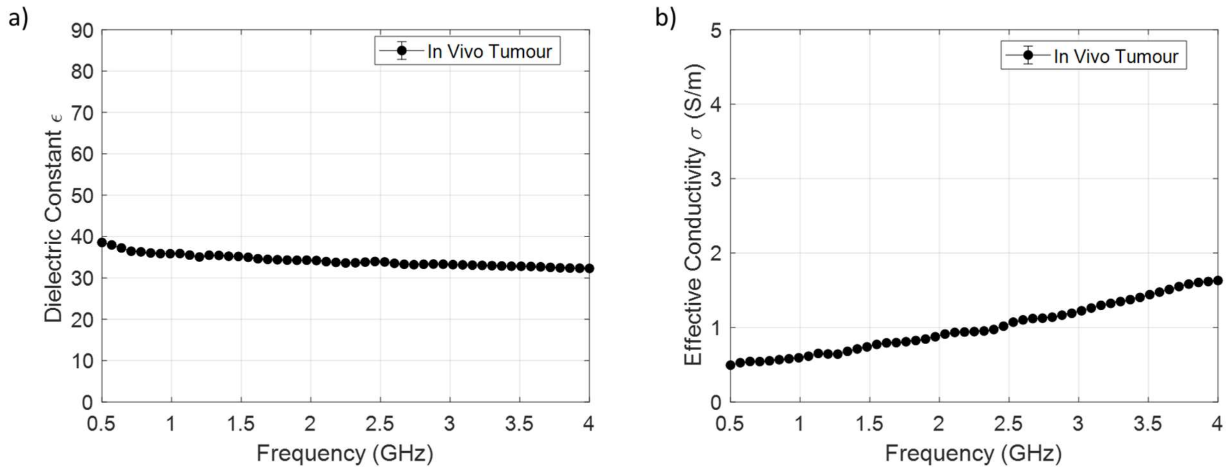

Figure 35 - Graph showing *in vivo* measured a) dielectric constant (ε) and b) effective conductivity S/m (σ) of triple-negative breast cancer tumours in an athymic nude mouse model. For each individual tumour, 10 consecutive measurements were taken using a slim-form co-axial probe in the same position. Plots show an average calculated from measurements of 10 individual tumours. (n=5)

The effective conductivity at 2.45 GHz is measured to be 1.0 S/m; the dielectric constant at the same frequency is 34.0, which when compared to the *ex vivo* 'tumour in-situ' measurements taken in the previous experiments demonstrates a similar trend. The average dielectric constant measured was 34.8 and effective conductivity was 1.1 S/m. These data give further confirmation of the reproducibility of this measurement style and consistency seen across this breast cancer model.

Following the humane culling of the mice, tumours were excised and directly injected with PSMA-coated zinc ferrite nanoparticles (0.06 mg/mL; 10 µl) or control diH_2O. Tumours were subsequently measured using the previously described setup, with 10 consecutive measurements taken in the same position and an average calculated. Tumours were measured in under 5 minutes post-excision to prevent dehydration. The following graphs show the average measurements of excised tumours injected with PSMA-coated zinc ferrite nanoparticles (0.06 mg/mL; 10 µl) and excised tumours injected with 10 µl of diH_2O.

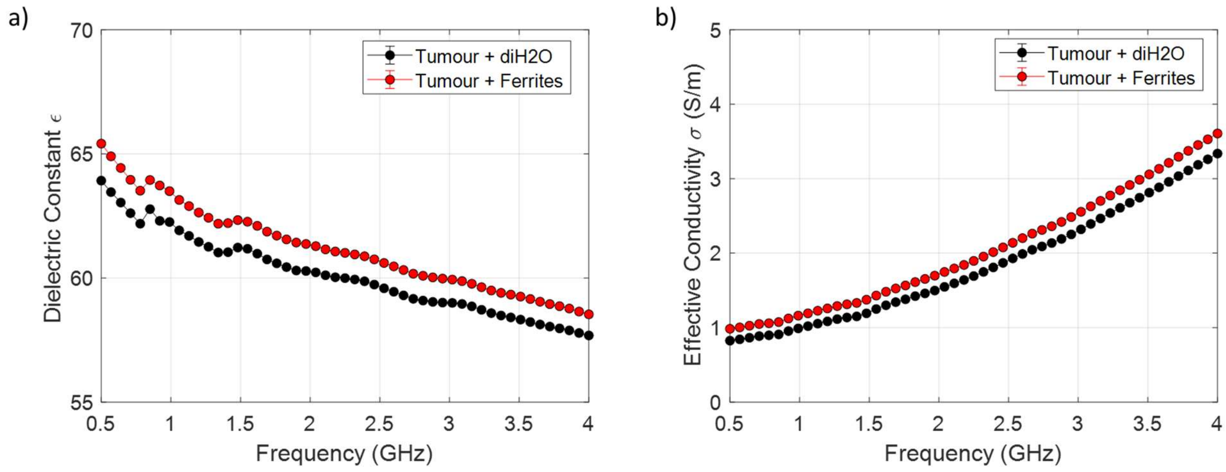

Figure 36 - Graph showing measured a) dielectric constant (ε) and b) effective conductivity (σ) of *ex vivo* triple-negative breast cancer tumours in an athymic nude mouse model injected with zinc PSMA-coated zinc ferrite nanoparticles (0.06 mg/mL; 10 µl) or de-ionised water (10 µl). For each individual tumour, 10 consecutive measurements were taken using a slim-form co-axial probe in the same position. Plots show an average calculated from measurements of 5 individual tumours per group. (n=5)

As can be seen from Figure 36, a small change is observed in dielectric constant when comparing the injected PSMA-coated zinc ferrite nanoparticles vs the water control. Average dielectric constant at 2.45 GHz is measured at 60.7 for excised tumour with injected PSMA-coated zinc ferrites, and 59.7 for excised tumour injected with water. Owing to the risk of dehydration, it was not possible to measure the individual tumours before injection and after injection. However, we can draw some comparison from previous *ex vivo* tumour experiments, where the dielectric constant of excised tumour was 58.6. For the tumours injected with water therefore we are seeing a shift of approximately 1, and for tumours injected with PSMA-coated zinc ferrites, this is approximately 2. Similar trends were observed for effective conductivity, which at 2.45 GHz was recorded to be 2.1 S/m and 1.9 S/m for tumours injected with PSMA-coated ferrites and water respectively. This is compared with the value of 2.2 S/m measured in the previous *ex* vivo experiments. There are limitations with this type of experiment however, such as the lack of blood flow, making the tumours more difficult to inject into. In conclusion, while a small change can be seen, *in vivo* experiments would be better suited to determining the true values. The PSMA-coated zinc ferrites are also in a low concentration and low injection volume. Further experiments may benefit from increasing the concentration injected.

3.3.5 In vivo *dielectric properties of tumours with ferrite contrast nanoparticles*

Having assessed *ex vivo* properties and observed the small changes in dielectric properties in an *ex vivo* environment, it was important to determine the characteristics of the PSMA-coated zinc ferrite nanoparticles *in vivo*. As these particles had not previously been tested *in vivo*, a small study group of 3 animals was selected to demonstrate proof of concept and safety.

PSMA-coated zinc ferrite nanoparticles prepared for these experiments were the same batch as previously used in the *ex vivo* studies. Characteristics, therefore, are the same as those described in the preceding section. A small alteration made however was the injected concentration, which for *in vivo* experiments was increased to 0.2 mg/mL by concentrating particles by spin filtration. Dual flank tumours were induced in an athymic nude mouse model using the triple-negative breast cancer cell line MDA-MB-231. Tumours were allowed to grow to approximately 5-6 mm Ø. Properties of the tumours were measured as a baseline using the Keysight two-port VNA system and slim-form probe. The skin was not removed for these measurements. For each tumour, a series of 5 measurements was taken with the co-axial probe in the same position and an average later calculated. This is less than the number of measurements taken *ex vivo* as consideration had to be given to the animal and length of anaesthesia. Following this, PSMA-coated zinc ferrites suspended in diH_2O (0.2 mg/mL; 10 µl) were injected intra-tumourally, and immediate further measurements taken using the same setup and protocol. After periods of 1h, 2h and 4h, further dielectric measurements were taken, to determine the longevity of any observed contrast. Data graphically presented in Figure 37 shows the dielectric constant and effective conductivity measurements taken from a group of 3 mice pre- and post- ferrite injection.

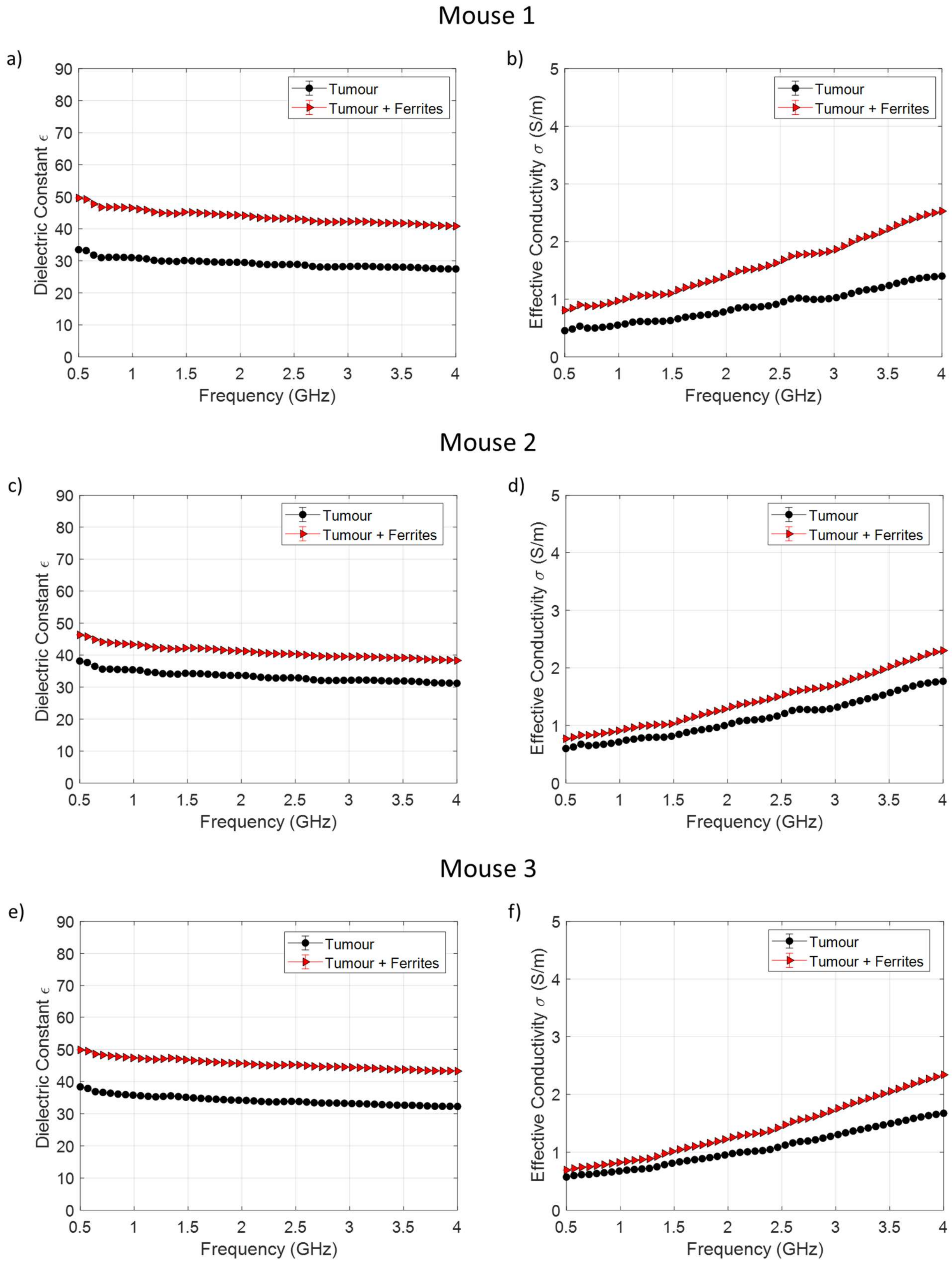

Figure 37 - Graph showing measured dielectric constant (ε) and effective conductivity S/m (σ) of triple-negative breast cancer tumours in an athymic nude mouse model. For each individual mouse,

5 consecutive measurements were taken using a slim-form co-axial probe in the same position. Plots shown are in both the absence and presence of injected ferrite nanoparticles (0.2 mg/mL; 10 µl) over a frequency range of 0.5-4 GHz.

From the graphs shown in Figure 37, a significant difference is noted for all three tumours following injection of PSMA-coated zinc ferrites (0.2 mg/mL; 10 µl). From a practical perspective, *in vivo* tumours are considerably easier to inject, and have a blood flow allowing the dispersion of the agent into the tumour region. It's key also to note that these measurements are taken through the skin barrier, and still a notable change is observed. Figure 38 shows the breakdown of dielectric constant and effective conductivity measurements for each individual mouse, as well as a calculated average and standard deviation.

	Dielectric Constant ε of tumour at 2.45 GHz	**Dielectric Constant ε of tumour + ferrites at 2.45 GHz**	**Change in Dielectric Constant ε at 2.45 GHz**	**Effective Conductivity σ (S/m) of tumour at 2.45 GHz**	**Effective Conductivity σ (S/m) of tumour + ferrites at 2.45 GHz**	**Change in Effective Conductivity σ (S/m) at 2.45 GHz**
Mouse 1	28.9	43.2	14.3	0.9	1.6	0.7
Mouse 2	32.9	40.4	7.5	1.2	1.5	0.3
Mouse 3	33.8	45.2	11.4	1.1	1.4	0.3
Average	31.9	42.9	11.1	1.1	1.5	0.4
Standard Deviation	2.6	2.4	3.4	0.2	0.1	0.2

Figure 38 – Table showing measured dielectric constant (ε) and effective conductivity (σ) S/m of triple-negative breast cancer tumours in an athymic nude mouse model. For each individual mouse, 5 consecutive measurements were taken using a slim-form co-axial probe in the same position. Measurements are shown are before and immediately after injection of PSMA-coated zinc ferrite nanoparticles (0.2 mg/mL; 10 µl) at 2.45 GHz. Calculated average and standard deviation are also shown.

From the table, we can see an average change in dielectric constant of 11.1 at 2.45 GHz and an average change in effective conductivity of 0.3 S/m. This is higher than was observed *ex vivo* which could be accounted for by the higher injected concentration and the blood perfusion. This may allow the injected material to disperse through the tumour. The calculated standard deviation values are mostly low, reaffirming the reproducibility of this trend between individual mice and tumours. This is an important consideration for translation to a patient setting, where breast composition is known to vary between individuals.

Further dielectric measurements were taken at 1h, 2h and 4h timepoints to examine the longevity of any observed contrast. As previously, a series of 5 measurements was taken for each mouse with the slim-form co-axial probe in the same position on the tumour surface. An average of these measurements was calculated. The average measured dielectric constant and effective conductivity (S/m) values can be seen in Figure 39.

	Dielectric Constant ε of tumour at 2.45 GHz	**Effective Conductivity σ (S/m) of tumour at 2.45 GHz**	**Dielectric Constant ε of tumour at 2.45 GHz**	**Effective Conductivity σ (S/m) of tumour at 2.45 GHz**	**Dielectric Constant ε of tumour at 2.45 GHz**	**Effective Conductivity σ (S/m) of tumour at 2.45 GHz**
	1 h post-injection	**1 h post-injection**	**2 h post-injection**	**2h post-injection**	**4 h post-injection**	**4 h post-injection**
Mouse 1	31.1	1.0	35.4	1.2	30.6	1.1
Mouse 2	35.8	1.1	32.6	1.1	31.2	1.0
Mouse 3	37.9	1.3	31.7	1.0	32.7	1.1
Average	34.9	1.2	33.2	1.1	31.5	1.1
Standard Deviation	3.5	0.15	1.9	0.1	1.1	0.1

Figure 39 - Table showing measured dielectric constant (ε) and effective conductivity (σ) S/m of triple-negative breast cancer tumours in an athymic nude mouse model. For each individual mouse, 5 consecutive measurements were taken using a slim-form co-axial probe in the same position. Measurements are at 1 h, 2 h and 4 h following the injection of PSMA-coated zinc ferrite nanoparticles (0.2 mg/mL; 10 µl) at 2.45 GHz. Calculated average and standard deviation are also shown.

At 1 h post-injection, measured dielectric constant values for all mice remain higher than the initial measured background value. However there has been a noted decrease relative to the post-injection value recorded. This could indicate some continued presence of injected PSMA-coated zinc ferrites in the tumour area. Tumours are known to have unusual angiogenesis, with leaking and misshapen blood vessels that could slow clearance of an injected agent from the tumour region. For two of the mice, dielectric constant values were consistent with their background measurements. By the 4 h timepoint, for all three measured mice, dielectric constant values return to equal or below the background measured for that individual. Effective conductivity (S/m) values are within the background range from 1 h post-injection.

3.4 Conclusion

Dielectric assessment of MDA-MB-231 triple negative breast cancer cells in suspension was conducted using the open-ended co-axial probe technique. Despite high cell density, and exploration of different suspension media and concentrations, no significant difference was found between media with and without cells, indicating that in the described setup the presence of cells could not be detected. Based on this, cells in suspension or measured as a monolayer were not regarded as a suitable model system for evaluation of nanoparticles. Conversely, pelleted cells of the same line showed a very different signature to those in solution, and even obtained similar values to known measured breast tissue. From a practical perspective however, pelleted cells were unsuitable as a model, leading to the progression to *ex vivo* measurements. While outside the scope of this project, it would be interesting from a progression perspective to explore profiles of different pelleted cell lines, to determine if there is an observable difference in the signatures.

Ex vivo dielectric properties form an essential component of model systems for microwave imaging/sensing. In these experiments, liver, skin, muscle, and fat tissues excised from athymic nude mice were evaluated for their dielectric properties. The results echo experiments performed on similar models, highlighting the unique dielectric profiles of individual tissues, as well as the variance that can exist between individuals. We also demonstrate that fat sampled in close proximity to tumours showed a higher measured dielectric constant than abdominal fat excised from the same animal. This is hypothesised to be due to the impact of tumour angiogenesis on the surrounding tissue and is an important consideration for microwave imaging/sensing systems based on dielectric contrast. As a part of the *ex vivo* studies, PSMA-coated zinc ferrite nanoparticles (0.06 mg/mL; 10 µl) were injected into excised triple-negative breast cancer tumours. When compared with reference tumour measurements, these tumours exhibited a small increase in dielectric properties, indicating their suitability for further examination as a MW imaging/sensing contrast agent.

Finally, a small-scale *in vivo* experiment was conducted using an athymic nude triple-negative breast cancer model. This study involved the direct injection of PSMA-coated zinc ferrite nanoparticles (0.2 mg/mL; 10 µl) into a mouse xenograft tumour model. The dielectric properties of the tumours were measured before and after the injection, with monitoring continuing over a period of 4 hours post-injection. The data show a notable increase in the dielectric constant post-injection, which is not observable four hours later. This indicates a short-lived change in the contrast is induced, which is desirable for an imaging agent. The particles were tolerated well, with no adverse effects noted in the injected animals in the hours following injection. While a wider scale *in vivo* experiment would be required to confirm and build upon these findings, this study represents a foundation for further research of these nanoparticles.

4: Development of a microwave hyperthermia (MWHT) lab setup

4.1 Introduction

Microwave technology is emerging as an exciting medical modality which can combine imaging and therapy, potentially using the same device. Through exploring microwave hyperthermia (MWHT) in conjunction with MW imaging/sensing, we can take a step towards a desirable theranostic approach to cancer treatments. This aligns well with the project goal of creating a spotlight on the true potential of the microwave applications in medicine and ensuring co-development of systems alongside nanoparticles (NPs).

Hyperthermia is an established therapeutic approach, which can be used in the treatment of cancers.[90,93,175,176] It involves the heating of specific regions, tissues or even across the whole body within the hyperthermia range (typically 40-45 °C). In the context of this project, we are exploring hyperthermia rather than ablation, which would be temperatures of over 45 °C.[177] In cancer, the hyperthermia is applied to the tumour area, altering cells in the tumour microenvironment, and promoting cell death. Hyperthermia is often used as an adjunctive therapy, with established research indicating that application of hyperthermia can improve the efficacy of other therapeutics such as chemotherapy and radiotherapy by increasing blood flow to the area and inhibiting DNA repair. [178,179] Research has shown *in vitro*, that hyperthermia induces a ‘heat shock’ leading to a suppression of angiogenic factors such as VEGF.[180] Angiogenic factors stimulate the generation of blood vessels, their suppression therefore could limit blood supply to the tumour. Research has also indicated a link between hyperthermia and the immune response to cancer [181], as well as the impact on the tumour microenvironment such as through temperature sensitive checkpoints.[182] Hyperthermia has progressed significantly since the early studies conducted in the 1960’s and 1970’s with successful application in numerous cancers including breast [176], brain [175] and bladder [183] among many others. Limitations include concerns around damage to surrounding tissues and heating at depth, which can be challenging when tumours are less easily accessible.

Hyperthermia is commonly applied using various modalities such as ultrasound, radio waves and microwaves. In recent years microwave technology has become more established as a promising modality for applying both hyperthermia and ablation. As hyperthermia can be applied both locally and regionally, different types of applicators and frequencies suitable to the application are used. Minimally invasive external applicators useful for surface tumours, while deep-seated tumours may require invasive endoscope or needle style applicators. Challenges remain however which include targeting and tissue specificity, particularly in tumours that are situated deep within the body [184], with concerns raised around damage to surrounding tissues. With microwave application, the dielectric properties are key, and give an indication of the interaction with particular tissues. [185] The distinct signature each tissue presents forms the basis for microwave imaging. In hyperthermia, the significance of these properties relates instead to their heat absorption, as tissues with higher water content such as muscle will absorb more heat.

Practically, application of MWHT varies, with a number of groups designing different application systems and antennas for both hyperthermia and ablation. A notable example is the balun-free microwave ablation antenna described by Luyen et al.[186] This design is intended to reduce the diameter of the antenna, thereby decreasing the invasiveness of the overall MWHT procedure, with experiments in *ex vivo* liver tissue demonstrating a similar ablation area when compared to other antenna types. Interestingly, this has the potential to be combined with a higher frequency range than is typical of microwave ablation, with efficacious ablation reported at 10 GHz.[187]

Particularly relevant to this thesis is the work of the Prakash group at Kansas State University.[188,189] Their angled monopole microwave antenna design incorporates a directional reflector to maximise the amount of signal reaching the target area. Tissue cooling has also been incorporated, with a continual water flow throughout the antenna. This antenna design has shown to be efficacious for *in vivo* application in a tumour model in rats.[190] The Prakash group has kindly provided the antenna for the experiments that will form Chapters 4 and 5 of this thesis.

Preliminary assessment of MWHT setups commonly involves the use of phantom model systems. These phantoms are carefully designed to mimic properties of specific tissues and are commonly characterised for their dielectric properties. This can give an indication of heat absorption of tissues at different frequencies, essential for translation to *in vivo* studies. Agar based phantoms are common, with the addition of salts and oils in varying quantities to mimic the permittivity of specific tissues.[29]

While there have been~~,~~ challenges associated with depth and localisation have brought the development of companion nanoparticles to the forefront of the field. Numerous formulations have been explored including gold [114,134], multi-walled nanotubes[68,110] and iron oxides.[191]

Relevant to this project, one such area of exploration is magnetic nanoparticles (MNPs), which have numerous applications throughout biology and medicine, such as MRI contrast agents. This pre-existing relationship with imaging and therapeutics means that they have also been characterised as contrast agents for MW imaging, as well as attenuators for MW hyperthermia. Controllable and adaptable synthesis methods are key to driving this research.

Notably, a publication by the Thanh group at UCL describes a synthesis of multi-core iron oxide nanoparticles [191]. Particles were synthesised by a microwave method and were citrate coated for stability and bioavailability. Alterations to input yielded particles of varying core sizes. Interestingly, when tested with magnetic heating, results demonstrated varying effects based on both the core diameter and the hydrodynamic diameter of the multi-core particle used. Overall, the study proposes an accessible and tuneable synthesis method, and clearly demonstrates the impact this can have on hyperthermia application.

Another interesting study by Garcia-Jimeno et.al [192] describes the use of ferrofluids and magnetoliposomes as companion nanoparticles in a microwave hyperthermia/ablation setting. In these experiments, tumour phantoms (mimicking their dielectric properties) were prepared incorporating varying concentrations of the nanoparticles and subjected to 5 minutes heating using a microwave system. Power was set to 10W at a frequency of 2.45 GHz. The magentoliposomes proved similarly effective and required a lesser concentration than the ferrofluid to achieve similar heating rates. These are promising results, demonstrating the ability of nanoparticles to be incorporated into a microwave system, however concentrations used per mL were quite high, which could prove challenging for clinical use. This highlights the need for further development of responsive nanomaterials that prove efficacious at lower concentrations.

4.1.1 Outline

Iron-based particles show promise not only in MW imaging/sensing, but also MWHT. This could look like zinc ferrite nanoparticles applied locally in the tumour region, allowing for enhanced MW imaging/sensing, followed by the application of MWHT for therapeutic purposes.

This chapter will investigate the optimal parameters of MWHT system in phantom model systems, before progression to *in vivo* experimentation. It is important to note that this setup is not commercially available as a complete entity, and significant time at the inception of this chapter was dedicated to sourcing and integration of appropriate components. The heating antenna itself is novel and was kindly provided by the group of Professor Punit Prakash (Kansas State University, Electrical Engineering). The antenna had previously been used for ablation purposes [193] as well as a hyperthermia study.[106] Full details of the setup and relevant components can be found in Materials and Methods.

Once the lab setup had been established, a series of phantoms were used to evaluate the antenna inclusive of heating and cooling profiles alongside the optimal settings and parameters for achieving hyperthermia. PSMA-coated zinc ferrites previously developed for MW imaging/sensing were explored as potential enhancer of MWHT. Finally, a pilot experiment was conducted *in vivo* demonstrating the ability of the setup to heat a tumour within the specified temperature range.

4.2 Aim & Objectives

4.2.1 Aim

To optimise parameters of a MWHT lab setup in phantoms to allow for use *in vivo.*

4.2.2 Objectives

1) To establish a functional MWHT lab setup suitable for testing in conjunction with nanoparticles.

2) To use tissue-mimicking phantoms to explore parameters and heating profiles.

3) Exploring MWHT with PSMA-coated zinc ferrite nanoparticles

4) Using outcomes from phantom experiments to determine parameters, pilot the MWHT setup *in vivo*.

4.3 Results & Discussion

4.3.1 MWHT lab setup

A 2.5 mm OD monopole antenna was provided by the Prakash group based in Kansas State University. This is similar to the antenna described in previous publications involving the group and has previously been used largely for ablation purposes.[105,132,194] Our aim was to incorporate this antenna into a lab MWHT setup, with the intent to be used to induce hyperthermia (42-45 °C). Specifically, the establishment of this setup would allow experimentation with nanoparticles for MWHT and progression to *in vivo* experiments. The setup incorporated the following elements: amplifier (NuWaves 12B01A-D30); signal generator (AnaPico APSIN4010HC); power supply (Tenma 72-8695) and peristaltic pump (Verderflex Economy EV045). Finally, to confirm functionality of the system, the S-parameters were measured using the Keysight Materials Measurement Suite.

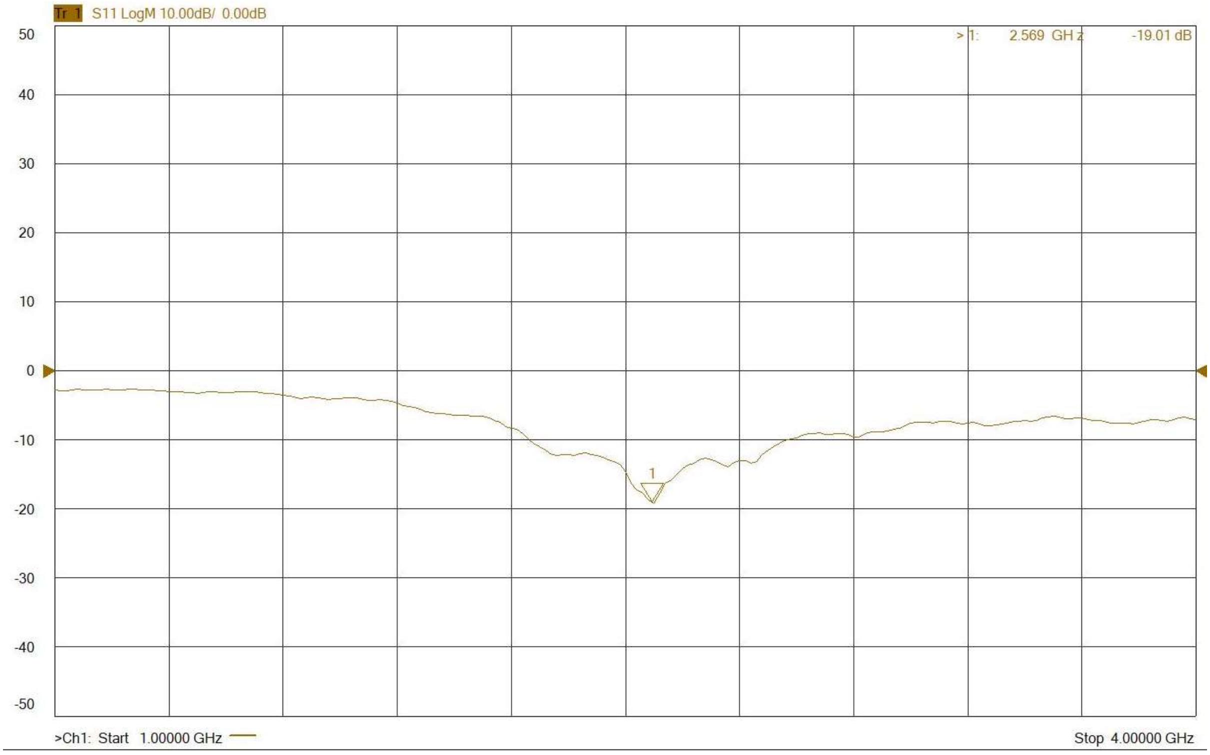

Figure 40 – Graphical representation of measured S11 scatter parameters for the MWHT setup taken over a range of 1 – 4 GHz.

The measured S-parameters are shown in Figure 40. These detail the reflection coefficient or power reflected from the antenna. The marker shown as ‘1’ in the diagram indicates the frequency at which most power delivered to the antenna is radiated. In this case, the value given is 2.569 GHz. Measuring the S-parameters is important to determine correct operation of the system, and to select the optimum frequency for operation of the antenna for MWHT. Following both discussion with the Prakash group and review of these data, 2.45 GHz was selected for further experiments, which is in line the frequency bands designated frequency bands for industrial, scientific and medical (ISM) use.

4.3.2 MWHT using a tissue model

Before progressing to more complex phantom models, it was essential to demonstrate a functional system in a solid medium. Therefore, a tissue model was setup using room temperature chicken breast. In this experiment, the antenna was placed directly on the tissue surface, with heating taking place over a period of 4 minutes. The signal generator was set to 24 dBm at a frequency of 2.45 GHz and the peristaltic pump at a flow rate of 18 mL/min with room temperature water.

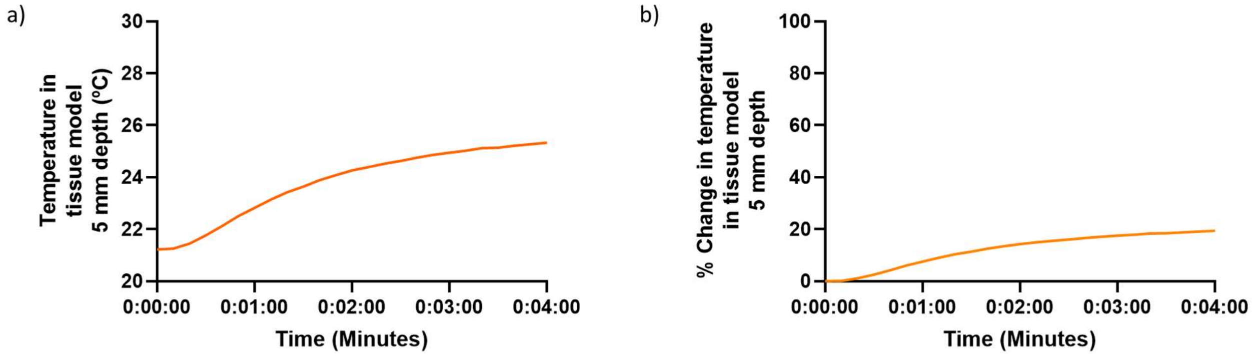

Figure 41 - Temperature change observed in tissue model at 5 mm depth over a period of 4 minutes. Panel a) represents the actual change in temperature observed. Panel b) shows the % change in temperature relative to the starting value.

As can be seen in Figure 41, despite the 24 dBm power input, a relatively small temperature of 4 °C over 4 minutes was observed. As represented in panel b), this is a change of approximately 20%. A longer period of application was not possible due to overheating of the amplifier. As this antenna was originally designed for ablation purposes, we would have expected a higher temperature increase at this stage. As an outcome of this experiment, a heat sink was purchased for the antenna, giving the final setup described below (Figure 42). This setup was used in all further experiments, including the *in vivo* studies. Full details are available in Materials and Methods.

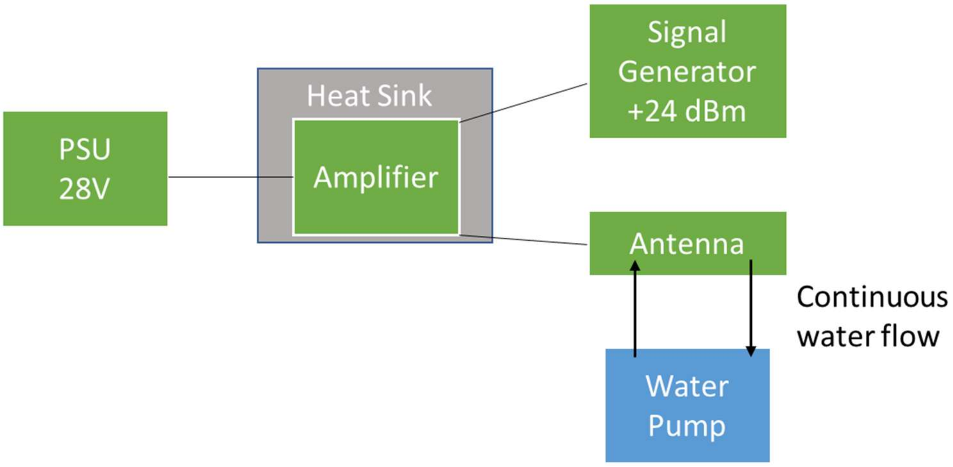

Figure 42 - Diagram detailing final hyperthermia setup. A power supply unit (PSU) at 28 V and signal generator at +24 dBM, 2.45 GHz are both connected to the amplifier by co-axial cable. The amplifier itself sits on a heat sink module and is directly connected to the antenna. Separately, a peristaltic pump provides a continuous water flow through the antenna at a rate of 18 mL/minute.

4.3.3 Exploring heating depth profile in agar phantoms

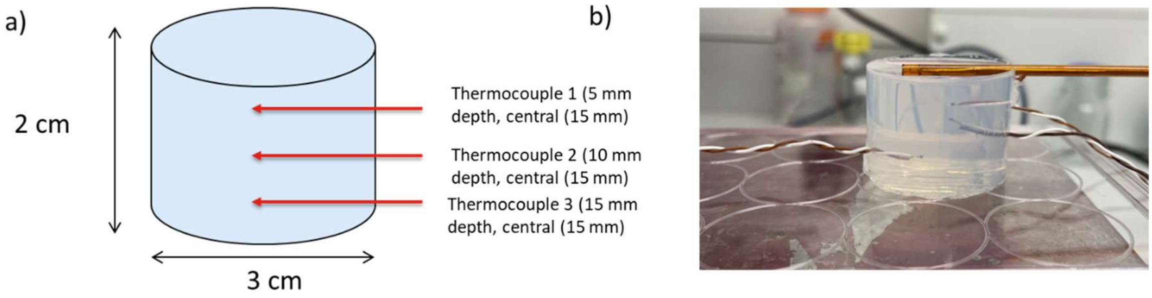

Figure 43 – Cylindrical agar phantoms. a) diagram of a cross section of the agar phantom, showing diameter, height and thermocouple placement. b) an image of the agar phantom, with thermocouples placed as described and the microwave heating antenna on the surface.

Now with a finalised setup, further experiments focused on establishing the optimum parameters for hyperthermia in the desired temperature range (40-45 °C). With thermocouple visibility presenting an issue for tissue models, modelling at this stage progressed to simple agar-based phantoms. This would allow careful placement of thermocouples at specific distances from the antenna to determine depth of heating. As depicted in Figure 43, a cylindrical 2% agar phantom was prepared, and thermocouples placed at 3 depth intervals (5 mm, 10 mm, 15 mm).

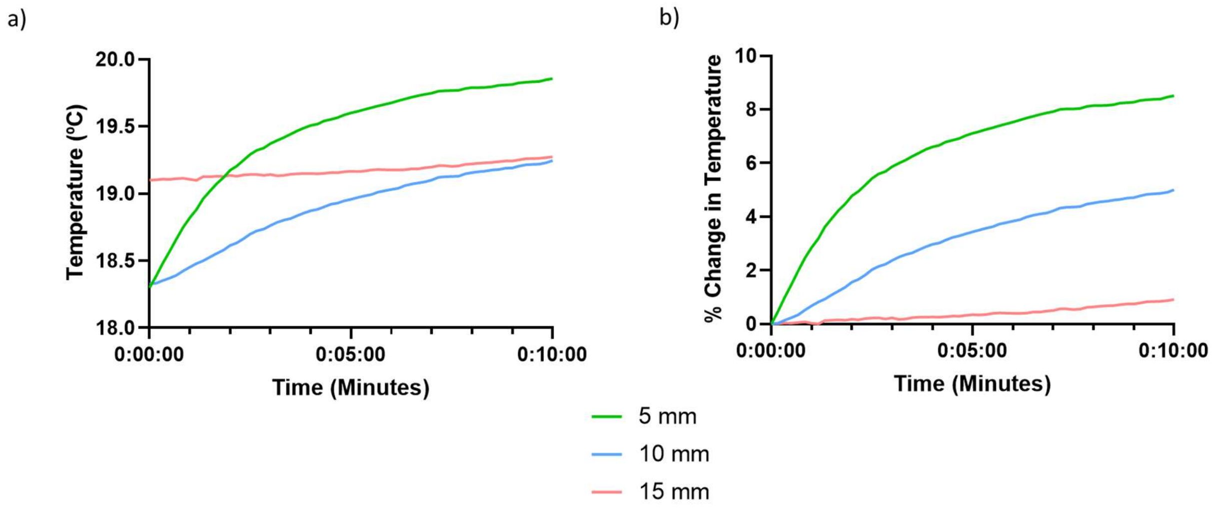

Figure 44 - Temperature profiles observed at 12 dBm in 2% agar phantom at 3 different thermocouple depths: 5 mm; 10 mm; 15 mm. Graphs show a) true temperature change over heating period; b) % change in temperature over heating period.

MW hyperthermia was applied over a period of 10 minutes using the previously described setup. Power input was scaled back for this experiment to 12 dBm, to ensure proper function of the newly installed heat sink module (NuPower PA Fan-Cooled Heatsink) over a longer period of heating, before experimenting with higher powers. Thermocouples were placed at different phantom depths using a needle applicator. The observed temperature profiles can be seen in Figure 44. In panel a) it is demonstrated that overall, a temperature change of less than 2 °C is observed, even at a 5 mm thermocouple depth. There are two key factors that may be influencing this; one is the power input and the other phantom composition. The % temperature change in panel b) demonstrates a temperature change of less than 10% at all thermocouple depths. Importantly, minimal temperature change is observed at 15 mm, which gives an early indication of the depth of heating. Analysing these results, further experimentation to evaluate different powers is necessary, with the incorporation of phantoms with appropriate dielectric properties. These are described below.

4.3.4 Using tumour phantoms to evaluate the impact of input power on temperature and cooling profiles.

To form a more complete picture of the possible heating profiles *in vivo*, phantoms mimicking the dielectric properties of tumours were used. Using an appropriate recipe from the literature [192], phantoms were prepared by that would display similar permittivity to breast cancer at 2.45 GHz (the chosen operating frequency for this antenna). The phantoms comprised agarose, distilled water, ethanol and NaCl (0.1 M) and were set in a small semi-spherical 6 mL mould to better mimic the curvature of a tumour surface. Full details are available in Materials and Methods. To confirm the dielectric properties of the phantom before heating, measurements were taken using the open-ended co-axial probe technique. Results are displayed in Figure 45.

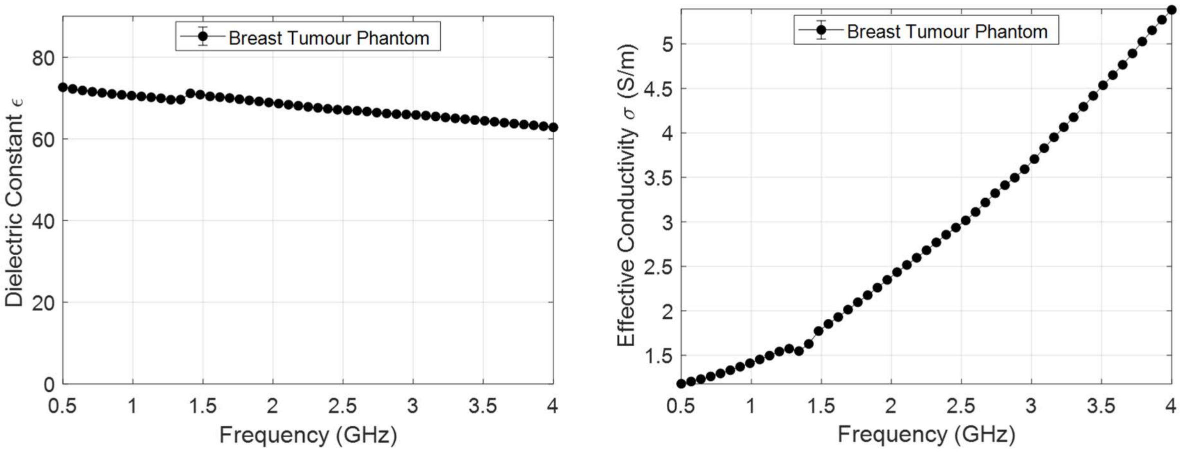

Figure 45 - Dielectric constant (ε) and conductivity (σ) (S/m) values of breast tumour mimic phantom measured over a frequency range of 0.5-4 GHz. Graph represents average measurements taken over 3 prepared phantoms, with each phantom also having 10 individual measurements. (n=3)

As is demonstrated there is an observed dielectric constant of approximately 64 at 2.45 GHz, this is in line with values for breast tumours in published literature. Similarly, the conductivity at 2.45GHz is 2.9, again in range of values published in the literature.[192] Importantly, these figures align with those taken in the *ex vivo* experiments described previously in Chapter 3, which used a triple-negative breast cancer line (MDA-MB-231) to induce tumours in athymic nude mice. This demonstrates consistency across the model systems we have utilised throughout this project; values can be seen Figure 46.

	Dielectric constant (ε)	**Effective Conductivity (σ) (S/m)**
Breast tumour phantom	64.2	2.9
***Ex vivo* triple negative breast cancer tumour in athymic nude mouse model**	58.5	2.2
Breast cancer tumour in literature [192]	59.4	3.2

Figure 46 - A comparison of relative permittivity and conductivity values at 2.45 GHz. Table shows values of: prepared breast tumour phantoms; *ex vivo* triple negative breast cancer tumours in an athymic nude mouse model; representative values of breast cancer tumours from the literature.

Once the dielectric profile of the phantom had been established, the phantoms were used to assess differing power inputs on heating and cooling profiles. This experiment was conducted to identify suitable parameters for pilot *in vivo* hyperthermia experiments, using the setup detailed below.

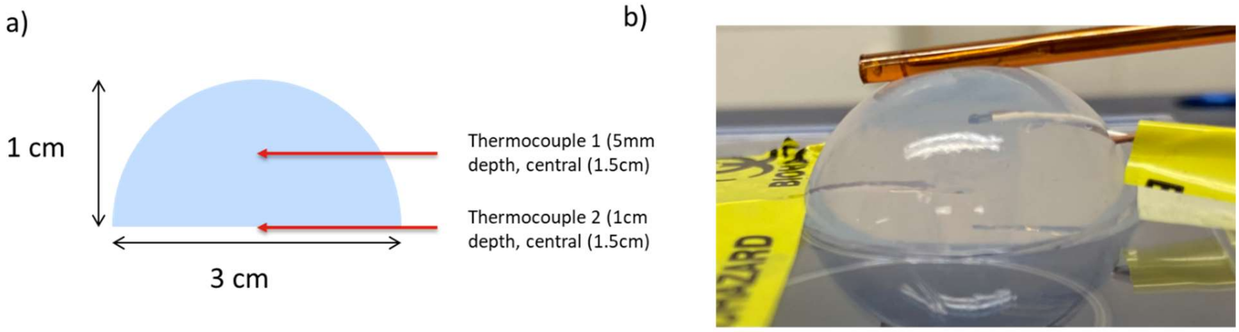

Figure 47 – Semi-spherical tumour mimicking phantoms. a) a diagram of a cross section of the tumour mimic phantom, showing diameter, height and thermocouple placement. b) an image of the prepared tumour mimic phantom, with thermocouples placed as described and the microwave heating antenna on the surface.

Figure 47 shows the tumour mimic phantom, which has a diameter of 3 cm and a height of 1 cm. The size of the selected phantom is larger than the expected tumour size *in vivo,* however smaller phantoms that mimic the exact tumour volume *in vivo* would not be practicable for this experiment. The curved surface of the phantom was selected to better mimic the tumour shape. The microwave heating antenna was placed in direct contact of the phantom surface, without any coupling medium. For temperature monitoring, thermocouples were placed at 5 mm and 10 mm depth using a needle applicator for precision. Heating was conducted over a period of 10 minutes, with the temperature monitored for a further 10 minutes following removal of the antenna to observe the cooling profile. Four different power settings were tested by altering parameters on the signal generator though frequency was kept constant at 2.45 GHz. These were: 12 dBm, 16 dBm, 20 dBm and 24 dBm.

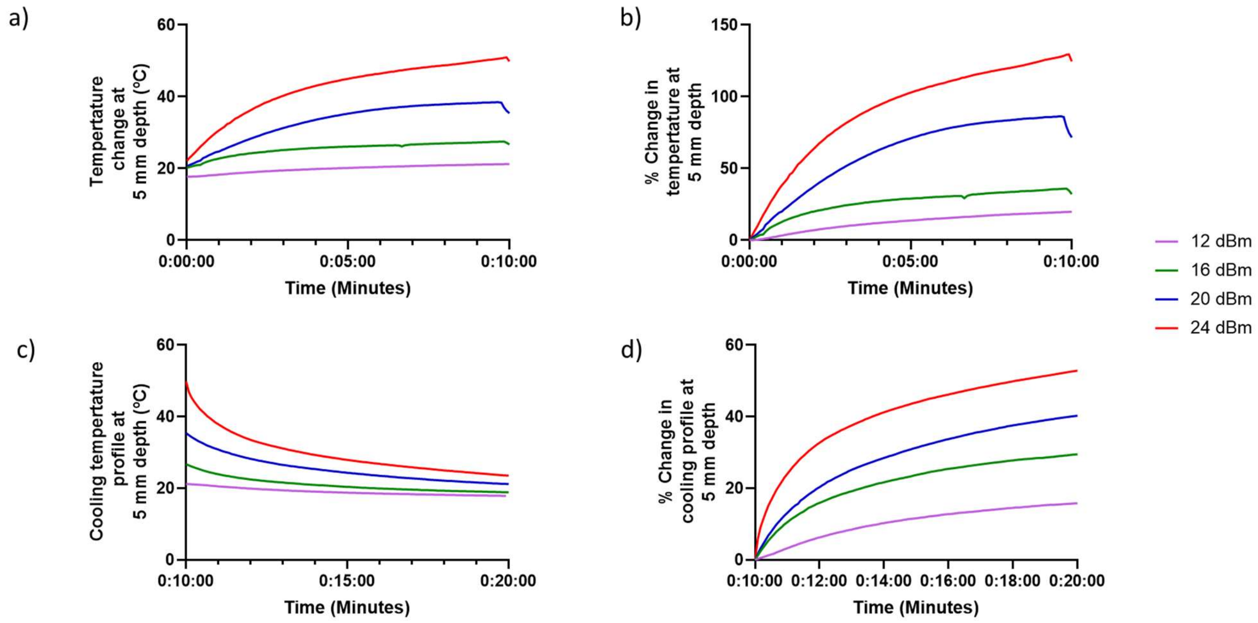

Figure 48 – Temperature profiles observed at different input powers in phantom mimicking breast tumour at 5 mm thermocouple depth. MW hyperthermia applied over a period of 10 minutes at power inputs of: 12 dBm, 16 dBm, 20 dBm and 24 dBm. Power terminated at 10-minute timepoint, and thermocouple readings taken for a further ten minutes to observe cooling profile. Graphs show a) true temperature change over heating period; b) % change in temperature over heating period; c) true temperature cooling profile; d) % change in cooling profile relative to peak temperature.

As can be observed in Figure 48 panel a), significant temperature differences were observed at the different input powers tested. At the top end of the spectrum, an input power of 24 dBm peaked at a temperature of 51 °C over a heating period of ten minutes. At an input of 12 dBm on the other hand, there is a peak temperature of 21 °C; a mere 3.5 °C increase from the starting temperature. Other powers ranged in between these two values, with 24 dBm providing the closest value for the hyperthermia target of 42 °C. Given the slight variation in start temperature of phantoms, these changes in temperature were also represented in percentage form, depicted in panel b). These findings are of particular significance to *in vivo* translation, as the typical treatment size for subcutaneous breast cancer tumour models is 5-6 mm. It is therefore essential to understand temperatures observed at this depth, to guide the decision on power input for *in vivo* studies. Equally important to determine are the cooling profiles. Following the 10 minutes of applied MW hyperthermia, the power was terminated, and the antenna removed from the surface of the phantom. No changes were made to the thermocouples and temperature monitoring continued for this period. As can be seen in panels c) and d), cooling profiles showed a direct relationship with input powers. Understandably, higher powers took longer to return to the starting temperature, having achieved a higher peak temperature. However, all powers tested had returned to within a 2 °C margin of their starting temperature in the 10-minute cooling period. This is essential knowledge for *in vivo* studies, where animals will not be culled following treatment and tells us approximately how long the tumour will remain at the desired temperature. From a treatment perspective, this can inform the estimated period of thermosensitive drug release and hyperthermic stress on the tumour microenvironment. For animal welfare, this can help to understand recovery and time take to return to normal body temperatures.

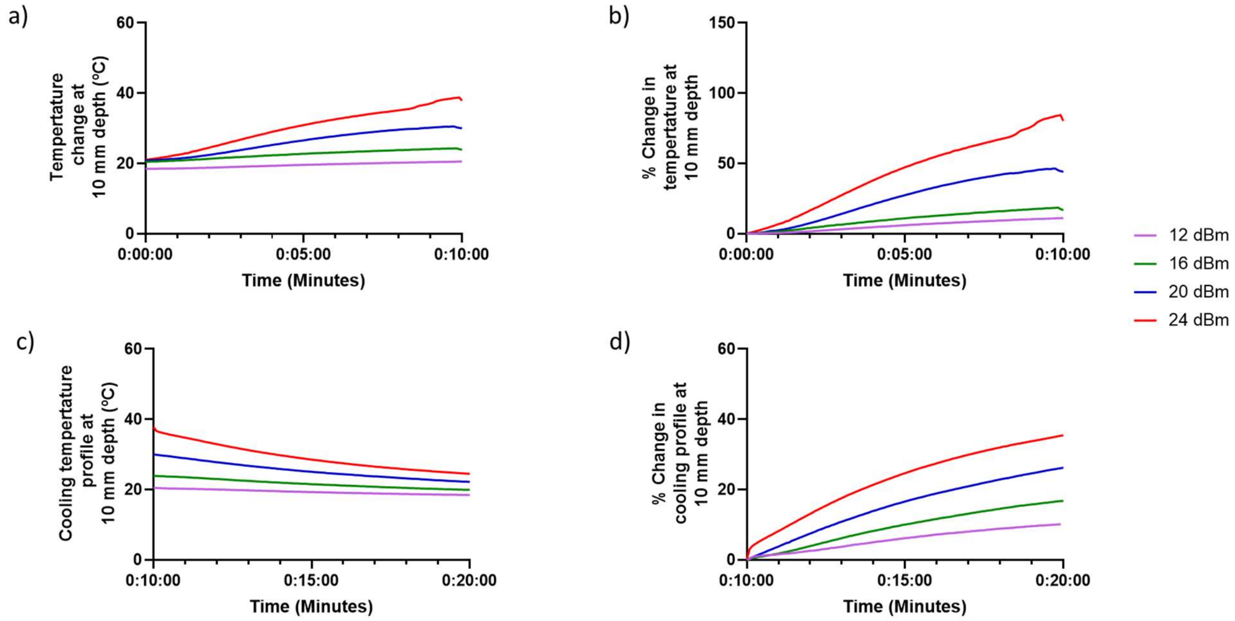

Figure 49 - Temperature profiles observed at different input powers in phantom mimicking breast tumour at 10 mm thermocouple depth. MW hyperthermia applied over a period of 10 minutes at power inputs of: 12 dBm, 16 dBm, 20 dBm and 24 dBm. Power terminated at 10-minute timepoint, and thermocouple readings taken for a further ten minutes to observe cooling profile. Graphs show

a) true temperature change over heating period; b) % change in temperature over heating period; c) true temperature cooling profile; d) % change in cooling profile relative to peak temperature.

Similarly, Figure 49 depicts the changes in temperature in identical conditions, but with data collected from a thermocouple at a depth of 10 mm. As can be seen in panel a) there is still a large shift in temperature at 10 mm depth at higher powers. At an input power of 24 dBm, the peak temperature reached at 10 minutes is 38.7 °C, which although falling below the range for hyperthermia, is still an increase of 16.5 °C from the phantom baseline temperature, an increase of nearly 85%. It is worth comparing this however to the 125% increase seen at 5 mm depth at the same input power. There is therefore a notable dissipation of heating. Cooling profiles represented in panels c) and d) demonstrate similar trends to the 5 mm depth data and again all input powers have returned to within 2 °C of the starting temperature comfortably within the 10-minute window.

When we compare the values from the 5 mm and 10 mm thermocouples, it is reassuring to see that while temperature increases are seen at a depth of 10 mm, the largest changes in temperature are observed at 5mm, which is line with proposed *in vivo* subcutaneous tumour sizes. This is of particular importance due to the earlier discussed concerns in MW hyperthermia regarding damage to surrounding tissues and lack of specificity. This is also an important consideration for translation *in vivo*, where damage to surrounding tissues could impact treatment survivability and animal welfare. The conclusions are overall positive, with the significant temperature increase seen to be at the 5 mm depth rather than the 10 mm. It is important to consider that in these experiments the antenna was in direct contact with the tumour phantom, and possible *in vivo* mitigations couple include positioning the antenna 1-2 mm above the tumour to reduce heating of surrounding tissues. The power setting data was also encouraging, demonstrating the ability of the antenna to achieve and even go above the desired 42 °C at an input power of 24 dBm. This observed combination of efficacious targeted heating in the desired temperature range demonstrates the viability of the antenna in this configuration to be translated *in vivo.*

4.3.6 MWHT with PSMA-coated zinc ferrite nanoparticles

Magnetic nanoparticles (MNPs) have been suggested as potential enhancers for MWHT through increased energy absorption.[132] Having demonstrated synthesised [PSMA]-$Zn_{0.06}Fe_2O_4$ nanoparticles to be MW sensitive materials in previous chapters in an imaging/sensing context, we were interested to explore their impact in a MWHT setting. Due to dispersion difficulties in solid phantoms, temperature profiles were observed in diH_2O. Characteristics of PSMA-coated zinc ferrite nanoparticles used in these experiments can be found in Figure 50.

Formulation	z-average size /nm	PDI
[PSMA]-$Zn_{0.06}Fe_2O_4$	117.8 (+/- 1.2)	0.20 (+/- 0.02)

Figure 50 - Characteristics of synthesised $Zn_{0.06}Fe_2O_4$ nanoparticles used for MWHT solution experiments. The table shows the measured z-average and PDI by DLS of PSMA-coated particles. Values shown are the calculated average of 3 individual DLS measurements +/- SD.

For these experiments 5 mL of test mediums were places in an appropriate vessel. A thermocouple was secured 5 mm from the hot spot of the antenna. $Zn_{0.06}Fe_2O_4$ was tested at a final concentration of 0.2 mg/mL. MWHT was applied for a period of 5 minutes at a frequency of 2.45 GHz and power of 24 dBm. Observed temperatures were measured and a change relative to the starting temperature of the solution was calculated. Results can be seen in Figure 51.

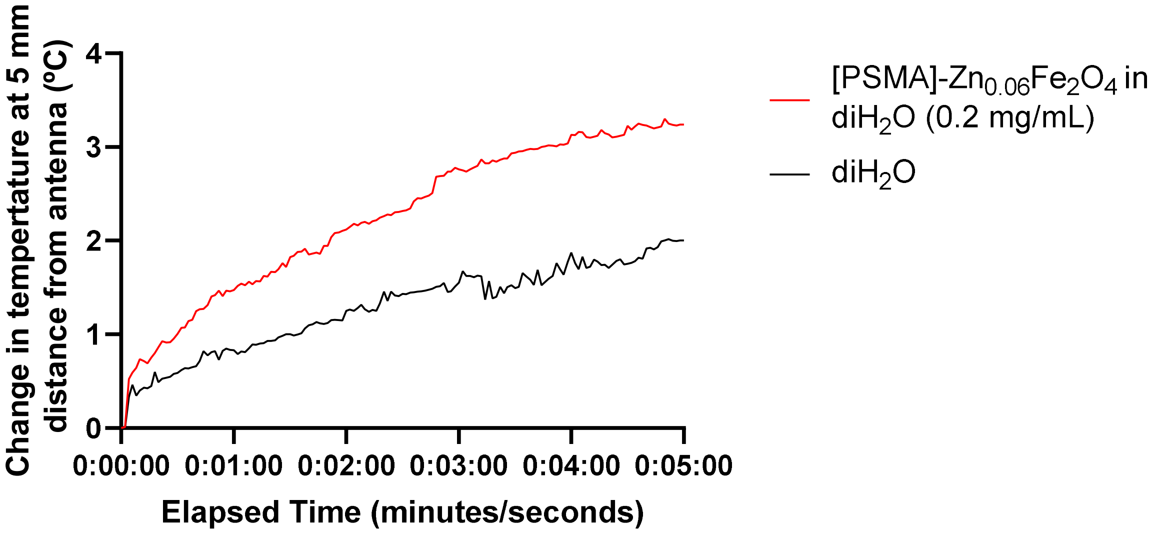

Figure 51 – Change in temperature (°C) observed over 5 minutes MWHT application in solutions. Thermocouples were secured 5 mm from the antenna surface. Power input was set to 24 dBm at a frequency of 2.45 GHz. $Zn_{0.06}Fe_2O_4$ was tested at a final concentration of 0.2 mg/mL. Water was used as a control. (n=3)

As can be seen from the presented data, it was observed over a period of minutes that an enhanced temperature increase was observed in the [PSMA]-$Zn_{0.06}Fe_2O_4$ nanoparticle solution vs diH_2O. Total change in temperature for the diH_2O was 2.0 °C vs 3.2 °C for the nanoparticle solution. This is an increase of just over 60%. While this is a limited experiment with small overall increases in temperature, it is perhaps indicative of the behaviour of PSMA-coated zinc ferrites and warrants further investigation.

4.3.7 Pilot in vivo *MWHT*

Having extensively characterised the MWHT system in phantoms, the next step involved pilot experiments *in vivo*. This presented an opportunity to trial the selected parameters determined from the phantom experiments to ensure that targeted heating in the desired temperature range (~42°C) was taking place.

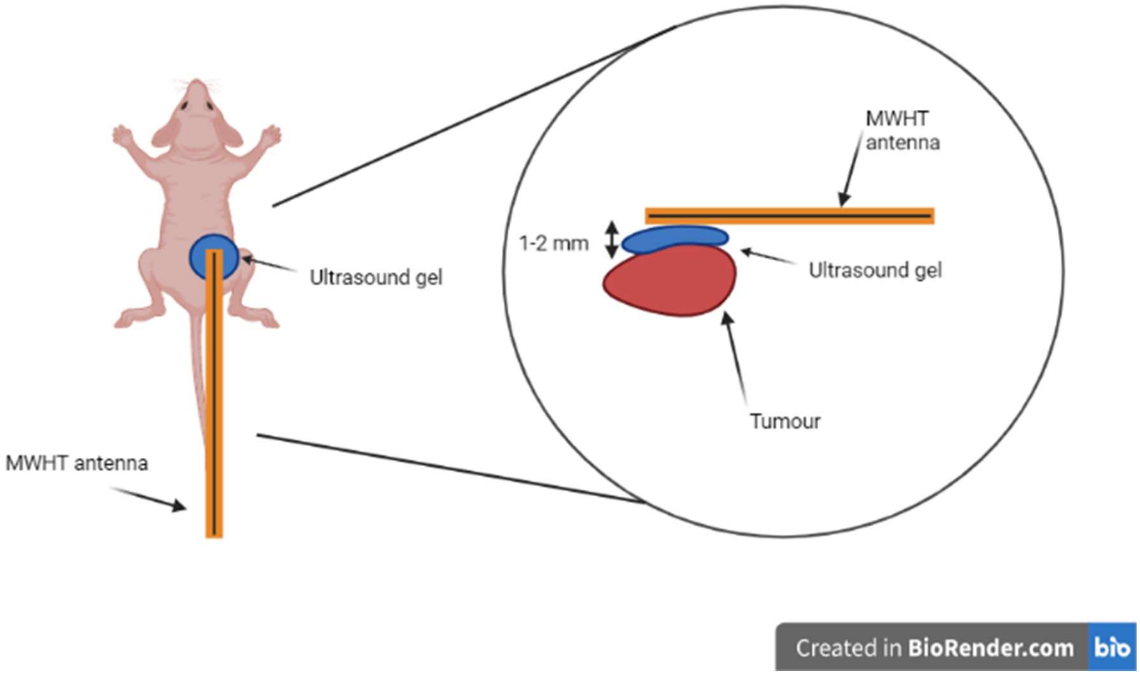

Figure 52 –Depiction of MWHT antenna positioning for *in vivo* experiments. MWHT antenna was placed directly over the tumour surface approximately 1-2 mm away from the skin. A pre-warmed water-based ultrasound gel was used to create a buffer/coupling medium. Created with BioRender.com.

These experiments used athymic nude mice with single triple negative breast cancer tumours (MDA-MB-231) induced on the flank. The tumour was heated using the microwave antenna over a period of 10 minutes at 24 dBm 2.45 GHz, mirroring the typical application length of high-intensity focused ultrasound (FUS). The antenna was placed 1-2 mm above the surface of the tumour, with water-based ultrasound gel used to create a coupling medium/buffer due to heat transfer inefficiencies observed in air (Figure 52). Owing to their composition, fine wire thermocouples were unsuitable for real-time temperature monitoring of the tumour in these experiments. As an alternative, a thermal camera (FLIR® Systems Inc., Wilsonville, OR, USA) was used to monitor temperature, with regular images taken before, during and after heating (0 minutes, 2.5 minutes, 5 minutes and 10 minutes). Images were recoloured in ImageJ using a calibration curve to estimate the tumour temperature, with temperatures of known surrounding entities in the images plotted, and the final image false coloured to give a tumour temperature estimate.

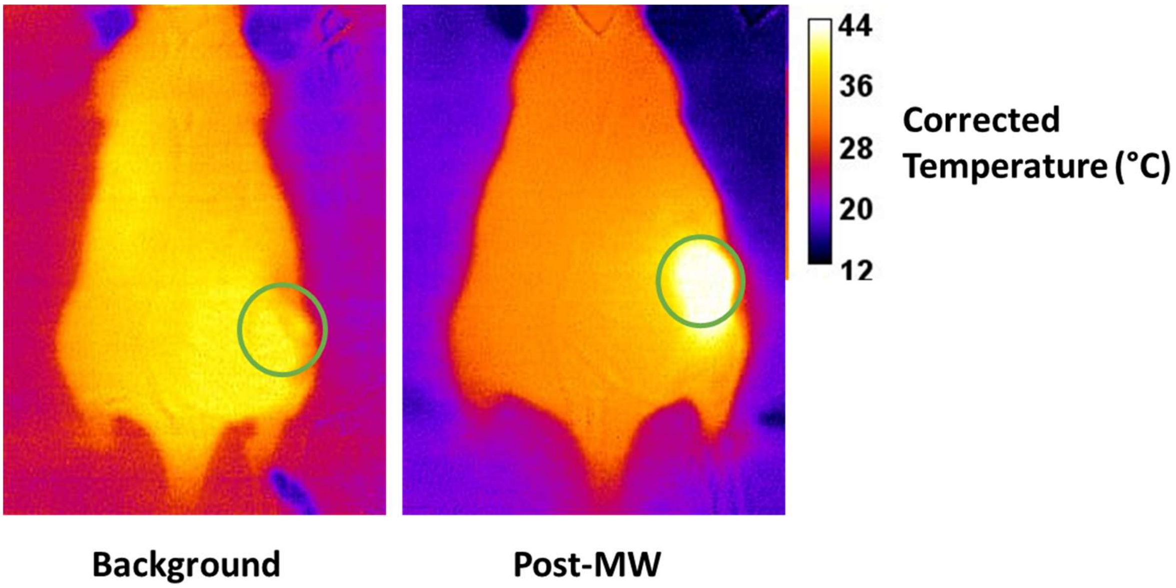

Figure 53 – Images depict recoloured thermal images taken before and after a period of ten minutes MW hyperthermia. Images were corrected in ImageJ using a calibration curve to give estimated tumour temperature. Flank tumours were induced using MDA-MB-231 in athymic nude mice and are highlighted in green in the image. Images representative of a study group containing minimum n=3 mice.

From Figure 53, we can see a clear alteration in tumour temperature following application of MW hyperthermia. Visibly during the experiments, there was a notable reddening of the tumour, indicating heating and higher blood perfusion to the area. Images were recoloured in ImageJ using a calibration curve, to provide an estimate of tumour temperature. From the image, it is estimated that the tumour reached a surface temperature of approximately 44 °C, which although higher than our temperature goal of 42 °C, is nonetheless within the hyperthermia range. Previous experiments using a similar antenna reported achieving temperatures of approximately 43 °C, demonstrating the functionality of this setup.[194] The images indicate minimal temperature increases at surrounding areas, demonstrating the potential of the setup for targeted heating. MW hyperthermia was tolerated well, with no surface skin burns or other adverse effects to the animals noted in the days following application. From these data, it was determined that the MW hyperthermia setup was suitable for larger scale *in vivo* experimentation.

4.4 Conclusion

In conclusion, in this chapter we have established and tested a lab MWHT system using a 2.5 mm OD monopole antenna. Using phantom model systems, we have explored parameters such as heating depth and input powers with a view to translate the system *in vivo*. In doing so, we have demonstrated the importance of using appropriate dielectric phantoms in the testing of model systems and have outlined the additional considerations such as blood perfusion when selecting power input for *in vivo* experimentation. We also assess the heating profile of zinc ferrite nanoparticles in solution. Finally, we demonstrate the ability of this setup to heat a subcutaneous tumour successfully and selectively in a triple negative breast cancer mouse model. Overall, these data suggest the suitability for this system to be used in further *in vivo* experiments with a possibility to combine with PSMA-coated zinc ferrite nanoparticles.

5: Nanoparticles in conjunction with microwave hyperthermia (MWHT) for the treatment of triple negative breast cancer

5.1 Introduction

One of the key objectives of this project is to highlight the emerging potential of microwave technologies in conjunction with adjuvant nanoparticles. External microwave antennas can be used to selectively heat targeted areas non-invasively using in both ablative and hyperthermia temperature ranges.[189,193,195] This technology has the potential to be combined with thermosensitive therapeutics to further control and amplify its therapeutic efficacy. Pre-clinical small animal models provide an excellent basis for the advancement of novel therapeutic intervention, often helping to determine efficacy and dose. With this in mind, *in vivo* validation represents a key step in MWHT studies.

Antennas designed for small-animal models have formed an important part of MWHT research, facilitating pre-clinical studies. An interesting paper by Curto et al. describes the development of an *in vivo* 2.45 GHz MWHT system designed specifically for small animals. In this study, 15 minutes of MWHT at 20 W input power was applied using a directional 3.5 mm (OD) antenna on mice bearing 4T1 tumours, with hyperthermia profiles assessed using MR thermometry.[105] The setup (seen in Figure 54) proved an efficacious platform for *in vivo* research, using MRI-suitable materials to avoid interference from the antenna. Measurements indicated a change in in temperature of approximately 11 °C in the tumour region 2.3 mm from the antenna.

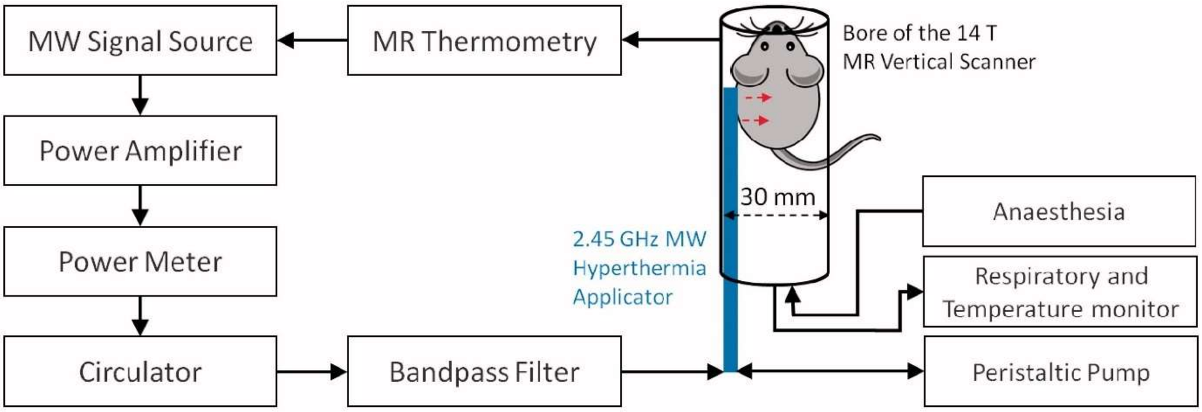

Figure 54 - Block diagram of small-animal microwave hyperthermia system integrated with 14 T MR thermometry. Reprinted from ref.[105]

Magnetic nanoparticles (MNPs) have been suggested as potential enhancers for MWHT through increased energy absorption, resulting in improved heating. In one study, spherical iron/iron oxide with 10 and 20 nm diameter were dispersed in liver tissue-mimicking phantoms at varying concentrations (5mg/mL and greater).[132] MWHT was applied at 2.45 GHz using an interstitial dipole antenna, and the transient temperature profiles subsequently measured at different phantom depths. Relative to the control phantoms, MNP phantoms showed enhanced heating rates of up to 0.28 °C per second as well as an increased radial heating distance. The concentration of MNPs used in this study was high, as an equivalent injected dose would prove challenging to translate into mouse models or people. Nonetheless these experiments highlight the potential of nanoparticles to enhance heating profiles.

Further enhancement of MWHT systems could potentially be achieved through combination with thermosensitive therapeutics. Thermosensitive liposomes (TSLs) are nanoparticles where release of the encapsulated drug is triggered in response to mild hyperthermia of approximately 42°C, with early research taking place in the 1970's.[196] A simplified scheme can be seen in Figure 55. This can provide a targeted therapeutic with local drug delivery. Great progress has been made in the area in recent years, with TSL formulations progressing to clinical trials. Examples include phase 1 trials of TARDOX, a thermosensitive liposome encapsulating doxorubicin for liver tumours activated by high frequency focused ultrasound (HIFU).[197] The trial found the treatment to be safe and efficacious, enhancing drug delivery to tumours in participating patients by up to ten-fold. Similarly, in breast cancer a phase 1 trial involving 29 patients also used a liposomal doxorubicin and demonstrated safety while examining dose response.[198] Interestingly, this trial used two different hyperthermia approaches: 915 MHz microwave applicators or ultrasound. Patients in this trial had quite advanced disease, and so it was more difficult to determine efficacy outcomes, however nearly half of the participants demonstrated local control following treatment.

TSL clinical trials have also reached phase 3, with ThermoDox, a lysolipid thermosensitive liposome formulation encapsulating doxorubicin that is used in combination with radiofrequency. [199] This trial focused on the treatment of hepatocellular carcinoma, but despite showing safety, results showed survival was not significantly increased in treatment groups. Despite this, active phase 1 trials are currently recruiting for ThermoDox application in pancreatic tumours (NCT04852367) as well as several paediatric cancers (NCT04791228, NCT02536183). The described studies showcase the wide variety of hyperthermia techniques including microwaves, radiofrequency and HIFU, further cementing the potential for MWHT applicators in this area.

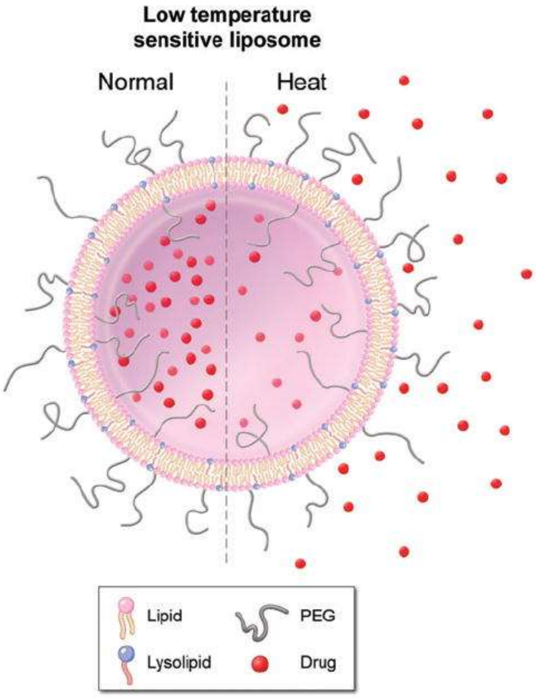

Figure 55 - Low temperature sensitive liposome (LTSL): Lipid bilayer, which encapsulates (chemo-) therapeutic agents. They rapidly release their payload in response to heat. Reprinted from ref. [200]

Moving forwards, advances in development of TSLs has focused on their combination with imaging modalities, which can be achieved by the incorporation of adding imaging components such as fluorescence molecules as well as MRI and PET contrast agents.[201] In addition, a shift into personalised medicine is occurring with the incorporation of a wider range of drugs tailored to the patient treatment regime. Relevant to this project, TSLs have also been shown to be capable of encapsulating more than one drug, providing dual delivery of chemotherapy agents.[202] These experiments used an athymic nude mouse model for triple-negative breast cancer to test the efficacy of TSLs delivering both carboplatin and SN-38. This was achieved by encapsulating carboplatin in the liposome core and embedding the SN-38 in the lipid membrane. Results showed statistically significant increases in survival and tumour growth suppression in groups treated with the TSLs in combination HIFU. The TSLs also incorporated an MRI lipid, allowing for image monitoring.

Research has also demonstrated the potential of MWHT in conjunction with thermosensitive therapeutics. A previous study using a similar directional 2.45 GHz antenna design to our lab MWHT setup was conducted *in vivo* in rats, with application of mild MWHT and TSLs encapsulating the chemotherapy drug doxorubicin (TSL-Dox).[194] The experiments used a BN175 sarcoma cell line to induce flank tumours in rats and infused TSL-Dox at 7 mg/kg before applying 15 minutes of MWHT at 42 °C using the directional antenna at 2.45 GHz. Results demonstrated a 2.6-fold increase in tumour doxorubicin uptake in heated tumours vs unheated, determined by fluorescence imaging. They also present a novel approach to the removal of excess drug from the circulatory system, aiming to reduce cardiotoxicities that have been associated with doxorubicin therapies.[203] Overall, this study demonstrates the potential of combining MWHT with thermosensitive drug delivery.

5.1.1 Outline

In the previous chapter, we demonstrated the ability of the MWHT setup to provide targeted heating *in vivo* in an athymic nude triple-negative breast cancer mouse model. In this chapter, we will evaluate this MWHT setup through further *in vivo* experiments, seeking to combine this targeted heating modality with thermosensitive therapeutics and microwave-sensitive nanoparticles and assessing for efficacy.

Work in my research group also includes development of image-guided drug-loaded thermosensitive liposomes (iTSLs), typically activated by high-intensity focused ultrasound (HIFU) for targeted therapeutics. A dual-loaded formulation tested *in vivo* in conjunction with HIFU proved extremely efficacious and demonstrated decreased tumour growth and a 2.5-fold increase in overall survival relative control.[202] This presented an opportunity to test the MWHT setup as a targeted delivery system, creating a mirror study those performed with HIFU. In addition to this, previous chapters have detailed the synthesis and dielectric characterisation of zinc ferrites coated with PSMA (Poly(styrene-co-maleic anhydride), confirming them to be microwave-responsive nanomaterials. Experiments in the previous chapter indicated PSMA-coated zinc ferrites caused a change in the temperature profile when exposed to MWHT. Therefore, we were interested to explore the impact of the combination of these particles and iTSLs in an *in vivo* MWHT setting, laying the foundation for future work in combining microwave imaging/sensing, therapeutic intervention and MWHT.

The following studies used an athymic nude mouse model with xenograft triple-negative breast cancer tumours to determine the biodistribution and uptake profiles as well as efficacy by survivability, aligning with the project goals of developments in the imaging and treatment of breast cancer.

5.2 Aim & Objectives

5.2.1 Aim

The aim of this chapter is to investigate if a lab MWHT system *in vivo,* can activate drug delivery by inducing hyperthermia. Drug-loaded thermosensitive liposomes (iTSLs) will be used in conjunction with MWHT and PSMA-coated zinc ferrites as a potential MWHT enhancing agent.

5.2.2 Objectives

1) To observe the effect of MWHT with and without PSMA-coated zinc ferrite nanoparticles on the biodistribution of drug-loaded thermosensitive liposomes.

2) To evaluate the effect of MWHT with and without PSMA-coated zinc ferrite nanoparticles on the tumour uptake of drug-loaded thermosensitive liposomes.

3) To determine the efficacy of MWHT in combination with drug-loaded thermosensitive liposomes and PSMA-coated zinc ferrite nanoparticles in a xenograft mouse model.

5.3 Results & Discussion

5.3.1 PSMA-coated zinc ferrite nanoparticles

Preparation of PSMA-coated zinc ferrite nanoparticles was conducted as previously described in Chapter 2. Briefly zinc ferrites were synthesised by thermal decomposition using $Zn(acac)_2$ and $Fe(acac)_3$ as precursors. Oleic acid and oleylamine were used as capping agents. Size selection yielded nanoparticles of approximately 10 nm in size, measured by TEM (Figure 56). Particles were phase transferred into water using PSMA polymer (Poly(styrene-co-maleic anhydride)). Once coated, the size and PDI of the particles were determined via DLS measurements (Figure 56) showing a size of approximately 130 nm. This formulation was selected as previous *in vivo* experiments (outlined in Chapter 3) demonstrated an increase in the measured dielectric properties of tumours following direct injection of [PSMA]-$Zn_{0.06}Fe_2O_4$. As outlined previously in Chapter 2, stability of these particles is at least 30 days, which was more than sufficient for the purposes of these studies. Zn and Fe content for this batch were confirmed by ICP-MS; uncoated particles were also characterised by TEM imaging.

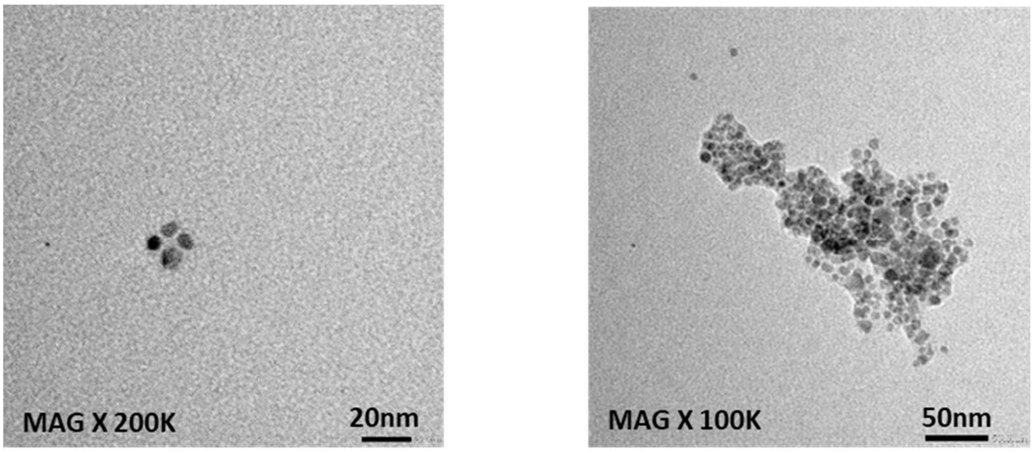

Formulation	z-average size /nm	PDI
[PSMA]-$Zn_{0.06}Fe_2O_4$	130.8 (+/- 1.6)	0.16 (+/- 0.03)

Figure 56 - Characteristics of synthesised $Zn_{0.06}Fe_2O_4$ nanoparticles used for *in vivo* experiments. Panels show TEM images of the uncoated particles taken at X100K and X200K. The table shows the

measured z-average and PDI by DLS of PSMA-coated particles. Values shown are the calculated average of 3 individual DLS measurements +/- SD.

5.3.2 Drug-loaded thermosensitive liposomes (iTSLs)

Thermosensitive liposomes were prepared in accordance with Cressey et al. [202] using a film hydration method. Full details are available in Materials and Methods. The incorporation of a gadolinium lipid conjugate in the liposome bilayer was included to ensure that the formulation matched that in published data using HIFU.[202] This would allow the data from the studies to be cross compared. The inclusion of the gadolinium lipid also served the purpose of allowing downstream tumour uptake to be determined by gadolinium content. NIRF labelling was included to allow tracking of liposome biodistribution *in vivo*. Figure 57 gives an outline of the determined characteristics of iTSLs used for *in vivo* experiments in this chapter. The size and PDI of the particles were determined via DLS measurements, showing a size of approximately 129.5 nm.

Formulation	**z-average size /nm**	**PDI**	**SN-38 concentration (mg/mL)**	**Carboplatin concentration (mg/mL)**	**Gadolinium concentration (mg/mL)**
$\text{iTSL}_{\text{SM/CC}}$	129.5 (+/-3.5)	0.27 (+/0.02)	0.97 (+/- 0.05)	0.47 (+/- 0.02)	1.23 (+/- 0.1)

Figure 57 - Characteristics of iTSLs used for *in vivo* experiments. The table shows the measured z-average and PDI by DLS. Values shown are the calculated average of 3 individual DLS measurements +/- SD.

5.3.3 MWHT Setup

The microwave setup used in these experiments is as described in Chapter 4 and can be seen depicted in Figure 58, with full details available in Materials and Methods.

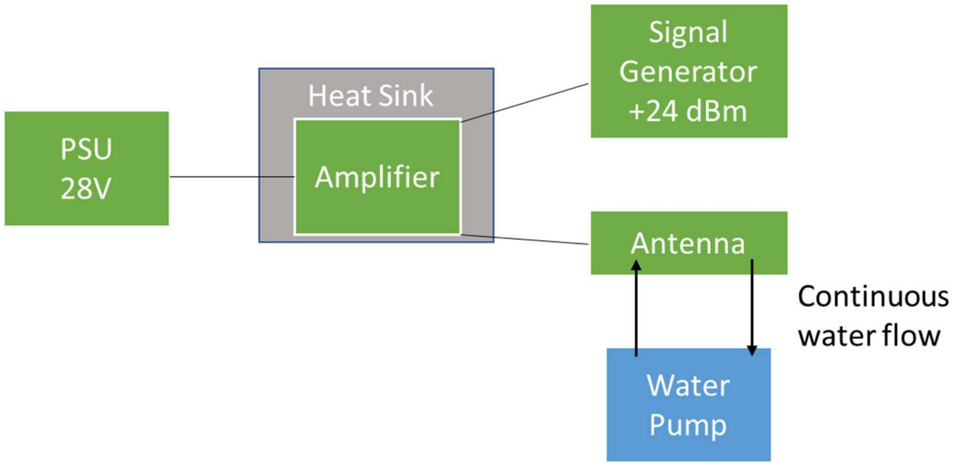

Figure 58 - Diagram detailing final MWHT setup. A power supply unit (PSU) at 28 V and signal generator at +24 dBM, 2.45 GHz are both connected to the amplifier by co-axial cable. The amplifier itself sits on a heat sink module and is directly connected to the antenna. Separately, a peristaltic pump provides a continuous water flow through the antenna at a rate of 18 mL/minute.

The antenna was horizontally placed to ensure the alignment of the focal point with the tumour region. As previously discussed, a reflector in the antenna deflects the signal to optimise heating in a single direction. For all experiments, the antenna was placed approximately 1-2 mm from the flank tumours and ultrasound gel applied between the surface of the antenna and the skin. Direct skin contact with the antenna comes with a risk of surface burns; therefore, a small distance was required. A water-based ultrasound gel was therefore used to aid heat transfer as this would be ineffective through air. The frequency set on the signal generator was 2.45 GHz, with a power of + 24 dBm; the PSU was set to 28 V. Hyperthermia was applied for a period of ten minutes, with regular temperature monitoring by thermal camera. During this time, no alterations were made to power input or water flow (18 mL/minute). Water flow rate was selected to promote heating in the hyperthermia range, with lower flow rates associated with tissue ablation. For this setup used *in vivo*, simulations by the

Prakash group indicate a power output of approximately 3.3 W at the antenna connector, with approximately 2.7 W transferred to tissue. The system proved simple to use once established and easy apply to an *in vivo* setting. A thermal camera (FLIR® Systems Inc., Wilsonville, OR, USA) was used to monitor temperature, with regular images taken before, during and after heating (0 minutes, 2.5 minutes, 5 minutes and 10 minutes). Images were recoloured in ImageJ using a calibration curve to estimate the tumour temperature, with temperatures of known surrounding entities in the images plotted, and the final image false coloured to give a tumour temperature estimate. A representative example of the heating profiles observed in this chapter is given in Figure 59.

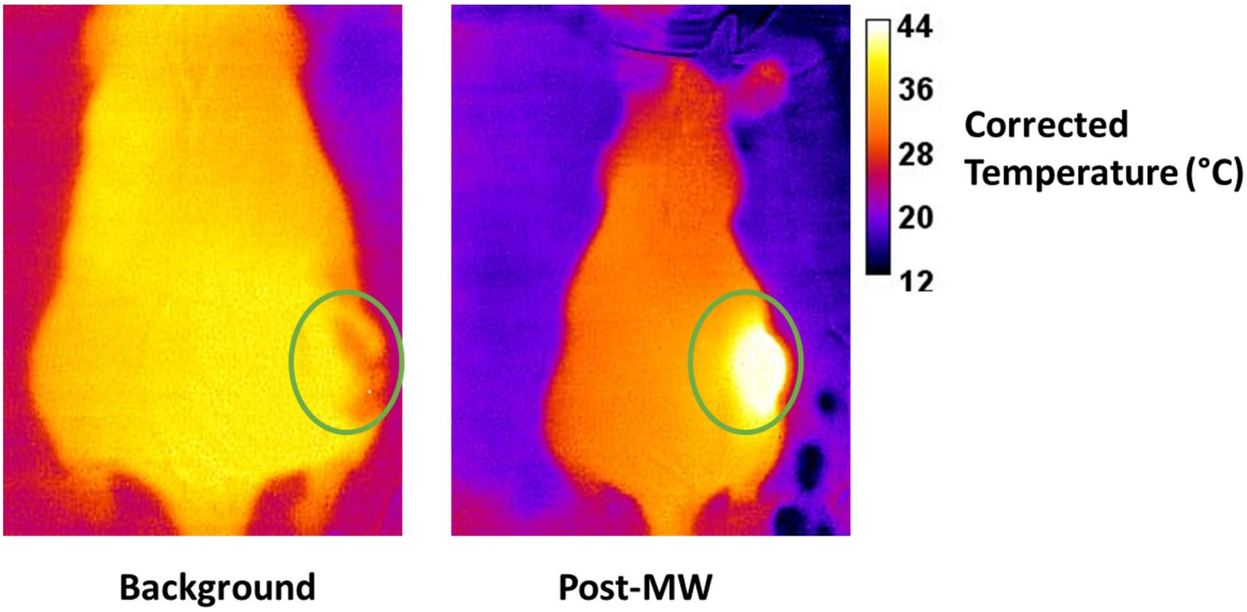

Figure 59 - Images depict recoloured thermal images taken before and after a period of ten minutes MW hyperthermia. Images were corrected in ImageJ using a calibration curve to give estimated tumour temperature. Flank tumours were induced using MDA-MB-231 in athymic nude mice and are highlighted in green in the image. Images representative of MWHT applied in this chapter.

5.3.4 In vivo *biodistribution*

The aim of this experiment was to evaluate the effect of applied MWHT on drug-loaded thermosensitive liposomes (iTSLs), typically activated by High-Intensity Focused Ultrasound (HIFU). A scheme of the experimental design can be found in Figure 60. As previously, athymic mice bearing single flank tumours using MDA-MB-231 were used as a model system; iTSLs (10 mg/kg SN-38) were infused by tail vein injection, PSMA-coated zinc ferrite nanoparticles were injected intra-tumourally at a concentration of (10 µl; 0.2 mg/mL). MWHT was immediately applied to relevant groups using the previously described antenna setup, for a period of 10 minutes at approximately 42 °C. NIRF images were used to track biodistribution, with background images taken before injection, and then at regular intervals post-injection. Temperature monitoring was conducted using thermal camera images at regular time intervals. Both NIRF and thermal camera images were processed in ImageJ to provide clear information, with care taken to ensure adjustments for comparable images were on the same scale.

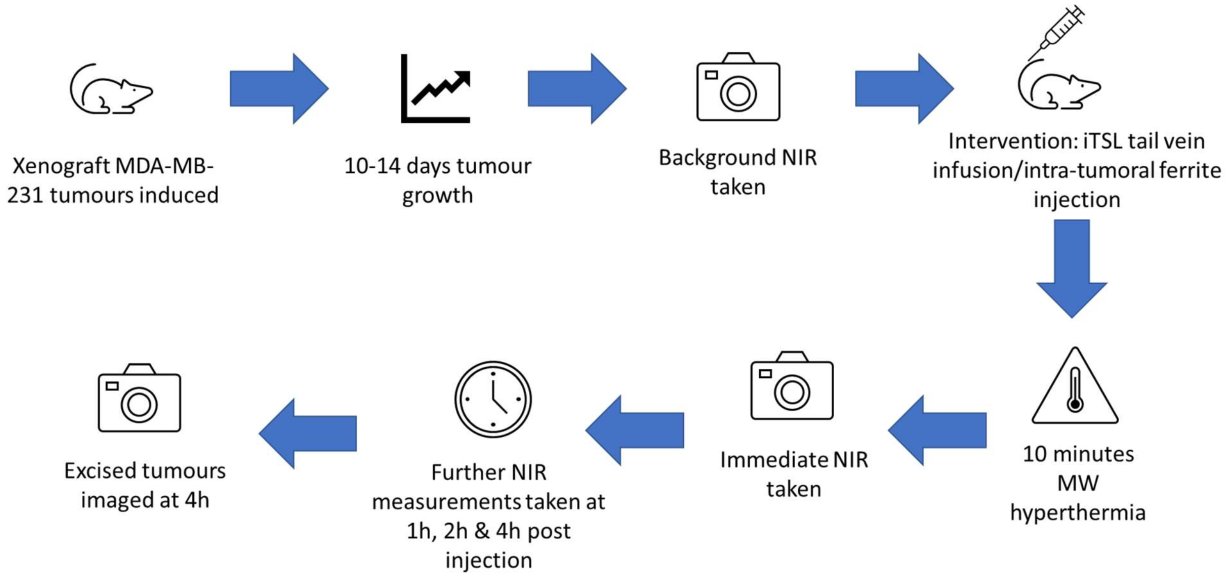

Figure 60 - Scheme shows a basic experimental overview of the *in vivo* biodistribution study. Xenograft MDA-MB-231 tumours are induced and grown to approximately 7-8mm Ø with background NIR images establish a baseline. Group dependent intervention including one from or a combination of: (i) IV injection of iTSL (10 mg/kg SN-38); (ii) intra-tumoural ferrite injection 10 µl (0.2 mg/mL); (iii) applied MW hyperthermia over 10 minutes.

Through the imaging of the NIRF lipid-conjugate dye (CW800.DSA, Ex 775 nm, Em 795-850 nm), the biodistribution can be visualised, with greater insights given through taking both dorsal and ventral images. Images were taken pre- and post-injection, and then at regular time intervals of 1h, 2h and 4h. Previously published studies using these iTSLs monitored uptake into the tumour over a 24h period, with NIRF images demonstrating a peak at the 4h timepoint; therefore 4h was selected as the endpoint for this study [202]. At 4h animals were humanely culled, and the tumours excised for downstream uptake analysis.

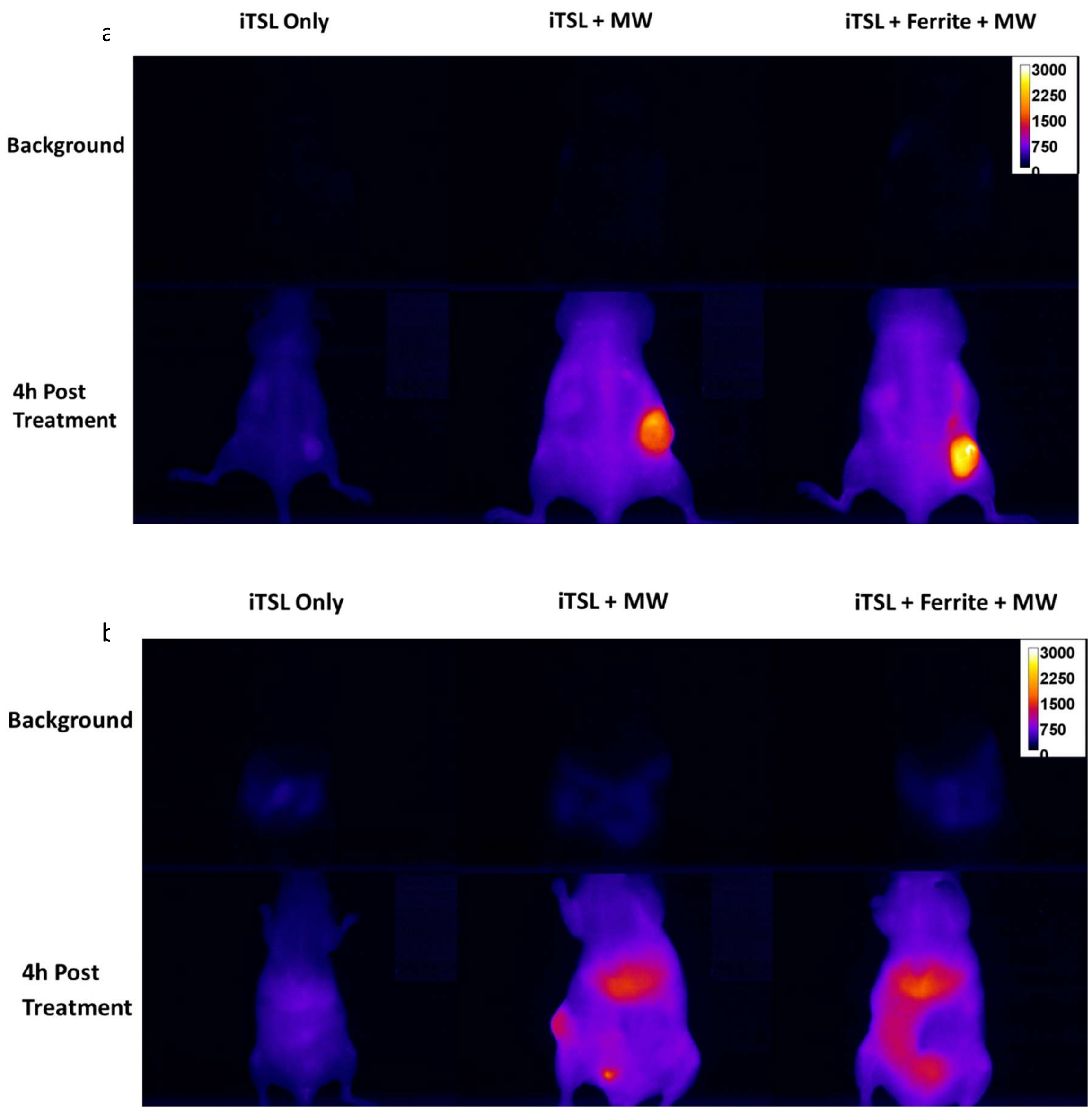

Figure 61 - Images show a) dorsal and b) ventral images demonstrating the *in vivo* biodistribution of iTSL in athymic nude mice with single flank MDA-MB-231 tumours. Uptake monitored using NIRF images taken on Maestro EX multispectral analyser, with fluorescence excitation at 704 nm and emission collected in 10 nm steps over 740 – 950 nm. Images subsequently unmixed using appropriate spectral library (iTSL in buffer) and adjusted for colour and contrast using standard research group protocols. Panels from left to right; iTSL only, iTSL + MWHT and iTSL + Ferrite + MWHT. All groups represented above received IV infusion of iTSL. Ferrite groups then additionally injected intra-tumourally with 10 µl ferrite nanoparticles in diH_2O. MWHT groups were subjected to 10 minutes of applied MWHT following infusion and/or injection. Upper panels represent the

background images taken pre-treatment, while the lower panels depict 4h post-treatment. Images shown depict animals representative of a wider study group.

As seen in Figure 61, relative to background, the ‘iTSL only’ group at 4 h shows a fairly balanced distribution, noting only that the slight lightening of the tumour may indicate a small amount of uptake of iTSL’s in this area. Similarly ventral images give the indication of an even NIRF signal, with some uptake into the liver. This is in line with published material using these iTSL’s, which indicated that in the absence of intervention, in their case HIFU, the expected distribution was accumulation in the liver with some minimal uptake into the tumour.[202]

Comparing this to the ‘iTSL + MWHT’ group, a distinct difference in distribution is observed. Dorsal images at the 4 h timepoint indicate notable accumulation in the tumour, and some uptake to the liver can be observed through the ventral images. This trend is similar for the ‘iTSL + Ferrites + MWHT’ group, with the tumour appearing slightly brighter. This is not however a quantitative measure, and comparison between the groups with regard to uptake will be reserved for a later experiment. These observations mirror the those with applied HIFU [202], where study groups with applied hyperthermia to the tumour area showed a notable increase in accumulation to this region.

In conclusion, a notable alteration in biodistribution is observed upon application of 10 minutes of MWHT both in the presence and absence of PSMA-coated zinc ferrites. This is an encouraging result, and an uptake study using downstream quantitative analysis will provide further insight into the differences in uptake between groups.

5.3.5 Impact of applied MWHT on in vivo *uptake of iTSLs*

This study aimed to determine the impact of applying MWHT and PSMA-coated zinc ferrite nanoparticles on the uptake of iTSLs into flank tumours. Results of the previously described biodistribution indicated a difference in tumour uptake of iTSLs dependant on application of MWHT. Therefore, a quantitative study was required to determine uptake differences between groups. The experimental design is as described in the biodistribution study, with full details of *in vivo* methodology can be found in Materials and Methods. Briefly, athymic nude mice were inoculated with MDA-MB-231 triple negative breast cancer cells to form single dorsal xenograft tumours. Excepting the no treatment control group, appropriate intervention was applied with any from a combination of: iTSL tail vein injection, intra-tumoural ferrite injection, application of MWHT for 10 minutes at approximately 42 °C. Temperature monitoring was conducted using thermal camera images at regular time intervals. Animals were humanely culled at the 4-hour timepoint post-injection, and the tumours excised for downstream analysis. Each study group contained 3 mice with groups randomly assigned as follows: iTSL only; iTSL + MWHT; iTSL + Ferrites + MWHT. Excised tumours from all groups were digested in a 3:1 ratio of HNO_3 and H_2O_2 respectively at 70 °C. Digested tumours were analysed using ICP-MS to determine gadolinium content, and the % uptake determined relative to the injected dose.

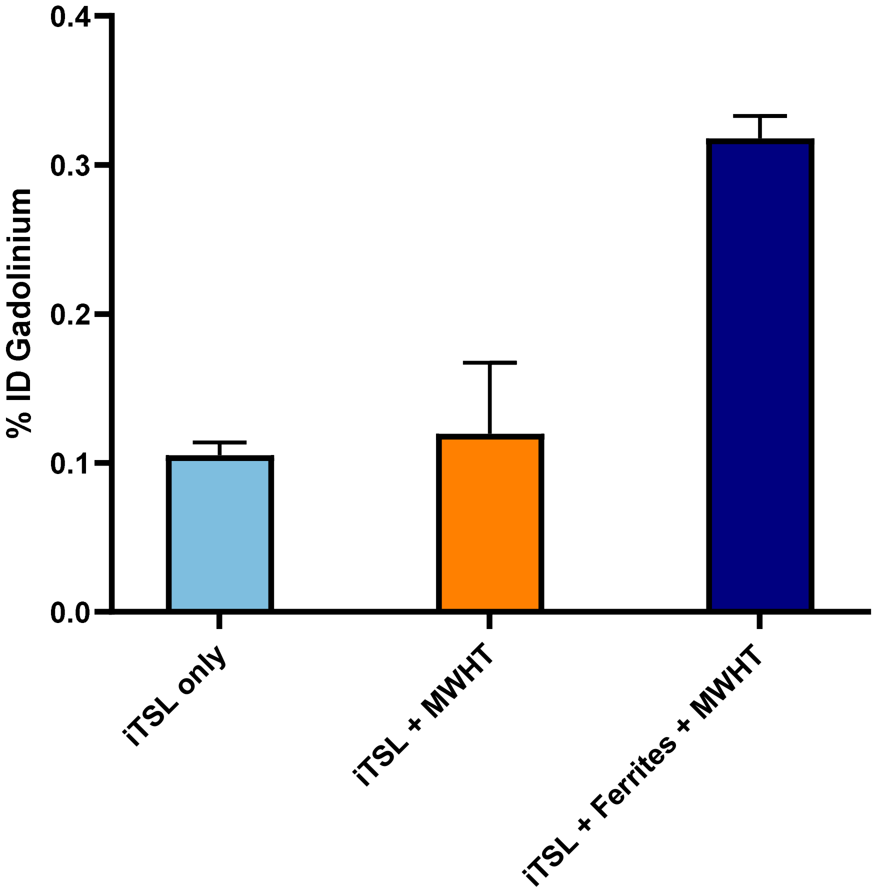

Figure 62 - Determined *in vivo* tumour uptake of iTSLs by gadolinium content. Groups depicted are as follows: iTSL only; iTSL + MWHT; iTSL + Ferrites + MWHT. Uptake shown 4 h post-injection, with quantification determined by ICP-MS.

As can be seen in Figure 62, a significant ($p<0.05$) difference is seen in uptake of gadolinium relative to injected dose in the iTSL + Ferrites + MWHT group when compared with the iTSL only group. The difference seen is approximately 3-fold, marking a significant increase in uptake. Interestingly the difference between iTSL only and iTSL + MWHT groups is not significant ($p>0.05$), however we can see that there was greater variation in this group reflected in the higher standard deviation seen.

5.3.6 Efficacy of MWHT system in conjunction with nanoparticles in vivo *using a triple negative breast cancer model*

In vivo treatment efficacy using MWHT hyperthermia in conjunction with two types of nanoparticles was conducted. Athymic nude mice with xenograft triple-negative breast cancer (MDA-MB-231) tumours were randomly allocated to five study groups. Three control groups were used: a growth control, free drug control and iTSLs without MWHT. Mice in the free drug group had intravenous infusion of PBS, free carboplatin + irinotecan (10 mg/kg). According to study group, tumour-bearing mice were administered therapeutic intervention. iTSLs (10 mg/kg SN-38) were delivered intravenously through tail-vein injection; ferrite nanoparticles (10 µl; 0.2 mg/mL) were injected intra-tumourally. MWHT was applied to relevant treatment groups for 10 minutes, mimicking the typical time for application of HIFU.

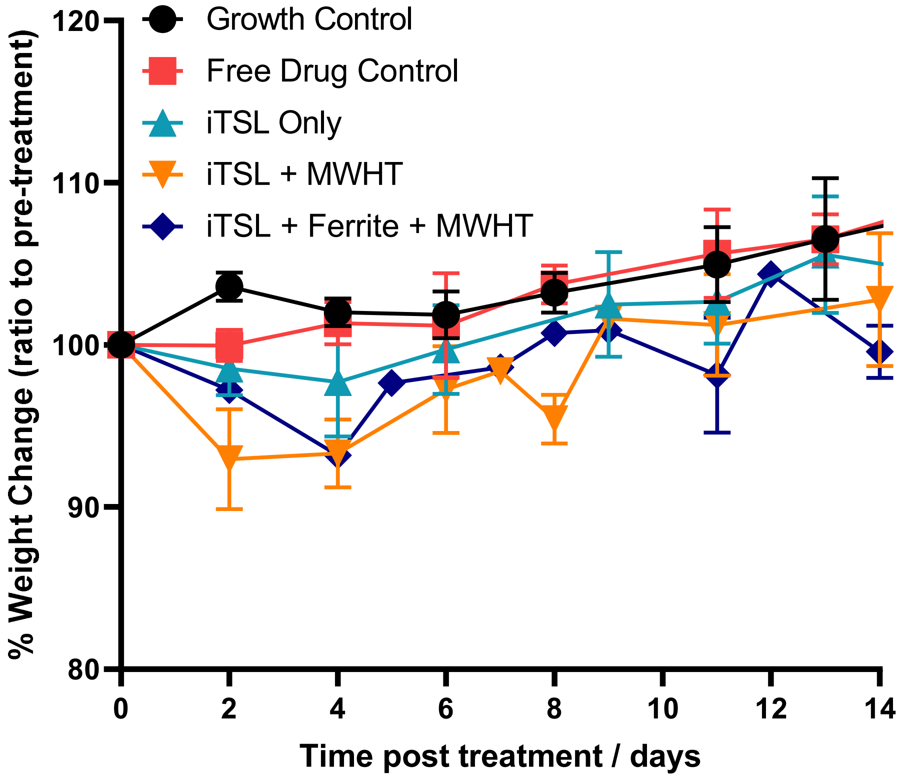

Figure 63 - % weight change of all study groups up to 14 days post-treatment. Each group represents the average of measurements taken athymic nude mice; n=4. Error bars represent +/- SD.

With any novel modality, tolerance to the intervention must be assessed, with monitoring for adverse effects or behaviours. As an indication of this, weight of all groups was measured pre-treatment and subsequently every 2-3 days to ensure the wellbeing of all study groups. As can be seen in Figure 63, minimal weight loss (≤10%) was observed in treatment groups. All groups with iTSL infusion appear to show slight weight-loss in the days post-treatment, however this is recovered by approximately day 9. This is extremely promising when compared with other TSL formulations. In one study, weight loss could take up to 20 days to recover in some treatment groups, with dose limited to >7 mg/kg.[204] Doses above this value were not tolerated and caused weight loss of >15% relative to pre-treatment weight.

Therapeutic efficacy post-treatment was evaluated by two methods: monitoring of tumour growth and group survival. Tumour growth was monitored alongside weight, with measurements taken by digital calliper every 2-3 days. Length and width values were measured and used to calculate tumour volume, as demonstrated in Figure 64. This is a standard measurement in accordance with the *in vivo* project licence and determines a humane end point of 12 mm tumour length in any measured direction. For the purposes of this study, survival in days was determined to be the number of days post-treatment until the tumour reached 12 mm in any direction.

$$volume = \frac{(l\ x\ w^2)}{2}$$

Figure 64 - Equation used to determine tumour volume (l = length, w = width). Here, the length represents the longest axis of the tumour. Width represents the shortest axis of the tumour.

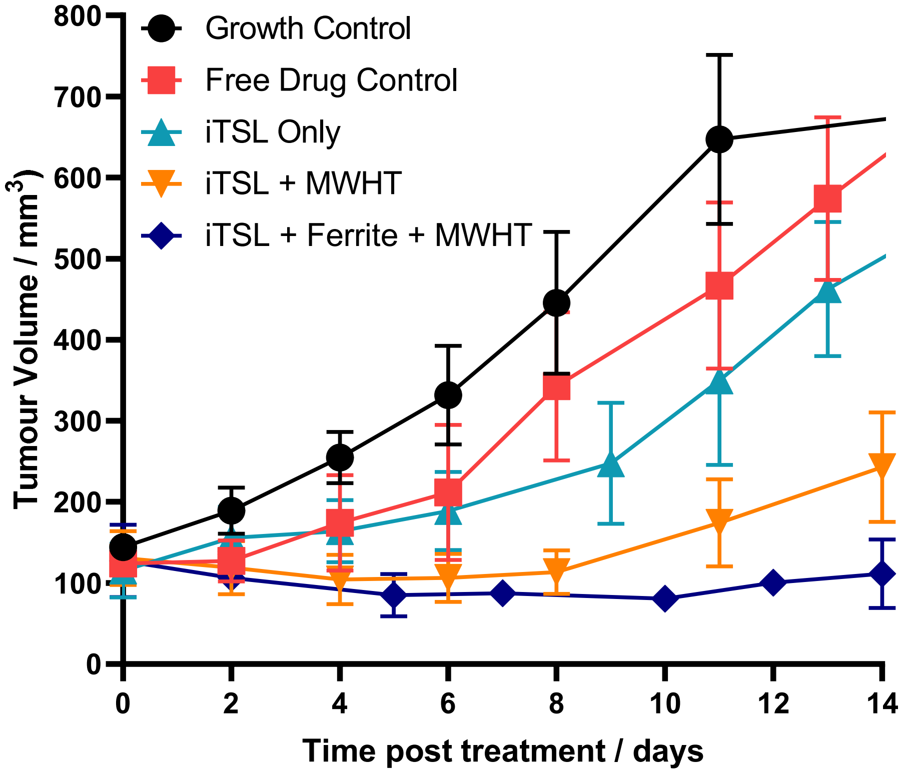

Figure 65 - Efficacy of intervention on tumour volume in all study groups. Each group represents the average of measurements athymic nude mice taken over 14 days. N=4 for all groups excepting iTSL + Ferrite + MWHT where n=3. Error bars represent +/- SD.

Measured tumour volume is noted to be lowest for the iTSL + ferrite + MWHT group, which corresponds to observations noted following the application of MWHT. A slow increase in volume is noted from approximately day 10. In the iTSL + MWHT group, a delay in volume increase is also noted, with values remaining consistent until day 8 post-treatment. When compared with other groups, all three control groups saw increases in volume from 2-4 days post treatment. Concluding this, both groups receiving MWHT showed a significant difference ($p<0.05$) relative to the growth control group, indicating the efficacious combination of iTSLs plus MWHT. In the ferrite group, observations post-treatment noted significant visible changes in the tumour consistent with ablation, despite identical MWHT parameters being used for other groups, in which this observation was not made. In one case, the tumour did not regrow at all post-treatment and so this was excluded from the tumour volume graph. This could potentially be due to the PSMA-coated zinc ferrite nanoparticles attenuating the microwave signal, causing higher temperatures in the ablative range to be reached inside the tumour. Comparing the iTSL + MWHT group to the published mirror study using HIFU [202], measured tumour volumes show an interesting finding. Our study shows an average tumour volume of approximately 240 mm^3 at 14 days for this group. The HIFU study however puts the 14-day tumour volume value at ~100 mm^3 for their 'iTSL + HIFU' group, indicating MWHT alone does not provide comparable tumour growth suppression when compared to HIFU. However, this value does closely match that of the iTSL + Ferrite + MWHT group, which had an average tumour volume of 111 mm^3 at day 14 post-treatment, highlighting the potential of companion nanoparticles to bring the MWHT technology in line with more established modalities.

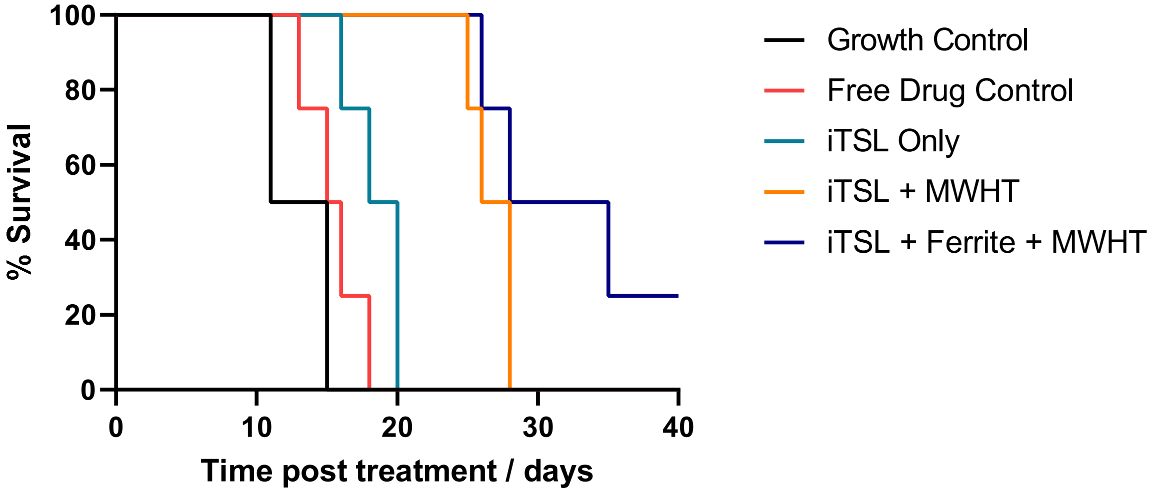

Figure 66 - Kaplan-Meier graph showing survival trend for *in* vivo treatment groups. Each group represents the average survival of athymic nude mice with single subcutaneous triple-negative breast cancer tumours induced using MDA-MB-231; n=4.

As is demonstrated in Figure 66, all tested groups showed improvement on the survival of the growth control group (15 days). Notable increase in survival times was observed in both iTSL + MWHT and iTSL + Ferrite + MWHT groups. Mentioned previously was the case of complete tumour removal observed in one mouse. This is reflected in the Kaplan-Meier graph and shows the mouse survived past the conclusion of the study at 40 days, as the tumour did not reform. As earlier discussed, this is hypothesised to be due to ablative temperatures reached inside the tumour. As with tumour volume, the control data set is comparable to the published study using HIFU. [202] Similar observations are also made with survivability, with published data showing survivability of up to 35 days post-treatment with iTSLs + HIFU. For iTSL + MWHT this value was up to 28 days and for iTSL + Ferrite + MWHT this value was over 40 days (or 35 days if the mouse with complete tumour removal is not considered. Again, we see the trend therefore that the addition of the ferrite nanoparticle injection was required to see equitable values to those seen with HIFU.

5.4 Conclusions

In conclusion, successful *in vivo* application of the lab MWHT setup in conjunction with nanoparticles was demonstrated. *In vivo* biodistribution showed accumulation of iTSLs in tumours following application of MWHT, indicating the capability of MWHT to be used with thermosensitive therapeutics. Tumour uptake quantified by ICP-MS further supported the findings of the biodistribution images, notably showing a significant increase in gadolinium content in tumours relative to injected dose in the group receiving 10 minutes of MWHT alongside iTSL IV injection and intra-tumoural injection of PSMA-coated zinc ferrites. Monitoring of tumour volume and survivability post-treatment substantiated this impact, with both groups receiving MWHT in conjunction with treatments showing a slowed tumour growth curve post-treatment. The treatment was also tolerated well with ≤10% weight loss observed in all groups. Finally, longer survival of up to 2.5-fold vs the growth control group was noted, marking a significant change. This again, strongly indicated that successful treatment was triggered by MWHT. Overall, these data reinforce the growing potential of MWHT systems to be used in combination with nanoparticles for therapeutics.

6: Summary & Future Work

In conclusion, the aim of this project was to explore microwave sensitive nanomaterials in combination with microwave imaging/sensing and hyperthermia systems. As an emerging modality, microwave offers the potential of low-cost and even portable systems for both imaging and hyperthermia that does not use ionising radiation. Addressing issues of penetration depth and sensitivity will be key to realising the full potential of microwave modalities. In this regard, the opportunity should not be missed to co-develop nanomaterials as companions to these emerging systems. Therefore, in this project, microwave sensitive nanomaterials were developed and tested for both imaging/sensing and hyperthermia purposes.

Chapter 2 explores the synthesis and characterisation of polymer-coated zinc ferrite nanoparticles. Three different zinc input ratios are explored, as well as two different polymer coatings. Synthesised nanoparticles were assessed for their dielectric properties in water and 60% glycerol phantoms. From these results a candidate formulation was selected for further exploration *ex vivo* and *in vivo*. Selected formulation was further assessed for stability and using TEM. Further work in this area could explore alternative polymer coatings and alternative metal compositions.

The focus of Chapter 3 is the establishment of living model systems for MW sensing and shows progression from cells through to *ex vivo* tissues and tumours and finally *in vivo* tumours. *Ex vivo* data demonstrated the reproducibility of measurements taken using the open-ended coaxial probe technique in conjunction with a slim-form probe and two-port VNA. Measurements of skin, fat, liver and muscle demonstrated distinct signatures when assessed for their dielectric properties. It was also shown that fat sampled in close proximity to the tumour area showed a different profile to abdominal fat. Later experiments in this chapter used PSMA-coated zinc ferrites directly injected into *ex vivo* and *in vivo* tumours, highlighting the observed change in dielectric properties post-injection and the longevity of this change.

In Chapter 4 we demonstrate the development of an R&D microwave hyperthermia system, illustrating the depth and profiles of heating and identifying suitable parameters to translate the system *in vivo*. Phantom experiments demonstrated the heating and cooling profiles of the antenna, as well as the heating depth achieved. A study in water also highlights the potential of PSMA-coated zinc ferrite nanoparticles as MWHT enhancers, showing the increased rate of heating in solution in their presence. This chapter concludes with the translation of the lab MWHT setup *in vivo*, demonstrating the capability of the setup to selectively heat tumours in a xenograft mouse tumour model. These data provide the foundation for progression to larger scale *in vivo* efficacy experiments using this setup.

In vivo experiments conducted in Chapter 5 explore the efficacy of nanoparticles in conjunction with MWHT. Specifically, PSMA-coated zinc ferrite nanoparticles and drug-loaded thermosensitive liposomes were tested in a triple negative breast cancer model. Uptake and biodistribution results demonstrate increased accumulation of thermosensitive liposomes in the tumour area following application of MWHT. Further to this, survival relative to control groups was significantly increased in both groups receiving MWHT. Particularly notable was the iTSL + ferrites + MWHT group which showed more than a 2.5-fold increase in survival relative to the growth control group. Overall, these data suggest the efficacy of MWHT systems in conjunction with nanoparticles. Further work could explore combinations with other thermosensitive formulations and extensively characterise the behaviour of polymer-coated zinc ferrite nanoparticle sin response to MWHT.

In summary, this research presents companion nanoparticles for microwave imaging/sensing and hyperthermia from synthesis through to *in vivo* translation.

7: Materials & Methods

7.1 MW imaging/sensing setup

Dielectric properties were measured using the P5023A Keysight Streamline USB Vector Network Analyzer. This is a portable vector network analyser (VNA) suitable for measurements up to 14 GHz. N1501A Dielectric probe kit (Keysight technologies Ltd, 10.0MHz-50.0GHz, slim-form probe, short), 85070E dielectric estimation software (Agilent - Keysight technologies Ltd), N1500A-004 Materials Measurement Suite (Keysight technologies Ltd, coaxial probe method). Before each use, the slim-form probe was calibrated using three known dielectric materials; air, short block (conductive elastomer that mimics electrical properties of metal), and diH$_2$o. The frequencies for each experiment are reflect alongside the relevant data but are typically 0.5-4 GHz. The slim form coaxial probe operates between 0.5-50 GHz and needs a minimum of 5.0 mm sample depth for measurements. The network analyser measures the reflection coefficient of the material under test, not its dielectric constant. The software, through a model, translates the reflection coefficient to complex dielectric constant values, which captures the permittivity and conductivity of the material.

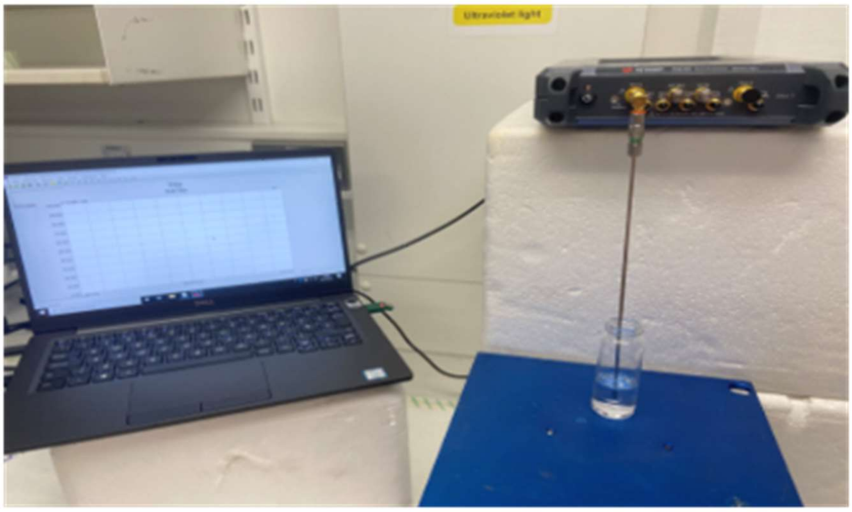

Figure 67 – Representative image of co-axial probe/VNA setup used for dielectric measurements. Photograph shows the Keysight two-port VNA system connected to the slim form co-axial probe, which is immersed in the sample. Measurements are taken using the corresponding software on the connected laptop.

7.2 MWHT setup

MWHT was conducted using a custom laboratory setup, not available as a full commercial entity. A 2.5 mm OD monopole antenna was provided by the Prakash group based in Kansas State University.[105,188,189,194] This is a directional antenna designed for *in vivo* hyperthermia and ablation studies, with continuous water flow. The MWHT setup (please see Figure 68) incorporated the following elements: amplifier (NuWaves 12B01A-D30); signal generator (AnaPico APSIN4010HC); power supply (Tenma 72-8695); peristaltic pump (Verderflex Economy EV045) and heat sink (NuPower PA Fan-Cooled Heatsink). Full details of parameters and setting for individual experiments are specified alongside data. In phantoms, temperature was monitored using the Pico Technology USB TC-08 Temperature Data Logger in conjunction with type K thermocouples (RS PRO). Temperature monitoring was conducted using a thermal camera (Teledyne FLIR LLC) for *in vivo* studies.

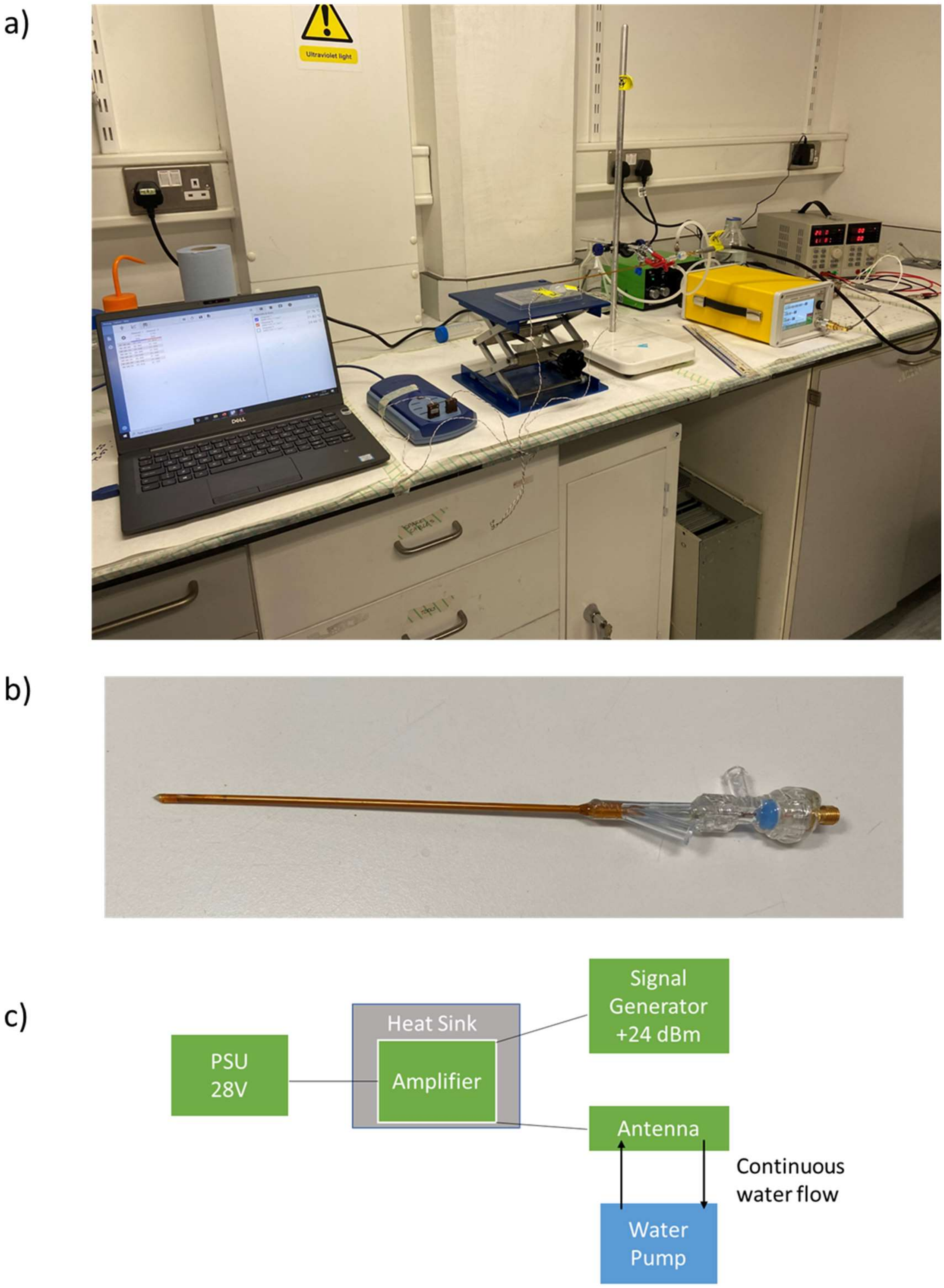

Figure 68 – Details of the lab MWHT setup used for experiments. Panels show a) photograph of MWHT setup during a phantom experiment; b) a photograph of the 2.5 mm OD antenna provided by the Prakash group; c) a diagram of the MWHT setup.

7.3 Phantom preparation

7.3.1 Glycerol phantoms

60 mL glycerol (G7757, Sigma-Aldrich) and 40 mL diH$_2$O were added to beaker and continuously stirred using a magnetic stirrer bar for a period of 1 hour before immediate use. For nanoparticle experiments, nanoparticles were added to a concentration of 10% (v/v) before stirring step.

7.3.2 MWHT agar phantoms

250 mL diH$_2$0 and 5 g agarose (UltraPure Invitrogen™ 16500500) were added to a beaker and heated using a hot plate to a temperature of 80 °C while continuously stirring with a magnetic bar. Once homogenous, heating element was disabled, and solution allowed to cool slightly while stirring. Before set, 10 mL was poured into cylindrical moulds and allowed to set for 1 hour.

7.3.3 MWHT tumour mimic phantoms

Tumour phantoms prepared according to a method from literature (ref [29]) Briefly, 18 mL ethanol (Merck, 51976), 30 mL diH$_2$0 and 0.3 g NaCl (Merck, S9888) were added to a beaker and heated using a hot plate to a temperature of 80 °C while continuously stirring with a magnetic bar. Once this temperature was reached, 0.3 g agarose (UltraPure Invitrogen™ 16500500) was added while stirring. Once homogenous, heating element was disabled, and solution allowed to cool slightly while stirring. Before set, 6mL was poured into semi-spherical moulds and allowed to set for 1 hour.

7.4 Nanoparticle preparation & characterisation

7.4.1 Synthesis of zinc ferrite nanoparticles

$Zn(acac)_2$ (varying concentrations dependant on composition: 0.33, 0.67, 1.00 mmol; 132306 Sigma Aldrich) and 1.5 mmol of $Fe(acac)_3$ (F300, Signma-Aldrich) were added 2.11 mL of oleic acid (O1383, Sigma Aldrich) 2.82 mL of oleylamine (Acros Organics, 12954) and 20 mL of benzyl ether. The mixture was stirred and heated to 200 °C for 1 hour and 250 °C for 1 hour under nitrogen. After cooling to room temperature, the mixture was aliquoted with 80 mL of ethanol, and was centrifuged for 30 minutes at 4000 RPM. The supernatant was discarded and 20 mL of hexane, and 50 µL of oleic acid and oleylamine were added to re-suspend the pellets. The suspension was centrifuged, and the pellet was discarded. Another 20 mL of Ethanol was then added to this mixture followed by a further 4000 RPM centrifuge for 30 minutes. The supernatant was then discarded, and the remaining pellet was left to dry under vacuum overnight.

7.4.2 Functionalisation of zinc ferrite nanoparticles with PMAO/PSMA

Zinc ferrite nanoparticles were functionalised using a method adapted from ref [149].

25 mg PMAO or 20 mg PSMA and 2 mg zinc ferrite nanoparticles were dissolved in 10 mL chloroform and tumbled for 1 hour at room temperature. 20 mL of diH_20 mixed with 200 µL of ethanolamine was added to the flask and tumbled for a further 30 minutes at room temperature. Chloroform was removed by rotary evaporation. 3 mL fresh chloroform was added and tumbled for 1 hour at room temperature. Sample centrifuged at 3000 RPM for 5 minutes to separate the chloroform. Aqueous phase passed through 0.2 µM syringe filter. Particles were washed 3x using centrifugal filter units (Amicon® Ultra-15) at 5000 RPM for 3 minutes. Particles were then resuspended in an appropriate amount of diH_20 according to the desired concentration. Where necessary, nanoparticles were further concentrated using centrifugal filter units (Amicon® Ultra-15) at 5000 RPM for 3 minutes. ICP-OES was used to determine iron and zinc content for each batch. For this, 250µL of polymerised nanoparticles in diH20 were digested in 17.5% HNO_3 overnight at 70 °C; Yttrium was used as a reference standard.

7.4.3 Functionalisation of zinc ferrite nanoparticles with PEDOT:PSS

2 mg zinc ferrite nanoparticles were dissolved in 1 mL chloroform via brief sonication. 20 mL of diH_20 was added on top to produce a biphasic solution. 200 µl of PEDOT:PSS (Poly(3,4-ethylenedioxythiophene)-poly(styrenesulfonate); 3.0-4.0% in H_2O, Sigma 655201) was added. Sonicate for 1 hour at room temperature. Chloroform was removed by rotary evaporation. Pellet centrifuge for 5 minutes at 5000 RPM. Resuspend pellet in 2 mL diH_20. Sonicate for a further 30 minutes. Aqueous phase passed through 0.2 µM syringe filter. Particles were then resuspended in an appropriate amount of diH_20 according to the desired concentration.

7.4.4 Thermosensitive liposomes

Thermosensitive liposomes were prepared using the method directly from ref [202] as follows:

Gadolinium (III) 2-(4,7-bis-carboxymethyl-10-[(N, N-distearylamidomethyl-N'-amidomethyl]-1,4,7,10-tetraazacyclododec-1-yl) acetic acid (Gd.DOTA.DSA; MR-labelled lipid) and CW800.DSA (Ex 775 nm, Em 795-850 nm) were synthesised and purified.

1,2-Dipalmitoyl-sn-glycero-3-phosphocholine (DPPC; 16:0 PC), 1,2-distearoyl-sn-glycero-3-phosphocholine (DSPC; 18:0 PC), 1-stearoyl-sn-glycero-3-phosphocholine (MSPC; 18:0 lyso-PC) and (ω-methoxy-polyethyleneglycol2000)-N-carboxy-1,2-distearoyl-sn-glycero-3-phosphoethanolamine (DSPE–PEG2000) were purchased from Avanti Polar Lipids (AL, USA) or Sigma Aldrich (MO, USA). All lipids were stored at −20 °C as aliquots of 10–20 mg/mL in chloroform, methanol or methanol:chloroform 1:1 (v/v) according to their solubility, while SN-38 (0.5 mg/mL) was stored in methanol:chloroform 1:1 (v/v). The standard buffers were sterile 20 mM HEPES, 5% (w/v) d-glucose corrected to pH 5.0 or 7.4 with HCl. Liposomes were prepared from Gd.DOTA.DSA/DPPC/DSPC/MSPC/PEG2000-DSPE/ CW800.DSA at 30/53.95/5/5/6/0.05 mol%. Lipid stocks were combined in a round bottom flask to a total lipid mass of 45 mg and SN-38 (0–5% w/w) was added. The solvent was slowly evaporated in vacuo to ensure thin film formation. This was hydrated in pH 5.0 buffer (1.5 mL) containing carboplatin (0–15 mg/mL) and film was fragmented by

×10 freeze-thaw cycles. The resulting suspension was sonicated at 60 °C for sufficient time to form a homogeneous, opalescent suspension of liposomes. This iTSL-SM/CC was then purified by dialysis, twice sequentially against fresh pH 5.0 buffer at ×800 vol ratio. Batches were stored at ~5 °C and appeared visually stable for at least 1 month.

7.4.5 Dynamic Light Scattering (DLS)

Zinc ferrite batches were routinely assessed using a Nanoseries Nano ZS (Malvern Panalytical, UK). Samples were diluted 1:20 (v/v) using diH20 at 25 °C and size modelling used default solute and particle parameters. To assess long-term stability, the size and PDI of the nanoparticles was tracked over 30 days. The nanoparticles were stored at room temperature, aliquots of 50 µL were removed every 10 days and diluted 1:20 v/v into diH$_2$0 at 25 °C before DLS measurements.

7.5 Cell studies

7.5.1 Cell culture

A human mammary epithelial cell line (MDA-MB-231) was maintained in Dulbecco's Modified Eagle Media (DMEM) supplemented with 10 v% FBS and 1 v% penicillin-streptomycin (stock 5 kU/mL each). The cells were grown at 37 °C in a humidified atmosphere containing 5 v% CO2. The cells were passaged approximately every 2-3 days once they had reached ~90 % confluent.

7.5.2 Dielectric characterization of cells in suspension

MDA-MB-231 cells were grown as detailed above until confluent. Cells were detached, pelleted, and resuspended at a concentration of 1 x 10^6 cells per ml in supplemented DMEM, HBSS or PBS. Dielectric measurements were conducted using the open-ended co-axial probe technique using a slim-form probe over a frequency range of 0.5-4 GHz.

7.5.3 Dielectric characterization of cell monolayer

MDA-MB-231 cells were grown as detailed above until confluent. Cells were seeded on 6-well and 12-well tissue culture plates and allowed to adhere for a period of 24 hours. Following incubation, cells were washed 3 times with PBS and an appropriate amount of DMEM readded to each well. Dielectric measurements used a SPEAG DAK 1.2E open-ended co-axial probe over a frequency range of 5 GHz - 8 GHz. Experiments were performed in triplicate, and a total of 10 measurements were taken per well and an average calculated.

7.5.4 Dielectric characterization of cell pellet

MDA-MB-231 cells were grown as detailed above until confluent. Cells were counted and approximately 60 million cells were detached and pelleted. Cell pellet was washed 3 times with PBS. Dielectric measurements were conducted using the open-ended co-axial probe technique a slim-form probe over a frequency range of 0.5-4 GHz.

7.6 *Ex vivo* and *in vivo* experiments

7.6.1 Animal studies

All animal procedures were conducted under the U.K. Home Office regulations and the Guidance for the Operation of Animals (Scientific Procedures) Act (1986). Female 4−6-week-old athymic nude mice were sourced from Envigo (Huntingdon, UK).

7.6.2 Tumour induction

MDA-MB-231 cells (6×10^6 per tumour) were suspended in PBS and then mixed 1:1 (v/v) with Geltrex Matrix (ThermoFisher). This was injected subcutaneously to induce bilateral tumours on the dorsal haunch of each mouse. Tumour size was monitored using a digital calliper.

7.6.3 Ex vivo *dielectric characterisation of tumours and tissues*

At a predetermined endpoint (either 12 mm tumour longest axis, or for 2 weeks post-induction) mice were euthanised and dissected. Dissected tumours and tissues (including muscle, skin, fat and the liver) were measured using the slim-form open-ended co-axial probe method. 10 measurements were taken at the same probe position and an average calculated. For tumour measurements with PSMA-coated zinc ferrite nanoparticles suspension (0.06 mg/mL; 10 µl) was injected directly into the excised tumour. For control tumours, 10 µl of diH20 was injected in the same manner. Post-injection, 10 measurements were subsequently taken at the same probe position and an average calculated.

7.6.4 In vivo *dielectric characterisation of tumours*

2 weeks post induction, mice bearing MDA-MB-231 tumours were placed under anaesthesia. Tumours were measured using the slim form open-ended co-axial probe method placed on the skin at the site of the tumour. 10 measurements were taken at the same probe position and an average calculated. For tumour measurements with PSMA-coated zinc ferrite nanoparticles, (0.2 mg/mL; 10 µl) suspension was injected directly into the excised tumour. 10 measurements were taken at the same probe position and an average calculated. Subsequent measurements at 1h, 2h and 4h timepoints were taken in the same fashion.

7.6.5 In vivo *MWHT*

Athymic nude mice bearing MDA-MB-231 tumours were prepared to receive MWHT. MWHT equipment is as previously detailed, with power set to 24 dBm at a frequency of 2.45 GHz. Water flow from the peristaltic pump was at 18 mL/min with room temperature water. The flank tumour was covered with degassed, pre-warmed ultrasound gel (~35 °C). The MWHT antenna was placed approximately 1-2 mm from the tumour surface, with the ultrasound gel providing a buffer. This distance was selected to reduce the risk of burns or ablative temperatures. Ultrasound gel was used as heat transfer through air could prove ineffective. Each MWHT treatment was applied for a total time of 10 minutes, with the goal of reaching a temperature of 42.0 °C. Power settings were not adjusted during the period of application. Temperature monitoring was conducted using a thermal camera (Teledyne FLIR LLC).

7.6.6 In vivo *biodistribution*

Athymic nude mice bearing MDA-MB-231 tumours were randomly allocated into three groups (n = 3): iTSL only, iTSL + MWHT; iTSL + Ferrites + MWHT. For iTSL infusion, all mice were placed under anaesthesia using isoflurane gas, iTSL (10 mg/kg) were injected iv via the tail vein. Intra-tumoural injection of PSMA-coated zinc ferrite nanoparticles (10 µl; 0.2 mg/mL) in relevant groups was conducted immediately following iTSL infusion. MWHT for relevant groups as applied for a period of 10 minutes with the goal of reaching a temperature of 42.0 °C. The distribution was monitored using an *in vivo* multispectral imaging system (Maestro EX, PerkinElmer, Waltham, MA, USA). Images were collected at time 0, 2, 4, 24 h post treatment. iTSL distribution images were acquired using the NIR filters set to track the NIRF lipid-conjugate dye (CW800.DSA, Ex 775 nm, Em 795-850 nm).

7.6.7 In vivo *uptake*

Athymic nude mice bearing MDA-MB-231 tumours were randomly allocated into three groups (n = 3): iTSL only, iTSL + MWHT; iTSL + Ferrites + MWHT. For iTSL infusion, all mice were placed under anaesthesia using isoflurane gas, iTSL (10 mg/kg) were injected iv via the tail vein. Intra-tumoural injection of PSMA-coated zinc ferrite nanoparticles (10 µl; 0.2 mg/mL) in relevant groups was conducted immediately following iTSL infusion. MWHT for relevant groups as applied for a period of 10 minutes with the goal of reaching a temperature of 42.0 °C. After 4 h post injection all mice were humanely euthanized, and the tumour excised. The excised tumour was weighed and then digested using HNO_3 (150 µL) and H_2O_2 (50 µL) at 70 °C overnight. The digested sample was diluted to a final volume of 10 mL ultrapure water and the gadolinium concentration analysed using ICP-MS (PerkinElmer NexION 350D). Final concentrations Gd-lipids are given after correction for dilution effects during sample preparation. To estimate the % injected dose (ID), the concentrations were normalised against tumour weight and compared to the injected concentration of iTSLs.

7.6.8 In vivo *efficacy*

Athymic nude mice bearing MDA-MB-231 tumours were randomly allocated into five groups (n = 4). One group was used as a growth control and received no treatment. The further four groups were treated as follows: 'free drug control' irinotecan + carboplatin (10 mg/kg); iTSL only, iTSL + MWHT; iTSL + Ferrites + MWHT. Following treatment, animals were maintained and monitored through regular weight checks and tumour volume measurements by digital calliper every 2/3 days. A predetermined humane end point of 12 mm tumour length in any direction was followed in accordance with the project licence. At the end of the experiment all mice were humanely euthanized.

8: Appendices

8.1 Chapter 3

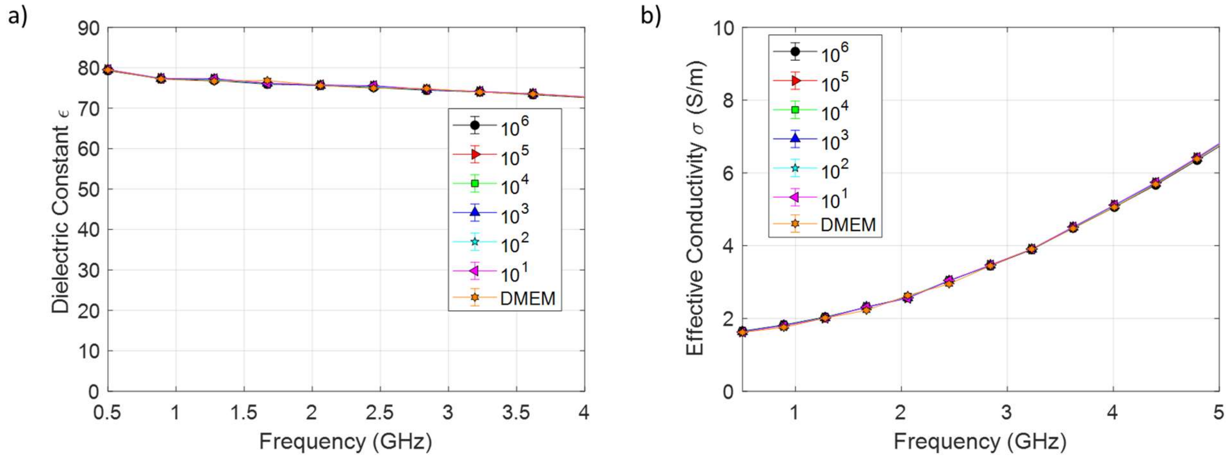

Figure 69 - Characterisation of MDA-MB-231 cells using the open-ended co-axial probe technique and a slim-form probe. Triple-negative breast cancer cell line MDA-MB-231 was suspended in 5 mL of DMEM at varying concentrations. 10^x represents number of cells per mL. Graphs depict measured properties over a frequency range of 0.5-4 GHz and are shown in the panels as a) dielectric constant and b) effective conductivity. (n=3)

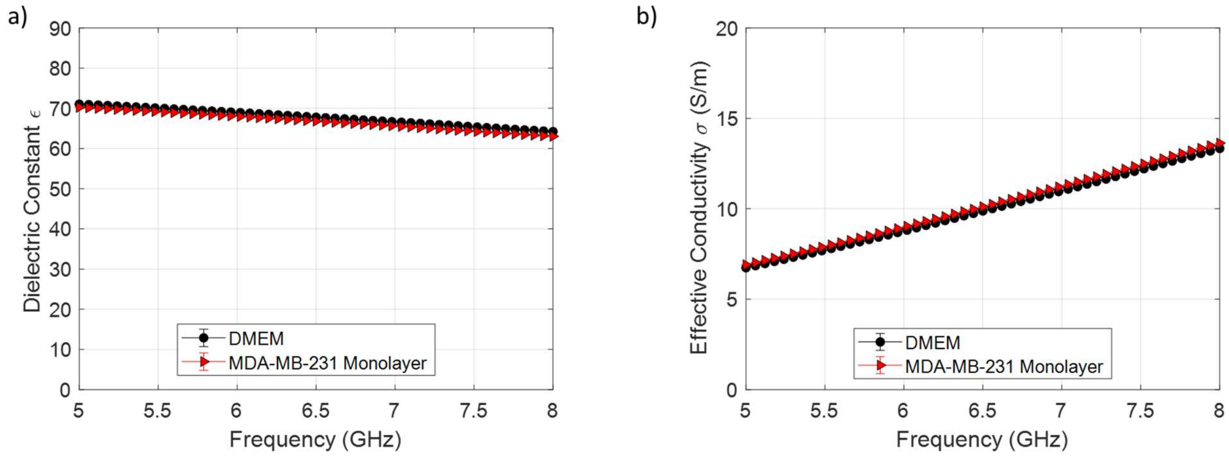

Figure 70 - Characterisation of cell monolayer using DAK 1.2E probe. Triple-negative breast cancer cell line MDA-MB-231 allowed to form a monolayer on a 12-well plate at a seeding density of 500k cells per well. Graphs depict measured properties over a frequency range of 5-8 GHz and are shown in the panels as: a) dielectric constant and b) effective conductivity. Measured properties of DMEM are shown as a comparison. (n=3)

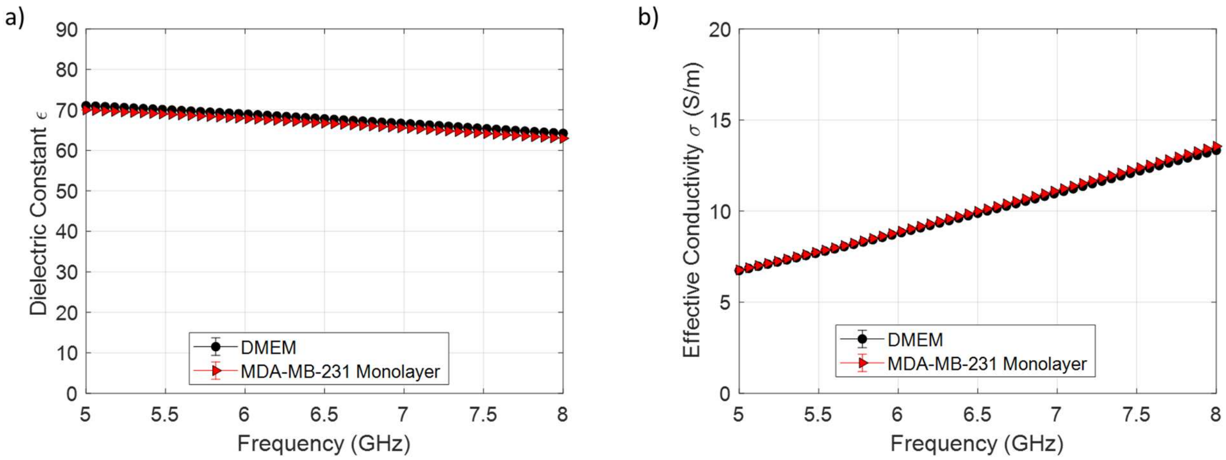

Figure 71 - Characterisation of cell monolayer using DAK 1.2E probe. Triple-negative breast cancer cell line MDA-MB-231 allowed to form a monolayer on a 6-well plate at a seeding density of 500k cells per well. Graphs depict measured properties over a frequency range of 5-8 GHz and are shown in the panels as: a) dielectric constant and b) effective conductivity. Measured properties of DMEM are shown as a comparison. (n=3)

9: References

1. Wilhelm, S. *et al.* Analysis of nanoparticle delivery to tumours. *Nat Rev Mater* **1**, 16014 (2016).

2. Ouyang, B. *et al.* The dose threshold for nanoparticle tumour delivery. *Nat Mater* 1–10 (2020) doi:10.1038/s41563-020-0755-z.

3. Wang, M. & Thanou, M. Targeting nanoparticles to cancer. *Pharmacol Res* **62**, (2010).

4. Sykes, E. A. *et al.* Tailoring nanoparticle designs to target cancer based on tumor pathophysiology. *Proceedings of the National Academy of Sciences* **113**, (2016).

5. Yoo, J., Park, C., Yi, G., Lee, D. & Koo, H. Active Targeting Strategies Using Biological Ligands for Nanoparticle Drug Delivery Systems. *Cancers (Basel)* **11**, (2019).

6. Golombek, S. K. *et al.* Tumor targeting via EPR: Strategies to enhance patient responses. *Adv Drug Deliv Rev* **130**, (2018).

7. Oliveira, B. L. *et al.* Microwave Breast Imaging: experimental tumour phantoms for the evaluation of new breast cancer diagnosis systems. *Biomed Phys Eng Express* **4**, 025036 (2018).

8. Joachimowicz, N., Duchêne, B., Conessa, C. & Meyer, O. Anthropomorphic Breast and Head Phantoms for Microwave Imaging. *Diagnostics* **8**, 85 (2018).

9. Meaney, P. M., Fox, C. J., Geimer, S. D. & Paulsen, K. D. Electrical Characterization of Glycerin: Water Mixtures: Implications for Use as a Coupling Medium in Microwave Tomography. *IEEE Trans Microw Theory Tech* **65**, 1471–1478 (2017).

10. Joachimowicz, N., Conessa, C., Henriksson, T. & Duchene, B. Breast Phantoms for Microwave Imaging. *IEEE Antennas Wirel Propag Lett* **13**, 1333–1336 (2014).

11. White, J. *et al.* Male breast carcinoma: increased awareness needed. *Breast Cancer Research* **13**, 219 (2011).

12. Siegel, R. L., Miller, K. D., Wagle, N. S. & Jemal, A. Cancer statistics, 2023. *CA Cancer J Clin* **73**, 17–48 (2023).

13. Lei, S. *et al.* Global patterns of breast cancer incidence and mortality: A population-based cancer registry data analysis from 2000 to 2020. *Cancer Commun* **41**, 1183–1194 (2021).

14. Rosen, R. D. & Sapra, A. *TNM Classification*. (2023).

15. Yin, L., Duan, J.-J., Bian, X.-W. & Yu, S. Triple-negative breast cancer molecular subtyping and treatment progress. *Breast Cancer Research* **22**, 61 (2020).

16. Abdulkareem, I. & Zurmi, I. Review of hormonal treatment of breast cancer. *Niger J Clin Pract* **15**, 9 (2012).

17. Griffiths, C. L. & Olin, J. L. Triple Negative Breast Cancer: A Brief Review of its Characteristics and Treatment Options. *J Pharm Pract* **25**, 319–323 (2012).

18. Wang, L. Early Diagnosis of Breast Cancer. *Sensors* **17**, 1572 (2017).

19. Tabár, L. *et al.* Swedish Two-County Trial: Impact of Mammographic Screening on Breast Cancer Mortality during 3 Decades. *Radiology* **260**, 658–663 (2011).

20. Rojas, K. & Stuckey, A. Breast Cancer Epidemiology and Risk Factors. *Clin Obstet Gynecol* **59**, 651–672 (2016).

21. von Euler-Chelpin, M., Lillholm, M., Vejborg, I., Nielsen, M. & Lynge, E. Sensitivity of screening mammography by density and texture: a cohort study from a population-based screening program in Denmark. *Breast Cancer Research* **21**, 111 (2019).

22. Elmore, J. G. *et al.* Ten-Year Risk of False Positive Screening Mammograms and Clinical Breast Examinations. *New England Journal of Medicine* **338**, 1089–1096 (1998).

23. Gram, I., Lund, E. & Slenker, S. Quality of life following a false positive mammogram. *Br J Cancer* **62**, 1018–1022 (1990).

24. Sood, R. *et al.* Ultrasound for Breast Cancer Detection Globally: A Systematic Review and Meta-Analysis. *J Glob Oncol* 1–17 (2019) doi:10.1200/JGO.19.00127.

25. Mann, R. M., Kuhl, C. K. & Moy, L. Contrast-enhanced MRI for breast cancer screening. *Journal of Magnetic Resonance Imaging* **50**, 377–390 (2019).

26. Preece, A. W., Craddock, I., Shere, M., Jones, L. & Winton, H. L. MARIA M4: clinical evaluation of a prototype ultrawideband radar scanner for breast cancer detection. *Journal of Medical Imaging* **3**, 033502 (2016).

27. Aldhaeebi, M. A. *et al.* Review of Microwaves Techniques for Breast Cancer Detection. *Sensors* **20**, 2390 (2020).

28. Ortega-Palacios, R., Leija, L., Vera, A. & Cepeda, M. F. J. Measurement of breast - tumor phantom dielectric properties for microwave breast cancer treatment evaluation. in *2010 7th International Conference on Electrical Engineering Computing Science and Automatic Control* 216–219 (IEEE, 2010). doi:10.1109/ICEEE.2010.5608579.

29. Semenov, S. Y. *et al.* Microwave tomography: two-dimensional system for biological imaging. *IEEE Trans Biomed Eng* **43**, 869–877 (1996).

30. Xu Li & Hagness, S. C. A confocal microwave imaging algorithm for breast cancer detection. *IEEE Microwave and Wireless Components Letters* **11**, 130–132 (2001).

31. Zhang, K., Amineh, R. K., Dong, Z. & Nadler, D. Microwave Sensing of Water Quality. *IEEE Access* **7**, 69481–69493 (2019).

32. Engman, E. T. Applications of microwave remote sensing of soil moisture for water resources and agriculture. *Remote Sens Environ* **35**, 213–226 (1991).

33. van Verre, W., Gao, X., Podd, F. J., Daniels, D. J. & Peyton, A. J. GPR Bowtie Antennas with Reduced Induction Footprints for Dual-Modality Detectors. in *2019 IEEE International Symposium on Antennas and Propagation and USNC-URSI Radio Science Meeting* 859–600 (2019). doi:10.1109/APUSNCURSINRSM.2019.8889194.

34. Soldovieri, F., Ahmad, F. & Solimene, R. Validation of Microwave Tomographic Inverse Scattering Approach via Through-the-Wall Experiments in Semicontrolled Conditions. *IEEE Geoscience and Remote Sensing Letters* **8**, 123–127 (2011).

35. Chandra, R., Zhou, H., Balasingham, I. & Narayanan, R. M. On the Opportunities and Challenges in Microwave Medical Sensing and Imaging. *IEEE Trans Biomed Eng* **62**, (2015).

36. Joines, W. T., Zhang, Y., Li, C. & Jirtle, R. L. The measured electrical properties of normal and malignant human tissues from 50 to 900 MHz. *Med Phys* **21**, (1994).

37. Semenov, S. Microwave tomography: review of the progress towards clinical applications. *Philosophical Transactions of the Royal Society A: Mathematical, Physical and Engineering Sciences* **367**, (2009).

38. O'Loughlin, D. *et al.* Microwave Breast Imaging: Clinical Advances and Remaining Challenges. *IEEE Trans Biomed Eng* **65**, 2580–2590 (2018).

39. Surowiec, A. J., Stuchly, S. S., Barr, J. R. & Swarup, A. Dielectric properties of breast carcinoma and the surrounding tissues. *IEEE Trans Biomed Eng* **35**, 257–263 (1988).

40. Campbell, A. M. & Land, D. v. Dielectric properties of female human breast tissue measured in vitro at 3.2 GHz. *Phys Med Biol* **37**, (1992).

41. Aldhaeebi, M. A. *et al.* Review of Microwaves Techniques for Breast Cancer Detection. *Sensors* **20**, (2020).

42. Aldhaeebi, M. A. *et al.* Review of Microwaves Techniques for Breast Cancer Detection. *Sensors* **20**, 2390 (2020).

43. Semenov, S. Y. & Corfield, D. R. Microwave Tomography for Brain Imaging: Feasibility Assessment for Stroke Detection. *Int J Antennas Propag* **2008**, 1–8 (2008).

44. Tobon Vasquez, J. A. *et al.* A Prototype Microwave System for 3D Brain Stroke Imaging. *Sensors* **20**, 2607 (2020).

45. Scapaticci, R., di Donato, L., Catapano, I. & Crocco, L. A FEASIBILITY STUDY ON MICROWAVE IMAGING FOR BRAIN STROKE MONITORING. *Progress In Electromagnetics Research B* **40**, 305–324 (2012).

46. Mobashsher, A. T., Mahmoud, A. & Abbosh, A. M. Portable Wideband Microwave Imaging System for Intracranial Hemorrhage Detection Using Improved Back-projection Algorithm with Model of Effective Head Permittivity. *Sci Rep* **6**, (2016).

47. Razzicchia, E. *et al.* Feasibility Study of Enhancing Microwave Brain Imaging Using Metamaterials. *Sensors* **19**, (2019).

48. Ljungqvist, J. *et al.* Clinical Evaluation of a Microwave-Based Device for Detection of Traumatic Intracranial Hemorrhage. *J Neurotrauma* **34**, 2176–2182 (2017).

49. Persson, M. *et al.* Microwave-Based Stroke Diagnosis Making Global Prehospital Thrombolytic Treatment Possible. *IEEE Trans Biomed Eng* **61**, 2806–2817 (2014).

50. Hussein, M. *et al.* Breast cancer cells exhibits specific dielectric signature in vitro using the open-ended coaxial probe technique from 200 MHz to 13.6 GHz. *Sci Rep* **9**, 4681 (2019).

51. al Ahmad, M., al Natour, Z., Mustafa, F. & Rizvi, T. A. Electrical Characterization of Normal and Cancer Cells. *IEEE Access* **6**, 25979–25986 (2018).

52. Kelleci, M., Aydogmus, H., Aslanbas, L., Erbil, S. O. & Hanay, M. S. Towards microwave imaging of cells. *Lab Chip* **18**, 463–472 (2018).

53. Lazebnik, M. *et al.* A large-scale study of the ultrawideband microwave dielectric properties of normal, benign and malignant breast tissues obtained from cancer surgeries. *Phys Med Biol* **52**, 6093–6115 (2007).

54. Lazebnik, M. *et al.* A large-scale study of the ultrawideband microwave dielectric properties of normal breast tissue obtained from reduction surgeries. *Phys Med Biol* **52**, (2007).

55. Kaye, C., Gilmore, C. & LoVetri, J. Enhanced Detection of Magnetic Nanoparticles using a Novel Microwave Ferromagnetic Resonance Imaging System. *IEEE Trans Biomed Eng* 1–1 (2020) doi:10.1109/TBME.2020.3019716.

56. Green, M. & Chen, X. Recent progress of nanomaterials for microwave absorption. *Journal of Materiomics* **5**, 503–541 (2019).

57. Chertok, B. *et al.* Iron oxide nanoparticles as a drug delivery vehicle for MRI monitored magnetic targeting of brain tumors. *Biomaterials* **29**, 487–496 (2008).

58. Ogunlade, O. & Beard, P. Exogenous contrast agents for thermoacoustic imaging: An investigation into the underlying sources of contrast. *Med Phys* **42**, 170–181 (2014).

59. Ibrahim, I. R. *et al.* A Study on Microwave Absorption Properties of Carbon Black and Ni0.6Zn0.4Fe2O4 Nanocomposites by Tuning the Matching-Absorbing Layer Structures. *Sci Rep* **10**, 3135 (2020).

60. Lahri, R. *et al.* Examination of zinc ferrites vs. iron oxides as contrast agents for microwave systems. in *13th European Conference on Antennas and Propagation, EuCAP 2019* (Institute of Electrical and Electronics Engineers Inc., 2019).

61. Lahri, R., Rahman, M., Wright, M., Kosmas, P. & Thanou, M. Zinc oxide nanoparticles as contrast-enhancing agents for microwave imaging. *Med Phys* **45**, 3820–3830 (2018).

62. Hudson, J. S. *et al.* Iron nanoparticle contrast enhanced microwave imaging for emergent stroke: A pilot study. *Journal of Clinical Neuroscience* **59**, 284–290 (2019).

63. Qin, H., Qin, B., Yuan, C., Chen, Q. & Xing, D. Pancreatic Cancer detection via Galectin-1-targeted Thermoacoustic Imaging: validation in an *in vivo* heterozygosity model. *Theranostics* **10**, 9172–9185 (2020).

64. Vázquez, E. & Prato, M. Carbon Nanotubes and Microwaves: Interactions, Responses, and Applications. *ACS Nano* **3**, 3819–3824 (2009).

65. Ebbesen, T. W. *et al.* Electrical conductivity of individual carbon nanotubes. *Nature* **382**, 54–56 (1996).

66. Zaporotskova, I. v., Boroznina, N. P., Parkhomenko, Y. N. & Kozhitov, L. v. Carbon nanotubes: Sensor properties. A review. *Modern Electronic Materials* **2**, 95–105 (2016).

67. Zoughi, R. *et al.* Microwave dielectric properties and Targeted heating of polypropylene nano-composites containing carbon nanotubes and carbon black. *Polymer (Guildf)* **179**, 121658 (2019).

68. Mashal, A. *et al.* Toward Carbon-Nanotube-Based Theranostic Agents for Microwave Detection and Treatment of Breast Cancer: Enhanced Dielectric and Heating Response of Tissue-Mimicking Materials. *IEEE Trans Biomed Eng* **57**, 1831–1834 (2010).

69. Babanzadeh, S., Mehdipour-Ataei, S. & Mahjoub, A. R. Effect of nanosilica on the dielectric properties and thermal stability of polyimide/SiO $_2$ nanohybrid. *Des Monomers Polym* **16**, 417–424 (2013).

70. Dutta, K. & De, S. K. Electrical conductivity and dielectric properties of SiO2 nanoparticles dispersed in conducting polymer matrix. *Journal of Nanoparticle Research* **9**, 631–638 (2007).

71. Chen, L., Duan, Y., Liu, L., Guo, J. & Liu, S. Influence of SiO2 fillers on microwave absorption properties of carbonyl iron/carbon black double-layer coatings. *Mater Des* **32**, 570–574 (2011).

72. Yan, L. *et al.* Enhanced microwave absorption of Fe nanoflakes after coating with SiO $_2$ nanoshell. *Nanotechnology* **21**, 095708 (2010).

73. Yuchang, Q., Wancheng, Z., Shu, J., Fa, L. & Dongmei, Z. Microwave electromagnetic property of SiO2-coated carbonyl iron particles with higher oxidation resistance. *Physica B Condens Matter* **406**, 777–780 (2011).

74. Green, M. *et al.* Doped, conductive SiO2 nanoparticles for large microwave absorption. *Light Sci Appl* **7**, 87 (2018).

75. Wada, S. *et al.* Preparation of nm-Sized Barium Titanate Fine Particles and Their Powder Dielectric Properties. *Jpn J Appl Phys* **42**, 6188–6195 (2003).

76. Wei, Y. *et al.* Dielectric and Ferroelectric Properties of BaTiO3 Nanofibers Prepared via Electrospinning. *J Mater Sci Technol* **30**, 743–747 (2014).

77. Pant, H., Patra, M., Verma, A., Vadera, S. & Kumar, N. Study of the dielectric properties of barium titanate–polymer composites. *Acta Mater* **54**, 3163–3169 (2006).

78. Tang, H., Zhou, Z. & Sodano, H. A. Relationship between $BaTiO_3$ Nanowire Aspect Ratio and the Dielectric Permittivity of Nanocomposites. *ACS Appl Mater Interfaces* **6**, 5450–5455 (2014).

79. Moharana, S., Mishra, M. K., Behera, B. & Mahaling, R. N. Enhanced dielectric properties of polyethylene glycol (PEG) modified BaTiO3 (BT)-poly(vinylidene fluoride) (PVDF) composites. *Polymer Science, Series A* **59**, 405–415 (2017).

80. Tian, L. *et al.* Effect of hydrogenation on the microwave absorption properties of $BaTiO_3$ nanoparticles. *J Mater Chem A Mater* **3**, 12550–12556 (2015).

81. Silva, A., Azough, F., Freer, R. & Leach, C. Microwave dielectric ceramics in the system BaO–Li2O–Nd2O3–TiO2. *J Eur Ceram Soc* **20**, 2727–2734 (2000).

82. Udovic, M., Valant, M. & Suvorov, D. Dielectric characterisation of ceramics from the TiO2–TeO2 system. *J Eur Ceram Soc* **21**, 1735–1738 (2001).

83. McCarthy, D. N. *et al.* Increased permittivity nanocomposite dielectrics by controlled interfacial interactions. *Compos Sci Technol* **72**, 731–736 (2012).

84. Wypych, A. *et al.* Dielectric Properties and Characterisation of Titanium Dioxide Obtained by Different Chemistry Methods. *J Nanomater* **2014**, 1–9 (2014).

85. Xia, T., Zhang, C., Oyler, N. A. & Chen, X. Hydrogenated TiO_2 Nanocrystals: A Novel Microwave Absorbing Material. *Advanced Materials* **25**, 6905–6910 (2013).

86. Dong, J. *et al.* Partially crystallized TiO_2 for microwave absorption. *J Mater Chem A Mater* **3**, 5285–5288 (2015).

87. Chen, W. & Zhang, J. Using Nanoparticles to Enable Simultaneous Radiation and Photodynamic Therapies for Cancer Treatment. *J Nanosci Nanotechnol* **6**, 1159–1166 (2006).

88. Mashal, A., Booske, J. H. & Hagness, S. C. Toward contrast-enhanced microwave-induced thermoacoustic imaging of breast cancer: an experimental study of the effects of microbubbles on simple thermoacoustic targets. *Phys Med Biol* **54**, 641–650 (2009).

89. Jha, S., Sharma, P. K. & Malviya, R. Hyperthermia: Role and Risk Factor for Cancer Treatment. *Achievements in the Life Sciences* **10**, 161–167 (2016).

90. Chicheł, A., Skowronek, J., Kubaszewska, M. & Kanikowski, M. Hyperthermia – description of a method and a review of clinical applications. *Reports of Practical Oncology & Radiotherapy* **12**, 267–275 (2007).

91. Rossmanna, C. & Haemmerich, D. Review of Temperature Dependence of Thermal Properties, Dielectric Properties, and Perfusion of Biological Tissues at Hyperthermic and Ablation Temperatures. *Crit Rev Biomed Eng* **42**, (2014).

92. Skitzki, J. J., Repasky, E. A. & Evans, S. S. Hyperthermia as an immunotherapy strategy for cancer. *Curr Opin Investig Drugs* **10**, 550–558 (2009).

93. Kok, H. P. *et al.* Heating technology for malignant tumors: a review. *International Journal of Hyperthermia* **37**, (2020).

94. Sawicki, J. F., Shea, J. D., Behdad, N. & Hagness, S. C. The impact of frequency on the performance of microwave ablation. *International Journal of Hyperthermia* **33**, (2017).

95. Yuan, H.-B. *et al.* Flexible bronchoscopy-guided microwave ablation in peripheral porcine lung: a new minimally-invasive ablation. *Transl Lung Cancer Res* **8**, (2019).

96. Kokuryo, D., Kumamoto, E. & Kuroda, K. Recent technological advancements in thermometry. *Adv Drug Deliv Rev* **163–164**, (2020).

97. Hijnen, N. M. *et al.* The magnetic susceptibility effect of gadolinium-based contrast agents on PRFS-based MR thermometry during thermal interventions. *J Ther Ultrasound* **1**, (2013).

98. Kobayashi, T. Cancer hyperthermia using magnetic nanoparticles. *Biotechnol J* **6**, 1342–1347 (2011).

99. Zhen, W., Hu, W., Dong, L., An, S. & Jiang, X. Nanomaterials for the regulation of the tumor microenvironment and theranostics. *Nanoscale Adv* **2**, 1395–1409 (2020).

100. Perlman, O., Weitz, I. S. & Azhari, H. Target visualisation and microwave hyperthermia monitoring using nanoparticle-enhanced transmission ultrasound (NETUS). *International Journal of Hyperthermia* **34**, 773–785 (2018).

101. Minbashi, M., Kordbacheh, A. A., Ghobadi, A. & Tuchin, V. v. Optimization of power used in liver cancer microwave therapy by injection of Magnetic Nanoparticles (MNPs). *Comput Biol Med* **120**, 103741 (2020).

102. Peng, H., Huang, Q., Wu, T., Wen, J. & He, H. Preparation of Porous γ-Fe2O3@mWO3 Multifunctional Nanoparticles for Drug Loading and Controlled Release. *Curr Drug Deliv* **15**, 278–285 (2018).

103. McWilliams, B. *et al.* Experimental Investigation of Magnetic Nanoparticle-Enhanced Microwave Hyperthermia. *J Funct Biomater* **8**, 21 (2017).

104. Curto, S. *et al.* An integrated platform for small-animal hyperthermia investigations under ultra-high-field MRI guidance. *International Journal of Hyperthermia* **34**, 341–351 (2018).

105. Faridi, P., Bossmann, S. H. & Prakash, P. Simulation-based design and characterization of a microwave applicator for MR-guided hyperthermia experimental studies in small animals. *Biomed Phys Eng Express* **6**, 015001 (2019).

106. Wen, F., Zhang, F. & Liu, Z. Investigation on Microwave Absorption Properties for Multiwalled Carbon Nanotubes/Fe/Co/Ni Nanopowders as Lightweight Absorbers. *The Journal of Physical Chemistry C* **115**, 14025–14030 (2011).

107. Zhu, H., Lin, H., Guo, H. & Yu, L. Microwave absorbing property of Fe-filled carbon nanotubes synthesized by a practical route. *Materials Science and Engineering: B* **138**, 101–104 (2007).

108. Zou, T., Li, H., Zhao, N. & Shi, C. Electromagnetic and microwave absorbing properties of multi-walled carbon nanotubes filled with Ni nanowire. *J Alloys Compd* **496**, L22–L24 (2010).

109. Zhang, L. & Zhu, H. Dielectric, magnetic, and microwave absorbing properties of multi-walled carbon nanotubes filled with Sm2O3 nanoparticles. *Mater Lett* **63**, 272–274 (2009).

110. Dalal, M. *et al.* Microwave Absorption and the Magnetic Hyperthermia Applications of $Li_{0.3} Zn_{0.3} Co_{0.1} Fe_{2.3} O_4$ Nanoparticles in Multiwalled Carbon Nanotube Matrix. *ACS Appl Mater Interfaces* **9**, 40831–40845 (2017).

111. Dalal, M., Das, A., Das, D., Ningthoujam, R. S. & Chakrabarti, P. K. Studies of magnetic, Mössbauer spectroscopy, microwave absorption and hyperthermia behavior of Ni-Zn-Co-ferrite nanoparticles encapsulated in multi-walled carbon nanotubes. *J Magn Magn Mater* **460**, 12–27 (2018).

112. Jiang, C. *et al.* Microwave absorption properties of gold nanoparticle doped polymers. *Solid State Electron* **57**, 19–22 (2011).

113. Ghahremani, F. H., Sazgarnia, A., Bahreyni-Toosi, M. H., Rajabi, O. & Aledavood, A. Efficacy of microwave hyperthermia and chemotherapy in the presence of gold nanoparticles: An in vitro study on osteosarcoma. *International Journal of Hyperthermia* **27**, 625–636 (2011).

114. Cifuentes-Rius, A. *et al.* Gold Nanocluster-Mediated Cellular Death under Electromagnetic Radiation. *ACS Appl Mater Interfaces* **9**, 41159–41167 (2017).

115. Dzimitrowicz, A. *et al.* Tuning Optical and Granulometric Properties of Gold Nanostructures Synthesized with the Aid of Different Types of Honeys for Microwave-Induced Hyperthermia. *Materials* **12**, 898 (2019).

116. Sun, M. *et al.* Enhanced Microwave Hyperthermia of Cancer Cells with Fullerene. *Mol Pharm* **13**, 2184–2192 (2016).

117. Kiourti, A., Sun, M., He, X. & Volakis, J. L. Microwave Cavity with Controllable Temperature for In Vitro Hyperthermia Investigations. *Journal of electromagnetic engineering and science* **14**, 267–272 (2014).

118. Li, W.-S. *et al.* Mild microwave activated, chemo-thermal combinational tumor therapy based on a targeted, thermal-sensitive and magnetic micelle. *Biomaterials* **131**, 36–46 (2017).

119. Shen, Q. *et al.* Sinomenine hydrochloride loaded thermosensitive liposomes combined with microwave hyperthermia for the treatment of rheumatoid arthritis. *Int J Pharm* **576**, 119001 (2020).

120. Castano, A. P., Mroz, P. & Hamblin, M. R. Photodynamic therapy and anti-tumour immunity. *Nat Rev Cancer* **6**, 535–545 (2006).

121. Wu, Q. *et al.* Dual-Functional Supernanoparticles with Microwave Dynamic Therapy and Microwave Thermal Therapy. *Nano Lett* **19**, 5277–5286 (2019).

122. Wu, Q. *et al.* Delivery of Arsenic Trioxide by Multifunction Nanoparticles To Improve the Treatment of Hepatocellular Carcinoma. *ACS Appl Mater Interfaces* **12**, 8016–8029 (2020).

123. Fu, C. *et al.* Microwave-Activated Mn-Doped Zirconium Metal–Organic Framework Nanocubes for Highly Effective Combination of Microwave Dynamic and Thermal Therapies Against Cancer. *ACS Nano* **12**, 2201–2210 (2018).

124. Zhou, H. *et al.* Mitochondria-targeted zirconium metal–organic frameworks for enhancing the efficacy of microwave thermal therapy against tumors. *Biomater Sci* **6**, 1535–1545 (2018).

125. Qi, J. *et al.* pH and Thermal Dual-Sensitive Nanoparticle-Mediated Synergistic Antitumor Effect of Immunotherapy and Microwave Thermotherapy. *Nano Lett* **19**, 4949–4959 (2019).

126. Crist, R. M. *et al.* Challenges in the development of nanoparticle-based imaging agents: Characterization and biology. *WIREs Nanomedicine and Nanobiotechnology* (2020) doi:10.1002/wnan.1665.

127. Bucci, O. M. *et al.* Assessing Detection Limits in Magnetic Nanoparticle Enhanced Microwave Imaging. *IEEE Access* **6**, 43192–43202 (2018).

128. Provenzano, R. *et al.* Ferumoxytol as an Intravenous Iron Replacement Therapy in Hemodialysis Patients. *Clinical Journal of the American Society of Nephrology* **4**, 386–393 (2009).

129. Toth, G. B. *et al.* Current and potential imaging applications of ferumoxytol for magnetic resonance imaging. *Kidney Int* **92**, 47–66 (2017).

130. Dong, J. & Ma, Q. Integration of inflammation, fibrosis, and cancer induced by carbon nanotubes. *Nanotoxicology* **13**, 1244–1274 (2019).

131. McWilliams, B. *et al.* Experimental Investigation of Magnetic Nanoparticle-Enhanced Microwave Hyperthermia. *J Funct Biomater* **8**, 21 (2017).

132. Singh, S. & Melnik, R. Thermal ablation of biological tissues in disease treatment: A review of computational models and future directions. *Electromagn Biol Med* **39**, 49–88 (2020).

133. Paudel, N. R., Shvydka, D. & Parsai, E. I. A novel property of gold nanoparticles: Free radical generation under microwave irradiation. *Med Phys* **43**, 1598–1602 (2016).

134. Halter, R. J. *et al.* The correlation of *in vivo* and *ex vivo* tissue dielectric properties to validate electromagnetic breast imaging: initial clinical experience. *Physiol Meas* **30**, S121–S136 (2009).

135. Meaney, P. M. *et al.* Clinical microwave breast imaging - 2D results and the evolution to 3D. in *2009 International Conference on Electromagnetics in Advanced Applications* 881–884 (IEEE, 2009). doi:10.1109/ICEAA.2009.5297356.

136. Meaney, P. M. *et al.* Initial Clinical Experience with Microwave Breast Imaging in Women with Normal Mammography. *Acad Radiol* **14**, 207–218 (2007).

137. Joines, W. T., Zhang, Y., Li, C. & Jirtle, R. L. The measured electrical properties of normal and malignant human tissues from 50 to 900 MHz. *Med Phys* **21**, 547–550 (1994).

138. Lazebnik, M. *et al.* A large-scale study of the ultrawideband microwave dielectric properties of normal breast tissue obtained from reduction surgeries. *Phys Med Biol* **52**, 2637—2656 (2007).

139. Lazebnik, M. *et al.* A large-scale study of the ultrawideband microwave dielectric properties of normal, benign and malignant breast tissues obtained from cancer surgeries. *Phys Med Biol* **52**, (2007).

140. Çeşmeli, S. & Biray Avci, C. Application of titanium dioxide (TiO_2) nanoparticles in cancer therapies. *J Drug Target* **27**, (2019).

141. Bellizzi, G., Bucci, O. M., Catapano, I., Crocco, L. & Scapaticci, R. Feasibility study of a novel microwave breast cancer imaging approach exploiting Magnetic Nanoparticle as contrast

agents. in *Proceedings of the 2012 IEEE International Symposium on Antennas and Propagation* 1–2 (IEEE, 2012). doi:10.1109/APS.2012.6348909.

142. Bucci, O. M. *et al.* Experimental feasibility assessment of MNP enhanced microwave diagnostics of breast cancer. in *2016 10th European Conference on Antennas and Propagation (EuCAP)* 1–4 (IEEE, 2016). doi:10.1109/EuCAP.2016.7481513.

143. Hervault, A. & Thanh, N. T. K. Magnetic nanoparticle-based therapeutic agents for thermo-chemotherapy treatment of cancer. *Nanoscale* **6**, 11553–11573 (2014).

144. Dadfar, S. M. *et al.* Iron oxide nanoparticles: Diagnostic, therapeutic and theranostic applications. *Adv Drug Deliv Rev* **138**, 302–325 (2019).

145. Sandiford, L. *et al.* Bisphosphonate-Anchored PEGylation and Radiolabeling of Superparamagnetic Iron Oxide: Long-Circulating Nanoparticles for in Vivo Multimodal (T1 MRI-SPECT) Imaging. *ACS Nano* **7**, 500–512 (2013).

146. Rani, R., Kumar, G., Batoo, K. M. & Singh, M. Electric and Dielectric Study of Zinc Substituted Cobalt Nanoferrites Prepared by Solution Combustion Method. *American Journal of Nanomaterials* **1**, 9–12 (2013).

147. Gupta, M. & Randhawa, B. S. Microstructural, magnetic and electric properties of mixed Cs–Zn ferrites prepared by solution combustion method. *Solid State Sci* **14**, 849–856 (2012).

148. Lees, E. E., Nguyen, T.-L., Clayton, A. H. A. & Mulvaney, P. The Preparation of Colloidally Stable, Water-Soluble, Biocompatible, Semiconductor Nanocrystals with a Small Hydrodynamic Diameter. *ACS Nano* **3**, 1121–1128 (2009).

149. Lazebnik, M., Converse, M. C., Booske, J. H. & Hagness, S. C. Ultrawideband temperature-dependent dielectric properties of animal liver tissue in the microwave frequency range. *Phys Med Biol* **51**, (2006).

150. Bharti, R., Gupta, J., Rajamani, P., Moulick, R. G. & Bhattacharya, J. Iron oxide nanoparticles/PEDOT: PSS nanocomposite-based modification of both glassy carbon electrode and flexible cotton fiber OECT for highly sensitive multi-analytes detection. *Appl Nanosci* **12**, 3823–3833 (2022).

151. Kumar, S. *et al.* Electrochemical paper based cancer biosensor using iron oxide nanoparticles decorated PEDOT:PSS. *Anal Chim Acta* **1056**, 135–145 (2019).

152. Zhang, M. *et al.* Highly Electrical Conductive PEDOT:PSS/SWCNT Flexible Thermoelectric Films Fabricated by a High-Velocity Non-solvent Turbulent Secondary Doping Approach. *ACS Appl Mater Interfaces* **15**, 10947–10957 (2023).

153. Shea, J. D., Kosmas, P., Van Veen, B. D. & Hagness, S. C. Contrast-enhanced microwave imaging of breast tumors: a computational study using 3D realistic numerical phantoms. *Inverse Probl* **26**, 074009 (2010).

154. Rahman, M., Lahri, R., Ahsan, S., Thanou, M. & Kosmas, P. Assessing Changes in Dielectric Properties Due to Nanomaterials Using a Two-Port Microwave System. *Sensors* **20**, 6228 (2020).

155. Wei, J. *et al.* Correlation between mammographic density and volumetric fibroglandular tissue estimated on breast MR images. *Med Phys* **31**, 933–942 (2004).

156. Surowiec, A., Stuchly, S. S. & Swarup, A. Radiofrequency dielectric properties of animal tissues as a function of time following death. *Phys Med Biol* **30**, 1131–1141 (1985).

157. Surowiec, A., Stuchly, S. S., Eidus, L. & Swarup, A. In vitro dielectric properties of human tissues at radiofrequencies. *Phys Med Biol* **32**, 615–621 (1987).

158. Kraszewski, A., Stuchly, M. A., Stuchly, S. S. & Smith, A. M. In vivo and in vitro dielectric properties of animal tissues at radio frequencies. *Bioelectromagnetics* **3**, (1982).

159. Gabriel, S., Lau, R. W. & Gabriel, C. The dielectric properties of biological tissues: II. Measurements in the frequency range 10 Hz to 20 GHz. *Phys Med Biol* **41**, (1996).

160. Foster, K. R. & Schwan, H. P. Dielectric properties of tissues and biological materials: a critical review. *Crit Rev Biomed Eng* **17**, (1989).

161. Asami, K. Characterization of biological cells by dielectric spectroscopy. *J Non Cryst Solids* **305**, 268–277 (2002).

162. Ištuk, N. *et al.* Dielectric Properties of Ovine Heart at Microwave Frequencies. *Diagnostics* **11**, (2021).

163. Peyman, A., Rezazadeh, A. A. & Gabriel, C. Changes in the dielectric properties of rat tissue as a function of age at microwave frequencies. *Phys Med Biol* **46**, (2001).

164. Schmid, G., Neubauer, G. & Mazal, P. R. Dielectric properties of human brain tissue measured less than 10 h postmortem at frequencies from 800 to 2450 MHz. *Bioelectromagnetics* **24**, (2003).

165. Farrugia, L., Wismayer, P. S., Mangion, L. Z. & Sammut, C. v. Accurate in vivo dielectric properties of liver from 500 MHz to 40 GHz and their correlation to *ex vivo* measurements. *Electromagn Biol Med* **35**, (2016).

166. Shahzad, A., Khan, S., Jones, M., Dwyer, R. M. & O'Halloran, M. Investigation of the effect of dehydration on tissue dielectric properties in *ex vivo* measurements. *Biomed Phys Eng Express* **3**, (2017).

167. Yilmaz, T. & Ates Alkan, F. In Vivo Dielectric Properties of Healthy and Benign Rat Mammary Tissues from 500 MHz to 18 GHz. *Sensors* **20**, 2214 (2020).

168. Rogers, J. A., Sheppard, R. J., Grant, E. H., Bleehen, N. M. & Honess, D. J. The dielectric properties of normal and tumour mouse tissue between 50 MHz and 10 GHz. *Br J Radiol* **56**, 335–338 (1983).

169. Hesabgar, S. M., Sadeghi-Naini, A., Czarnota, G. & Samani, A. Dielectric properties of the normal and malignant breast tissues in xenograft mice at low frequencies (100 Hz–1 MHz). *Measurement* **105**, 56–65 (2017).

170. Halter, R. J. *et al.* The correlation of *in vivo* and *ex vivo* tissue dielectric properties to validate electromagnetic breast imaging: initial clinical experience. *Physiol Meas* **30**, (2009).

171. Macit, Z., Aydinalp, C., Yilmaz, T., Sert, A. B. O. & Kok, F. N. Microwave Dielectric properties of Osteosarcoma Cell Line (SAOS-2) Suspensions. in *2019 23rd International Conference on Applied Electromagnetics and Communications (ICECOM)* 1–4 (IEEE, 2019). doi:10.1109/ICECOM48045.2019.9163627.

172. Nörtemann, K., Hilland, J. & Kaatze, U. Dielectric Properties of Aqueous NaCl Solutions at Microwave Frequencies. *J Phys Chem A* **101**, 6864–6869 (1997).

173. Cho, J. *et al.* In-vivo measurements of the dielectric properties of breast carcinoma xenografted on nude mice. *Int J Cancer* **119**, (2006).

174. Sun, J. *et al.* Treatment of malignant glioma using hyperthermia. *Neural Regen Res* **8**, 2775–82 (2013).

175. Zagar, T. M. *et al.* Hyperthermia for locally advanced breast cancer. *International Journal of Hyperthermia* **26**, 618–624 (2010).

176. Kok, H. P. *et al.* Heating technology for malignant tumors: a review. *Int J Hyperthermia* **37**, 711—741 (2020).

177. Bull, J. M. An update on the anticancer effects of a combination of chemotherapy and hyperthermia. *Cancer Res* **44**, 4853s–4856s (1984).

178. Datta, N. R. *et al.* Local hyperthermia combined with radiotherapy and-/or chemotherapy: Recent advances and promises for the future. *Cancer Treat Rev* **41**, 742–753 (2015).

179. Sawaji, Y., Sato, T., Takeuchi, A., Hirata, M. & Ito, A. Anti-angiogenic action of hyperthermia by suppressing gene expression and production of tumour-derived vascular endothelial growth factor in vivo and in vitro. *Br J Cancer* **86**, 1597–1603 (2002).

180. Repasky, E. A., Evans, S. S. & Dewhirst, M. W. Temperature Matters! And Why It Should Matter to Tumor Immunologists. *Cancer Immunol Res* **1**, 210–216 (2013).

181. Li, Z., Deng, J., Sun, J. & Ma, Y. Hyperthermia Targeting the Tumor Microenvironment Facilitates Immune Checkpoint Inhibitors. *Front Immunol* **11**, (2020).

182. Longo, T. A. *et al.* A systematic review of regional hyperthermia therapy in bladder cancer. *International Journal of Hyperthermia* **32**, 381–389 (2016).

183. Chen, X., Tan, L., Liu, T. & Meng, X. Micro-Nanomaterials for Tumor Microwave Hyperthermia: Design, Preparation, and Application. *Curr Drug Deliv* **14**, 307–322 (2017).

184. Gabriel, C. *Compilation of the Dielectric Properties of Body Tissues at RF and Microwave Frequencies.* (1996) doi:10.21236/ADA303903.

185. Luyen, H., Hagness, S. C. & Behdad, N. A Balun-Free Helical Antenna for Minimally Invasive Microwave Ablation. *IEEE Trans Antennas Propag* **63**, 959–965 (2015).

186. Hung Luyen, Fuqiang Gao, Hagness, S. C. & Behdad, N. Microwave Ablation at 10.0 GHz Achieves Comparable Ablation Zones to 1.9 GHz in Ex Vivo Bovine Liver. *IEEE Trans Biomed Eng* **61**, 1702–1710 (2014).

187. Fallahi, H. & Prakash, P. Antenna Designs for Microwave Tissue Ablation. *Crit Rev Biomed Eng* **46**, 495–521 (2018).

188. Sebek, J., Curto, S., Bortel, R. & Prakash, P. Analysis of minimally invasive directional antennas for microwave tissue ablation. *International Journal of Hyperthermia* **33**, 51–60 (2017).

189. Motamarry, A. *et al.* Extracorporeal Removal of Thermosensitive Liposomal Doxorubicin from Systemic Circulation after Tumor Delivery to Reduce Toxicities. *Cancers (Basel)* **14**, 1322 (2022).

190. Blanco-Andujar, C., Ortega, D., Southern, P., Pankhurst, Q. A. & Thanh, N. T. K. High performance multi-core iron oxide nanoparticles for magnetic hyperthermia: microwave synthesis, and the role of core-to-core interactions. *Nanoscale* **7**, 1768–1775 (2015).

191. García-Jimeno, S. *et al.* Improved Thermal Ablation Efficacy Using Magnetic Nanoparticles: A Study in Tumour Phantoms. *Progress In Electromagnetics Research* **128**, 229–248 (2012).

192. McWilliams, B. T., Schnell, E. E., Curto, S., Fahrbach, T. M. & Prakash, P. A Directional Interstitial Antenna for Microwave Tissue Ablation: Theoretical and Experimental Investigation. *IEEE Trans Biomed Eng* **62**, 2144–2150 (2015).

193. Motamarry, A. *et al.* Extracorporeal Removal of Thermosensitive Liposomal Doxorubicin from Systemic Circulation after Tumor Delivery to Reduce Toxicities. *Cancers (Basel)* **14**, 1322 (2022).

194. Chiang, J., Hynes, K. A., Bedoya, M. & Brace, C. L. A Dual-Slot Microwave Antenna for More Spherical Ablation Zones: Ex Vivo and in Vivo Validation. *Radiology* **268**, 382–389 (2013).

195. Yatvin, M. B., Weinstein, J. N., Dennis, W. H. & Blumenthal, R. Design of Liposomes for Enhanced Local Release of Drugs by Hyperthermia. *Science (1979)* **202**, 1290–1293 (1978).

196. Lyon, P. C. *et al.* Safety and feasibility of ultrasound-triggered targeted drug delivery of doxorubicin from thermosensitive liposomes in liver tumours (TARDOX): a single-centre, open-label, phase 1 trial. *Lancet Oncol* **19**, 1027–1039 (2018).

197. Zagar, T. M. *et al.* Two phase I dose-escalation/pharmacokinetics studies of low temperature liposomal doxorubicin (LTLD) and mild local hyperthermia in heavily pretreated patients with local regionally recurrent breast cancer. *International Journal of Hyperthermia* **30**, 285–294 (2014).

198. Celik, H. *et al.* Radiofrequency Ablation Duration per Tumor Volume May Correlate with Overall Survival in Solitary Hepatocellular Carcinoma Patients Treated with Radiofrequency Ablation Plus Lyso-Thermosensitive Liposomal Doxorubicin. *Journal of Vascular and Interventional Radiology* **30**, 1908–1914 (2019).

199. Gasselhuber, A. *et al.* Mathematical spatio-temporal model of drug delivery from low temperature sensitive liposomes during radiofrequency tumour ablation. *International Journal of Hyperthermia* **26**, 499–513 (2010).

200. Malinge, J. *et al.* Liposomes for PET and MR Imaging and for Dual Targeting (Magnetic Field/Glucose Moiety): Synthesis, Properties, and *in Vivo* Studies. *Mol Pharm* **14**, 406–414 (2017).

201. Cressey, P. *et al.* Image-guided thermosensitive liposomes for focused ultrasound enhanced co-delivery of carboplatin and SN-38 against triple negative breast cancer in mice. *Biomaterials* **271**, 120758 (2021).

202. Robison, L. L. & Hudson, M. M. Survivors of childhood and adolescent cancer: life-long risks and responsibilities. *Nat Rev Cancer* **14**, 61–70 (2014).

203. Yarmolenko, P. S. *et al.* Comparative effects of thermosensitive doxorubicin-containing liposomes and hyperthermia in human and murine tumours. *International Journal of Hyperthermia* **26**, 485–498 (2010).